elektronisches dokument
ULB Sachsen-Anhalt

Spin-polarized scanning tunneling microscopy

Dissertation

zur Erlangung des akademischen Grades

Doctor rerum naturalium (Dr. rer. nat.)

vorgelegt der

Mathematisch-Naturwissenschaftlich-Technischen Fakultät
(mathematisch-naturwissenschaftlicher Bereich)
der Martin-Luther-Universität Halle-Wittenberg

von Herrn **Haifeng Ding**

geb. am: 05. Juli 1973 in Fujian, V. R. China

Gutachterin/Gutachter:

1. Prof. Dr. J. Kirschner
2. Prof. Dr. H. Neddermeyer
3. Prof. Dr. K. Baberschke

Halle/Saale, October 17 (2001).

urn:nbn:de:gbv:3-000002596
[http://nbn-resolving.de/urn/resolver.pl?urn=nbn%3Ade%3Agbv%3A3-000002596]

Abstract

A new magnetic imaging technique, i.e., spin-polarized scanning tunneling microscopy, is presented. The technique is based on the tunneling magneto resistance (TMR) effect between a ferromagnetic tip and a ferromagnetic sample. By periodically changing the magnetization of a magnetically soft tip in combination with lock-in technique, topographic and spin-dependent parts of the tunneling current are separated and the topography and the magnetic structure of the sample can be recorded simultaneously with high resolution. Besides magnetic imaging, dynamic effects like domain wall mobility or the magnetic susceptibility can be studied locally with the double frequency response in the limit of soft magnetic materials or strong stray fields of the tip. We studied the closure domain structure of Co(0001) with high resolution and found surprisingly narrow sections of the wall of 1.1 nm width, over an order of magnitude less than previously observed in bulk Co. The ultra narrow domain walls are explained on the basis of a simple micromagnetic model which predicts a wall width of 1.5 nm. Further, measurements of the TMR versus the tunneling voltage and the tip-to-sample distance as well as the study of the influence of a nonmagnetic Au layer on the TMR effect give deeper insight into the mechanisms of spin-polarized tunneling.

Zusammenfassung

Eine neue magnetische Abbildungstechnik, die spin-polarisierte Rastertunnelmikroskopie wird vorgestellt. Die Technik basiert auf dem Tunnelmagnetowiderstandseffekt (TMR-Effekt) zwischen einer ferromagnetischen Spitze und der ferromagnetischen Probe. Indem die Magnetisierung der weichmagnetischen Spitze periodisch umgeschaltet wird und die dabei durch den TMR-Effekt verursachten Schwankungen des Tunnelstroms mittels eines phasensensitiven Verstärkers gemessen werden, können Spin abhängige und Topographie abhängige Anteile des Tunnelstroms getrennt werden und Topographie und magnetische Struktur der Probe gleichzeitig mit hoher lateraler Auflösung abgebildet werden. Über die magnetische Abbildung hinaus kann die Mobilität von Domänenwänden und die magnetische Suszeptibilität der Probe lokal über den frequenzverdoppelten Anteil im Tunnelstrom studiert werden. Wir haben die Struktur der Abschlußdomänen von Co(0001) mit hoher Auflösung abgebildet und haben überraschend scharfe Domänenwände von einer Breite von nur 1.1 nm gefunden. Dieses ist eine Größenordnung schärfer als die bekannten Domänenwände im Inneren eines Co Kristalls. Die scharfen Domänenwände werden mittels eines einfachen, mikromagnetischen Modells erklärt, welches eine Wandbreite von 1.5 nm erwarten läßt. Drüber hinaus wurde der TMR-Effekt als Funktion der Tunnelspannung und des Spitzen-Proben-Abstands gemessen und der Einfluß einer unmagnetischen Au Deckschicht auf den TMR Effekt untersucht. Die Messungen erlauben einen tieferen Einblick in die Mechanismen des spin-polarisierten Tunnelns.

Contents

1 Introduction **1**

2 Theoretical background **5**
2.1 Jullière's model - a phenomenological explanation 6
2.1.1 Bandstructure difference between ferromagnetic and nonmagnetic material 6
2.1.2 Spin conservation in tunneling - an assumption 7
2.1.3 Formalism of tunneling magneto resistance effect 7
2.2 Slonczewski's model - a quantitative calculation 9
2.3 Bandstructure effects 12

3 Experimental setup **15**
3.1 UHV-chamber and surface analysis techniques 15
3.2 Sp-STM setup 16
3.2.1 STM 16
3.2.2 Sp-STM basic setup 17
3.3 The magnetic tip 20
3.3.1 Tip material 20
3.3.2 Etching of tips 20
3.3.3 The stray field of the tip 22
3.4 In-situ sample and tip preparation 26

4 Results and discussion **29**
4.1 Magnetic imaging 29
4.1.1 Influence of the external field 29
4.1.2 Comparison with standard magnetic imaging techniques 31
4.1.3 Estimation of resolution 36
4.1.4 Summary 38
4.2 Ultra narrow surface domain walls of Co(0001) 39
4.2.1 Surface closure domain of Co(0001) 39

4.2.2 Experiments 39
4.2.3 Surface closure domain model 43
4.2.4 Summary 52
4.3 Local magnetic susceptibility 53
4.4 Tip-to-sample distance dependence of the TMR through a vacuum barrier 56
4.5 Bias voltage dependence of the TMR through a vacuum barrier 63
4.5.1 Brief summary of the TMR across an insulator barrier 63
4.5.2 Voltage dependence of the TMR across a vacuum barrier 66
4.6 Spin-polarized tunneling through a nonmagnetic spacer 74

5 Main conclusions and summary **83**

A Component resolved Kerr effect **i**

B Curriculum vitae **xvii**

C Publication lists **xix**

D Erklärung **xxi**

E Acknowledgements **xxiii**

Chapter 1

Introduction

The concept of domains defines regions in which all the elements of a region share a common specific property. A magnetic domain is a region in which the magnetic moments of all atoms point into the same direction. Magnetic domains are the basic elements of the magnetic microstructure of a magnet and link the basic physical properties of the magnet with its macroscopic properties and applications [1]. In the early theories there was no clear concept of magnetic domains. They were only considered as magnetic impurities in which the magnetization direction deviates from the main orientation. Magnetic domains, however, were very quickly proven to be one of the key issues in magnetism. They are not only crucial for the analysis of magnetization curves but also in the development of new magnetic materials and the design of new magnetic devices. Thus, an understanding of the domain configuration is highly required.

Magnetic imaging is of course fundamental for micromagnetism, even though the existence of magnetic domains was initially not concluded from magnetic images but from the famous observations of Barkhausen [2], that magnetic hysteresis loops show discontinuous jumps attributed to the switching of individual domains. Magnetic imaging has been one of the most important driving forces for micromagnetism and has lead to valuable input for many theoretical micromagnetic studies. Different magnetic imaging techniques, i.e., methods to map in real space one or several components of the magnetization vector or a related quantity, have been developed for different specific problems. Beginning with the Bitter technique [3], where small ferromagnetic particles are used to decorate the local stray fields exiting a sample surface, the field of magnetic imaging has evolved quickly. Shortly after the utilization of magneto-optical effects to map a component of the magnetization [4], high resolution transmission electron microscopy was used to image domains in thin films [5]. Later, Koike and Hayakawa [6] established scanning electron microscopy with polarization analysis of the secondary electrons (SEMPA), which allows to map all three components of the magnetization of a surface. With surface sensitive techniques like SEMPA, spin-polarized low energy electron microscopy (SPLEEM) or photoemission electron microscopy (PEEM) magnetic resolutions of 10-30 nm have been achieved [7–9]. Several tech-

niques, e.g., PEEM and x-ray microscopy [10], even offer element specific information on the magnetization. Besides these techniques, magnetic force microscopy (MFM) has evolved to a standard magnetic imaging technique, due to its fair resolution around several 10 nm [11] in combination with its low costs and the small experimental efforts to carry out imaging.

Those magnetic imaging techniques mentioned above have already led to deep insights in magnetism and yield important applications. Due to the resolution limit of those techniques, however, not many experimental facts are known about the detailed structures of domains and domain walls in magnetic materials on the length scales set by the magnetic exchange length, i.e., below 10 nm. The knowledge about the magnetic structure on these small scales, however, is believed to be crucial for the fundamental understanding of micromagnetism and the controlling of magnetic media and devices in the near future. Especially, magnetism on the sub-micrometer scale has attained increasing attention recently. Not only that in commercially available data storage devices, the recording density has increased immensely so that bit lengths below 50 nm have been demonstrated, but also in the field of patterned media [12–16] and magnetic non-volatile memory cells, magnetic structures on the nanometer scale are aimed. Hence, a new magnetic imaging technique with nanometer or even atomic resolution is highly required.

Since its invention in 1981 [17], scanning tunneling microscopy (STM) has developed into a powerful surface analysis technique because it allows to investigate the surface structure in real space with atomic resolution [18]. Working in the field of magnetic imaging, one may ask the simple question: *"Is it possible to develop a similar technique like STM to image magnetic domains with high resolution?"*.

The invention of spin-polarized scanning tunneling microscopy (Sp-STM) is the direct answer to this question. During the last 10 years, many attempts have been made in this field [19–29]. Two different approaches have been of major importance to obtain sensitivity to the electron spin. First, the use of ferromagnetic tips that lead to a spin-polarized tunneling current, and second, the use of GaAs tips with spin-polarized carriers that are created by optical pumping with circularly polarized light. Early attempts in the beginning of the nineties to use ferromagnetic tips and utilize the tunneling magneto resistance effect [30] were only of limited success. The experiments by Johnson and Clarke [19], who used bulk Ni tips to image the magnetic structure of surfaces in air, were dominated by spurious effects like the tip magnetostriction and mechanical vibrations of the tip due to magnetic dipolar forces between tip and sample. Almost at the same time, Wiesendanger et al. [20] claimed to observe spin-polarized vacuum tunneling at room temperature between a ferromagnetic CrO_2 tip and the topological antiferromagnetic Cr(001) surface. The separation of topography and magnetic structure, however, was not achievable within this technique. In the mid nineties, a more promising approach to magnetic imaging [23–26] using optically pumped GaAs tips and a lock-in technique to separate topographic and magnetic information was established. However, it suffers from low contrast and an unintended additional optical contrast of limited lateral resolution [26]. Up to now, no experiments have been

published that prove the magnetic origin of the observed domains. Moreover, non-magnetic films are reported to show a similar signal to the domains in magnetic films [31] raising the question of the reliability of this method. Recently, the first approach to use ferromagnetic tips was revived by different groups [28, 29]. Bode et al. used tungsten tips coated with a thin ferromagnetic film to tunnel into the exchange-split surface state of Gd(0001) [28], Fe(001) [32] and recently of Cr(001) [33]. A magnetic contrast could be separated from the topography by local tunneling spectroscopy allowing magnetic imaging. This method, however, is limited to materials with well defined exchange split states and requires a rather flat surface.

In this work, a new technique to image magnetic domains by locally measuring the tunneling magneto resistance between a magnetic tip and the surface of a specimen is presented. By applying an alternating current of frequency f through a small coil wound around the magnetic tips, the longitudinal magnetization of the tip is switched periodically. (The whole volume of the tip is ferromagnetic such that the field of the coil at the backside of the tip switches the end of the tip between the two well known energetically favored states of opposite magnetization.) The frequency $f = 40 - 80$ kHz was chosen far away from any mechanical resonances of the STM and well above the cut-off frequency of the feed-back loop. In this way the variations of the tunneling probability due to the TMR effect result in variations of the tunneling current while a constant tip-to-sample distance is kept. The variations on the top of the average tunneling current set by the feed-back loop were detected with a phase sensitive lock-in amplifier. The average tunneling current is used as the feed-back to image the topography as a normal STM measurement. By this, the spin-dependent information and the topographic information are separated [29]. The technique offers a high magnetic contrast, fast data acquisition times in the range of ms/pixel. The lateral resolution of the technique is demonstrated to be well below 1 nm. Besides, in the presence of a short pulse of the external magnetic field, the local wall mobility can be studied dynamically.

As the TMR effect is proportional to the scalar product of the magnetization of the tip and the sample surface [34], the technique is sensitive to the magnetization component of the sample parallel to the tip magnetization. In the present case, where needle like magnetic tips are used, it is sensitive to the magnetization component perpendicular to the sample surface.

Due to the close proximity of the tunneling tip to the sample, the magnetic dipole interaction between these two ferromagnets cannot be neglected in all cases. For sharp tips and magnetic hard samples, no significant modifications of the domain structure by the tip is present. In the limit of soft magnetic material or strong stray fields of the tip, the sample magnetization can oscillate with the same frequency of the modulation frequency due to the influence of the stray field of the tip. This behavior is related to the local magnetic susceptibility. As the changes of both the tip and the sample magnetization are of the same frequency, the local susceptibility can be obtained as the double frequency response of the tunneling current. This can be used for dynamic studies like measurements of the wall mobility.

In addition to magnetic imaging and local magnetic susceptibility, the technique also allows to study the tunneling magneto resistance in a clean system. In comparison with planar tunneling junctions with insulator barriers, that are commonly studied presently, Sp-STM has well defined electrodes and an impurity free vacuum barrier. This offers the possibility to learn more about the fundamental physics of spin-polarized tunneling.

In the next chapter a short outline of the theoretical background of the tunneling magneto resistance effect will be given. Chapter 3 describes the experimental setup. The main results and discussions of this thesis will be presented in chapter 4. And finally a brief summary and conclusion will be given in Chapter 5.

Chapter 2

Theoretical background

Spin-polarized tunneling can be traced back to the early 1970s. The experiments of Tedrow and Meservey in 1971 [35], which addressed the magnetic field dependence of tunneling spectra between a superconducting Al film and the ferromagnetic metal Ni, gave the first evidence of spin conservation in electron tunneling. Under the influence of a strong magnetic field, the quasiparticle density of states of the superconducting Al film is split into spin-up and spin-down components [36] and the magnetization of the Ni film is fully aligned. The observed asymmetry of the tunneling conductance between states of different spin orientation of the Al film and the states of the ferromagnetic Ni film reflects the spin polarization of the Ni film.

In the sprit of Tedrow and Meservey's experiments, Jullière discovered that the tunneling between two ferromagnetic films is spin sensitive as well [30]. In his experiments, two magnetic films, Fe and Co, are isolated by a thin Ge film to form a tunneling junction. The two magnetic films are chosen to have the same easy axis of magnetization, but different coercive fields. These properties permit to align their magnetization parallel (when the applied magnetic field is higher than both coercive fields) or antiparallel (when the magnetization of the soft layer is switched and the external field is between the two coercive fields). Therefore, the difference between the tunneling conductance of the parallel and antiparallel configuration (tunneling magneto resistance) can be detected by tuning the magnitude of the external field. With this smart design, Jullière was able to obtain a tunneling magneto resistance of up to 14% at low temperatures (4.2 K). In his paper, he also proposed a very simple model to explain the tunneling magneto resistance effect by assuming spin conservation in tunneling.

2.1 Jullière's model - a phenomenological explanation

Although the model given by Jullière is so simple that it even could not predict the correct sign of the spin polarization of some materials,[1] it indeed gives a clear physical picture of the magneto-tunneling phenomena. To understand it, we need to look at the differences in the bandstructure between a nonmagnetic material and a ferromagnetic material as only the tunneling between two ferromagnetic electrodes shows the tunneling magneto resistance effect.

2.1.1 Bandstructure difference between ferromagnetic and nonmagnetic material

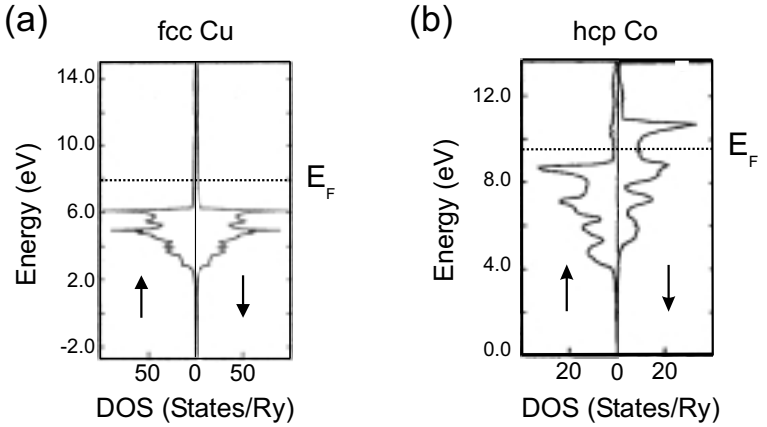

Figure 2.1: Comparison between the density of states (DOS) of a nonmagnetic material (Cu) and a ferromagnetic material (Co). For fcc Cu, the DOS for spin-up and spin-down electrons are identical (a). For hcp Co, the DOS for spin-up and spin-down electrons are different (b). The figures are taken from ref. [39].

Experimentally, we know that the electron has a spin of 1/2 and hence can be described by the expectation value of S_z, which can point in two directions, either the spin-up or the spin-down direction [38]. In a nonmagnetic material, for instance Cu, Au etc., the distributions of spin-up and spin-down electrons are identical. Due to the exchange interaction in a ferromagnetic material like Fe, Co, Ni etc., the potential of the electrons with spin orientation parallel to the molecular field is lower than that of the electrons with spin antiparallel to the molecular field. This causes an exchange splitting of the electron states in energy and, as a consequence, the distributions of spin-up and spin-down electrons are different. In the density of states shown in Fig. 2.1 we can clearly see the asymmetry in the bandstructure of a ferromagnetic material in

[1] At that time, the spin polarization was defined as the asymmetry of the density of states at the Fermi level. Later, the spin polarization was redefined by Mazin [37] according to the different measuring methods. Then the conflict disappeared.

contrast to a nonmagnetic material. In Fig. 2.1a, the density of states of a typical nonmagnetic material, fcc Cu, is symmetric for spin-up and spin-down electrons. The density of states of a typical ferromagnetic material, hcp Co in Fig. 2.1b, however, shows a clear asymmetry for spin-up and spin-down electrons. The asymmetry of the distribution causes a difference in the tunneling probability for spin-up and spin-down electrons as the tunneling probability is strongly related to the DOS.

2.1.2 Spin conservation in tunneling - an assumption

As the tunneling barriers used for magneto-tunneling junctions usually are nonmagnetic metal oxides like Al_2O_3 or MgO in which the spin orbit coupling is small or vanishing, spin-flip tunneling which is mainly induced by spin orbit coupling, magnetic impurity scattering and magnon excitation, can be considered as only a minor effect, especially in the approximation of small bias voltages. Therefore, it is generally believed that the spin is conserved in the tunneling process, i.e., the electrons keep their spin orientations during tunneling. The spin orientation of spin-up electrons still points upward while the spin orientation of the spin-down electrons still points downward after tunneling.

2.1.3 Formalism of tunneling magneto resistance effect

In a magneto-tunneling junction, two ferromagnetic materials with spin polarizations P_1 and P_2 are separated by a tunneling barrier. At a small bias, most of the electrons are tunneling near the Fermi level. The spin polarization P_i is defined as the asymmetry of the spin-up and spin-down electrons at the Fermi energy, i.e., $(N_\uparrow - N_\downarrow)/(N_\uparrow + N_\downarrow)$ with $N_\uparrow$ and $N_\downarrow$ the number of spin-up and spin-down electrons, respectively. When the magnetization of these two ferromagnetic materials is parallel, then their spin axes, which are defined as parallel to the magnetization directions, are also parallel. As mentioned above, the electrons keep their spin direction during the tunneling process. Hence, the spin-up and spin-down electrons of magnetic material 1 tunnel into the spin-up and spin-down empty states of magnetic material 2, respectively. Assuming the tunneling probability is proportional to the product of the density of states of each electrode [35], the tunneling conductance G_P at a small bias is proportional to:

$$N_\uparrow(1)N_\uparrow(2) + N_\downarrow(1)N_\downarrow(2) \tag{2.1}$$

In the case of antiparallel configuration, the spin-up electrons of magnetic material 1 tunnel into the spin-down empty states instead of the spin-up empty states of magnetic material 2. The spin-down electrons of magnetic material 1 tunnel into the spin-up empty states of magnetic material 2. This, at the first sight, might be a little bit confusing but due to the antiparallel configuration, the roles of minority and majority electrons are swapped in one of the electrodes. The spins of the tunneling electrons are still conserved as their respective spin axes are opposite in these two

magnetic materials. Therefore, the tunneling conductance for antiparallel configuration G_{AP} at a small bias is approximatively proportional to:

$$N_{\uparrow}(1)N_{\downarrow}(2) + N_{\downarrow}(1)N_{\uparrow}(2) \tag{2.2}$$

The TMR effect, which is defined as the change of conductance ΔG between the parallel and antiparallel configuration divided by the conductance in the parallel configuration G_P, can be written as:

$$\frac{\triangle G}{G_P} = \frac{2P_1P_2}{1 + P_1P_2} \tag{2.3}$$

From this formula, it can be seen that the tunneling magneto resistance effect vanishes if either P_1 or P_2 is zero, for instance, if one of the magnetic electrode is replaced by a nonmagnetic material. Hence, only in the case that both electrodes are spin-polarized the tunneling magneto resistance effect remains.

So far, we discussed the tunneling conductance for the parallel and antiparallel configuration. In the following, we will consider the tunneling conductance in another possible configuration, that is when the magnetization directions of both layers are perpendicular to each other. For simplicity, we assume that the first magnetic layer has different distribution for spin-up and spin-down electrons and the second magnetic layer has different distribution for spin-left and spin-right electrons, respectively. When the spin-up electrons of the first magnetic layer tunnel into the second magnetic layer, they do not know wether they are spin-left or spin-right electrons. Neither spin-left nor spin-right are eigenvalues for the wave function of the spin in the first electrode, but they are linear combination of those according to their projection which is $\frac{1}{\sqrt{2}}$. Therefore, the spin-up electrons simply have the same probability to enter either spin-left or spin-right states. As mentioned above, the conductance at small bias is proportional to the product of the density of states at the Fermi level of the two layers. For the spin-up electrons, it can be written as:

$$\frac{1}{2}N_{\uparrow}(1)N_{\leftarrow}(2) + \frac{1}{2}N_{\uparrow}(1)N_{\rightarrow}(2) \tag{2.4}$$

Similarly, the tunneling conductance for the spin-down electrons to cross this junction can be written as:

$$\frac{1}{2}N_{\downarrow}(1)N_{\leftarrow}(2) + \frac{1}{2}N_{\downarrow}(1)N_{\rightarrow}(2) \tag{2.5}$$

The total conductance of the tunneling junction is the sum of both. One can figure out that it is exactly the average value of the tunneling conductance for the parallel and antiparallel configuration. The same conductance is found when the magnetization of one electrode is reversed and hence the TMR is zero.

As the magnetization is a vector, it can be split up into several components. When the magnetization of both magnetic layers points into arbitrary directions, the magnetization of the second

layer can be considered to have two components, i.e., the component parallel/perpendicular to the magnetization orientation of the first layer, respectively. As discussed above, the magnetization component of the second layer which is perpendicular to the magnetization of the first layer has no contribution to the magneto-tunneling current. Only the magnetization component which is parallel to the magnetization orientation of the first layer has the contribution to the TMR effect. This contribution is proportional to the scalar product of the two layer magnetization. Hence, the tunneling magneto resistance effect is proportional to $\cos\theta$ with θ the angle between the magnetization of the two layers. This angular dependence of the TMR effect has been confirmed experimentally by Miyazaki and Tezuka [40] in 1995.

2.2 Slonczewski's model - a quantitative calculation

Following Stearns' theory [41], Slonczewski gave a quantitative model [34] to calculate the spin-polarized tunneling within the free electron approximation for arbitrary magnetization alignment of two magnetic layers isolated by a thin tunneling barrier.

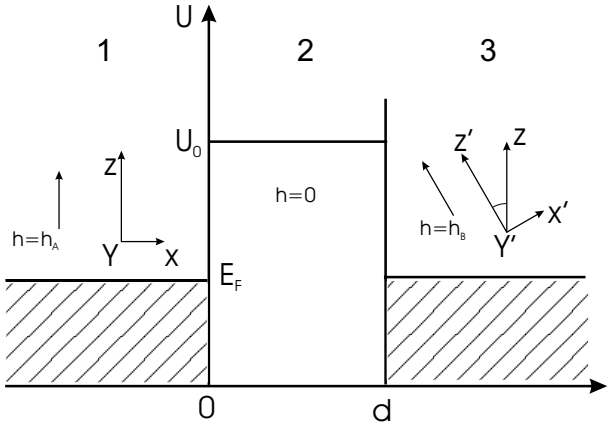

Figure 2.2: Schematic potential distribution for two metallic ferromagnets separated by an insulating barrier. The molecular fields $h_A(t)$ and $h_B(t)$ within the magnets form an angle of θ. They are parallel to the static axes z and z' at $t = 0$, respectively. The figure is taken from Ref. [34].

As shown in Fig. 2.2, Slonczewski considered two magnetic layers (layer 1 and 3) with the potential energy $U = 0$ and molecular fields $h = h_A$ and h_B, respectively, isolated by a nonmagnetic rectangular barrier (layer 2). This barrier has a potential energy $U = U_0$ and vanishing molecular field $h = 0$. For simplicity, he assumed the external voltage between the electrodes $V = 0$ and $|h_A| = |h_B| = h_0$. However, the direction of h_A and h_B, as well as the corresponding spin quantization axes z and z', differ by an angle of θ (see Fig. 2.2). Note that

only the mutual relationship between the coordinate systems x, y, z and x',y',z' matters. Their orientation with respect to the plane of the junction does not matter.

As the transverse momentum (the momentum parallel to the interface) $k_{\|}$ is conserved during the tunneling process, only the longitudinal part of the momentum is considered. In a free-electron approximation of the spin-polarized conduction electrons inside each ferromagnet, the longitudinal part of the effective one-electron Hamiltonian can be written as:

$$H_\xi = -\frac{1}{2}(\frac{d}{d\xi})^2 + U(\xi) - h(\xi)\cdot\sigma \tag{2.6}$$

Here the unit system incorporates the unit of electron mass and the unit of Planck constant. The term $-h(\xi)\cdot\sigma$ is the internal exchange energy with $-h(\xi)$ the molecular field and $\sigma = 2s$ (s is the eigen function of spin, $\pm\frac{1}{2}$) the conventional Pauli spin operator. We can write the Schrödinger equation Eq. 2.6 and obtain the electron energy for each layer. Inside the ferromagnets (layer 1 and 3), the one electron energy is:

$$E_\xi = \frac{1}{2}k_\sigma^2 - \sigma h_0, \quad \sigma = \pm 1 \; or \uparrow,\downarrow \tag{2.7}$$

where k_σ are the electron momenta for spin-up and spin-down electrons, respectively. Inside the barrier (layer 2), the energy is

$$E_\xi = \frac{1}{2}\kappa^2 + U_0, \quad \sigma = \uparrow,\downarrow \tag{2.8}$$

where $i\kappa$ is the imaginary momentum inside the barrier.

Consider a spin-up incident plane wave having unit incident flux in region 1 (ferromagnetic 1, $\xi < 0$ in Fig. 2.2). Taking into account all the boundary conditions, the eigenfunctions of H_ξ (eigenvalue E_ξ) in the three regions can be written as
In region 1 ($\xi < 0$):

$$\psi_{\uparrow 1} = k_\uparrow^{-1/2}e^{ik_\uparrow\xi} + R_\uparrow e^{-ik_\uparrow\xi}, \quad \psi_{\downarrow 1} = R_\downarrow e^{-ik_\downarrow\xi}, \tag{2.9}$$

In region 2 ($0 \le \xi \le d$):

$$\psi_{\sigma 2} = A_\sigma e^{-\kappa\xi} + B_\sigma e^{\kappa\xi}, \quad \sigma = \uparrow,\downarrow, \tag{2.10}$$

In region 3 ($\xi > d$):

$$\psi_{\sigma 3} = C_\sigma e^{ik_\sigma(\xi-d)}, \quad \sigma = \uparrow,\downarrow, \tag{2.11}$$

In the above equations, the eight unknowns R_σ, A_σ, B_σ, C_σ ($\sigma = \uparrow,\downarrow$) can be obtained by matching ψ_σ and $d\psi_\sigma/d\xi$ at the interfaces $\xi = 0$ and $\xi = d$. The change in the quantization axis at $\xi = d$ requires the spin or transformation

$$\begin{pmatrix} \psi_{\uparrow 2} \\ \psi_{\downarrow 2} \end{pmatrix} = \begin{pmatrix} \cos(\theta/2) & \sin(\theta/2) \\ -\sin(\theta/2) & \cos(\theta/2) \end{pmatrix} \begin{pmatrix} \psi_{\uparrow 3} \\ \psi_{\downarrow 3} \end{pmatrix} \tag{2.12}$$

and similarly for the derivatives.

With the obtained parameters, the conventional particle transmission coefficient can be calculated as

$$T = Im \sum_{\sigma} \psi_{\sigma}^{*} \frac{d\psi_{\sigma}}{d\xi} \tag{2.13}$$

Considering only zero temperature and in the limit of a small barrier factor, a narrow distribution of electrons near the normal incidence with E_ξ close to E_F carry most of the current. Therefore $\kappa(E_\xi)$ and $k_\sigma(E_\xi)$ can be replaced with $\kappa(E_F)$ and $k_\sigma(E_F)$, respectively, in calculating the conductance G due to tunneling. By summing the charge transmission over E_ξ and $k_{||}$ for occupied states in the usual manner [42], one finds the conventional expression for the tunneling conductance.

$$G = (e^2/8\pi^2\hbar)(\kappa T/d) \tag{2.14}$$

For simplicity, only the tunneling magneto resistance effect between two identical magnetic layers f across the barrier b is considered for the moment. According to the above calculation of the transmissivity, the tunneling conductance can be written as,

$$G = G^0_{fbf}(1 + P_{fb}P_{fb}cos\theta) \tag{2.15}$$

with the effective spin polarization of the ferromagnetic-barrier couple

$$P_{fb} = \frac{(k_\uparrow - k_\downarrow)}{(k_\uparrow + k_\downarrow)} \frac{(\kappa^2 - k_\uparrow k_\downarrow)}{(\kappa^2 + k_\uparrow k_\downarrow)} \tag{2.16}$$

and the mean conductance

$$G^0_{fbf} = \frac{\kappa}{\hbar d}[\frac{e\kappa(\kappa^2 + k_\uparrow k_\downarrow)(k_\uparrow + k_\downarrow)}{\pi(\kappa^2 + k_\uparrow^2)(\kappa^2 + k_\downarrow^2)}]^2 e^{-2\kappa d} \tag{2.17}$$

Assuming $k_\uparrow = k_\downarrow$ (nonmagnetic electrode), the formula also gives the tunneling conductance between two nonmagnetic electrodes.

In a more general treatment of this problem, the ferromagnetic electrodes f and f' can have different compositions. Thus, the quantities $k_\uparrow$ and $k_\downarrow$ are assumed to be different for the two electrodes. One finds easily,

$$G = G^0_{fbf'}(1 + P_{fb}P_{f'b}cos\theta) \tag{2.18}$$

where P_{fb} ($P_{f'b}$) is given with $k_\uparrow$, $k_\downarrow$ replaced by $k_{\uparrow f}$, $k_{\downarrow f}$ ($k_{\uparrow f'}$, $k_{\downarrow f'}$), respectively.

Slonzweski's model gives a clear dependence of the tunneling conductance of the junction with the relative projection of the magnetizations of two magnetic layers. This is in agreement with Jullière's model mentioned above. In comparison with Jullière's model, Slonzweski pointed out the importance of the barrier for the tunneling magneto resistance effect. The tunneling magneto resistance effect not only depends on the spin polarization of the magnetic electrodes, but also correlates with the barrier properties.

2.3 Bandstructure effects

Jullière's model gave a qualitively explaination why the tunneling conductance between two magnetic layers isolated by a thin isolating layer depends on the relative alignment of the magnetization. Slonzewski explained the effect in a more quantitative model which also includes the effect of the tunneling barrier. In a real junction, however, different states have different effective masses and velocities, and therefore the complete bandstructure of materials, both of the magnetic and the insulating layers have to be considered. Also, the interfaces between ferromagnet and insulator barrier need to be included. Recently, theoretical works have obtained further understanding for the TMR effect along this direction [43–45].

Many experiments [28, 46–48] have shown a strong relation between the TMR effect with the bandstructure. The TMR observed in most of the experiments is positive (the tunneling conductance for parallel configuration is higher than that for antiparallel configuration). Recently, also a negative TMR has been found in some experiments [46–48]. De Teresa et al. [47, 48] used $La_{0.7}Sr_{0.3}MnO_3$ as an electrode to tunnel through $SrTiO_3$ barrier into a Co film. It was observed that the TMR of the junction changed its sign when the bias voltage crossed 0.8 V. The result can be explained in the following way: as the barrier used in this junction, $SiTiO_3$ has a predominant d-d bonding between fcc Co and Ti or Si at the interface, d-electrons are dominant in tunneling. When the bias voltage changes, the tunneling reflects the bandstructure of the fcc Co d-band, which changes its polarity when the bias voltage crosses 0.8 V. Meanwhile, $La_{0.7}Sr_{0.3}MnO_3$ is half metallic ferromagnetic oxide. The sign of the polarization of half metallic ferromagnetic oxides usually does not change with the bias voltage. As the polarity of the TMR depends on the product of the two electrodes' polarization (see Jullière's model, Eq. 2.3) it also changes sign when the bias voltage crosses 0.8 V. Almost at the same time, Sharma et al. [46] used two different oxide layers to form an asymmetric tunneling barrier. The tunneling junction, $Ni_{80}Fe_{20}/Ta_2O_5/Al_2O_3/Ni_{80}Fe_{20}$ which has two different metal-insulator interfaces, (one $Ni_{80}Fe_{20}/Ta_2O_5$ and the other $Al_2O_3/Ni_{80}Fe_{20}$), also leads to a negative TMR effect for certain bias voltages. The effect was explained by very different band structures of Ta_2O_5 and Al_2O_3 and consequently different bounding characteristics. The relative contribution from s-electrons and from d-electrons to the tunneling current could be markedly different at the two interfaces even though the electrode materials are the same. Similar to fcc Co, which was calculated by Tsymbal et al. with first principle theory [49], the spin polarization of s-electrons in $Ni_{80}Fe_{20}$ could be opposite in sign compared to the spin polarization of the d-electrons. The character of the tunneling electrons is different for different interfaces, thus leading to spin polarizations of opposite signs and to a negative TMR at certain bias voltages. Inspired by the prediction of oscillations of the TMR in FM-NM-I-NM-FM[2] systems as a function of NM layer thickness [50, 51], Moodera [52] et al. measured the dependence of the TMR of $Co/Au/Al_2O_3/Ni_{80}Fe_{20}$ junction

[2]FM: ferromagnetic layer, NM: nonmagnetic layer, I: insulating layer

on the Au layer thickness. They found oscillations with the Au layer thickness which originate from quantum well states (QWS) in the Au layer. The experiments of Bode et al. [28], where a thin magnetic film coated tip is used to tunnel into the exchange split surface states, revealed the role of spin-polarized surface states.

Experimentally, high values of TMR can be achieved with good reproducibility even at room temperature. This leads to some important applications, like magnetic random access memory (MRAM), magnetic reading heads and picotesla field sensors. Many theoretical efforts have contributed to the understanding of the effect, too [53]. The tunneling magneto resistance effect, however, is still not very well understood. In this work, some open questions for the simple case of tunneling through a vacuum barrier will be discussed.

Chapter 3

Experimental setup

3.1 UHV-chamber and surface analysis techniques

The Sp-STM system contains two chambers, a preparation-, a Sp-STM-chamber and a two stages load-lock (see Fig. 3.1). The two stages load-lock allows a fast transfer of samples and STM scanners into the main chamber without breaking the vacuum. This is important for Sp-STM measurements as we use special magnetic tips. Once a tip is crashed into a dirty or a nonmagnetic sample, the end of the tip can become nonmagnetic. Thus the tip will lose the magnetic sensitivity and needs to be changed. The first stage of the load-lock is an air-lock stage which is equipped with a small turbo pump. The second stage is an ion pump supported sample-store stage. The samples and scanners are first inserted into the air-lock stage. The pressure in the air-lock can reach $\sim 10^{-7}$ mbar within half an hour after starting the turbo pump (after short baking the vacuum with pressure of $\sim 10^{-9}$ mbar can be recovered). After that, the scanners and samples can be transferred into the sample-store stage and further inserted into the main chamber with a wobble stick.

The base pressure in the preparation- and Sp-STM chamber is 6.0×10^{-11} mbar. The preparation chamber is equipped with a differentially pumped ion gun for sample cleaning by Ar ion sputtering, an Auger electron spectrometer (AES), a low energy electron diffractometer (LEED), and several electron beam evaporators. The AES and LEED are positioned face to face. This allows to combine the electron source of the AES and the screen of the LEED to do medium energy electron diffraction (MEED).

After the sample preparation, the samples are transferred to the Sp-STM chamber by a small wagon. In the Sp-STM chamber, besides Sp-STM setup, an ion gun is used for in-situ tip cleaning and a magnet is used to crosscheck the magnetic origin of obtained contrast, respectively. Since a new approach of Sp-STM is used, it will be discussed in more detail in the following sections.

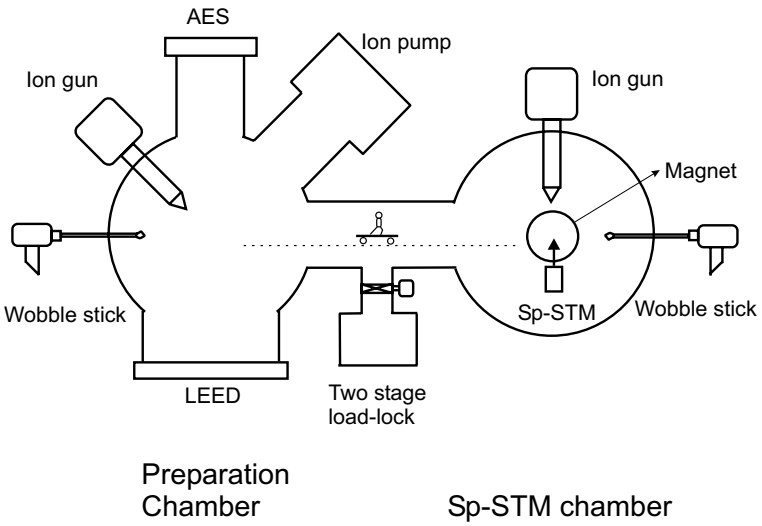

Figure 3.1: Top view of experimental setup. The system contains two main chambers, a preparation chamber, Sp-STM chamber and a two stage load-lock system.

3.2 Sp-STM setup

3.2.1 STM

Before going to the detailed setup of spin-polarized STM, I will give a short introduction of STM from which Sp-STM is modified. The principle of STM is based on the tunneling phenomena. As the electrons are quantum particles, they have wave like properties besides the particle like properties. Due to these wavelike properties, the electrons can tunnel through a barrier with the height higher than their energy. To understand the tunnel effect quantitatively, one needs to solve the Schrödinger equations as shown in the last chapter. For simplicity, one dimensional electron tunneling is considered. Electrons with momentum k and kinetic energy E that tunnel through a barrier which has a width of d and a height of V ($V > E$), have an imaginary momentum $i\kappa$ inside the barrier if their kinetic energy is lower than the barrier height. The Schrödinger equation can be solved analytically and the transmission (tunneling probability) T of the electrons is obtained as:

$$T \approx \frac{A}{d} e^{-2\kappa d} \tag{3.1}$$

The imaginary momentum $i\kappa$ depends on the kinetic energy E and barrier height V. Therefore, the tunneling probability decays nearly exponentially with the width of the tunnel barrier d. Assuming an barrier height of 4 eV, the intensity of the transmitted electrons becomes one order of magnitude smaller when the width of the barrier increases by 1 Å. Hence, the tunneling current is very sensitive to the barrier width and can serve as a feed-back to control the barrier width. Scanning tunneling microscopy is based exactly on this principle.

In a STM, three piezoes are used to control the movement of the tip in the x, y, and z-directions. The piezo coefficients of those piezoes are in the range of 10 nm/V. Hence, by applying a voltage on the piezo, one can control the movement of the tip in a very accurate way. For instance, 1 mV yields a change in distance of 0.1 Å. Applying a constant voltage between the tip and the sample and bringing the tip very close to the sample surface (several Å above the sample surface), a measurable tunneling current between the tip and the sample surface across the vacuum barrier is detected. The detected current serves as a feed-back to adjust the voltage applied to the piezo in the z-direction. In this way, the vertical movement of the tip is well controlled and a constant tunneling current is kept. Assuming that the local work function of the sample is homogeneous on the scanning area, a constant tunneling current means a constant tip-to-sample distance. Under this condition, the tip follows exactly the morphology of the sample surface when scanning along the x- and y-directions. Recording the vertical piezo voltage of each pixel, $V_z(x, y)$, and multiplying each value by the piezo coefficient c_z the morphology information $z(x, y)$ can be resolved:

$$z(x, y) = c_z V_z(x, y) \tag{3.2}$$

Hence, STM can measure the morphology of the sample surface with high resolution. Under favorable circumstances, atomic resolution can be achieved. As the electrons have a spin, it is possible to detect the sample magnetization if the spin information of the tunneling electrons can be resolved. Spin-polarized STM is the technique to resolve the spin information of the tunneling electrons and image the magnetic domain structure.

3.2.2 Sp-STM basic setup

The Sp-STM system is a modified commercially available micro STM system [29, 54]. Although this STM has only a very simple viton damping system which is not quite satisfactory for high resolution imaging measurements, it has the advantage that it doesn't use an eddy current damping system. This is important for our purpose as we are using a very soft magnetic tip. The coercivity of the tip is so small that the magnetization of the tip is easily disturbed by a small external field from, e.g., the magnets of an eddy current damping system.

In contrast to a normal STM in which a nonmagnetic tip is used, we use a very soft magnetic tip (see Fig. 3.2). A small coil is wound around the magnetic tip. The photograph of the real magnetic tip which is mounted on the top of the scanner head is shown in Fig. 3.3. A small AC current (in the range of 10 mA) is fed through the coil. Therefore, an AC magnetic field is generated and the longitudinal magnetization of the tip is periodically switched between the two well known energetically favored states of opposite magnetization. Hence, besides the nonmagnetic tunneling, an AC magneto-tunneling current is added due to the periodical magnetization alignment of the tip. One of the key points of this technique is that the frequency

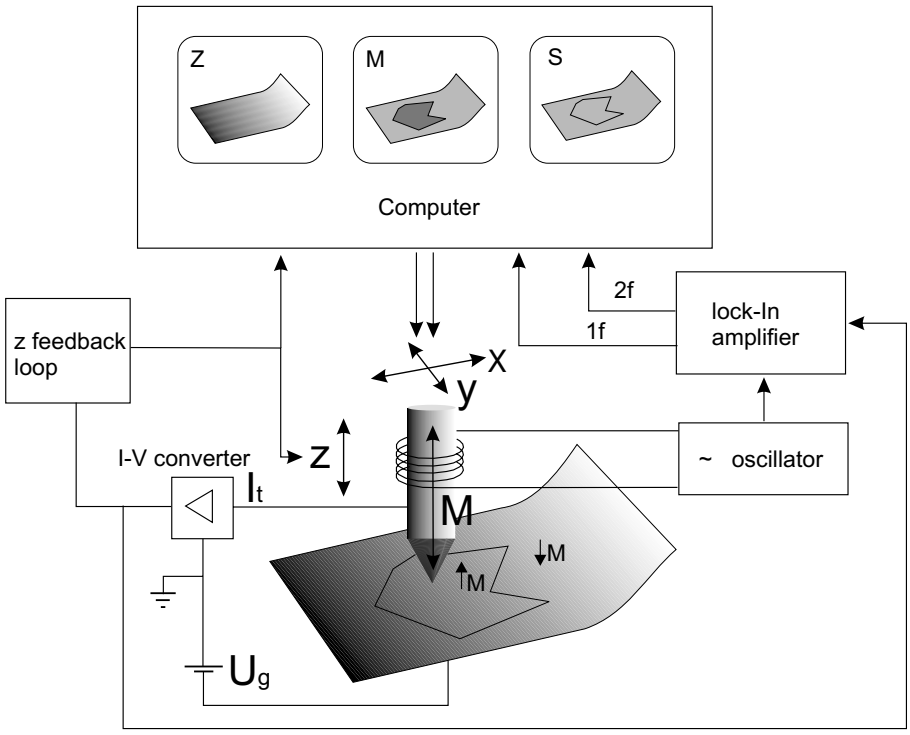

Figure 3.2: A simple sketch of spin-polarized scanning tunneling microscopy

of the AC current, $f = 40 - 80$ kHz, is chosen far away from any mechanical resonances of the STM and well above the cut-off frequency of the feed-back loop. Thus, the noise caused by mechanical vibrations can be minimized. As the frequency of the AC current is well above the cut-off frequency, only the DC component of the tunneling current enters into the feed-back loop to stabilize the tunneling current and keep a constant tip-to-sample distance. Mapping the vertical distance change on the sample surface, one obtains the morphology of the sample surface as an usual STM measurement. The stabilization of the DC tunneling current is very important for the magnetic imaging as the magneto-tunneling current is proportional to the DC tunneling current. Any changes of the DC tunneling current induces additional noise.

Based on the TMR effect, the periodical switching of the tip magnetization causes an AC tunneling current. This AC tunneling current is sensitive to the magnetization orientation on the sample surface and can be measured with a phase sensitive lock-in amplifier. As the magneto-tunneling current is a linear function of the magnetization alignment between the tip and sample surface as discussed in previous chapter, and the magnetization of the tip is switched between two well defined states of longitudinal magnetization, the projection of the sample surface magnetization to the magnetization of the tip is measured and perpendicular magnetic contrast is achieved.

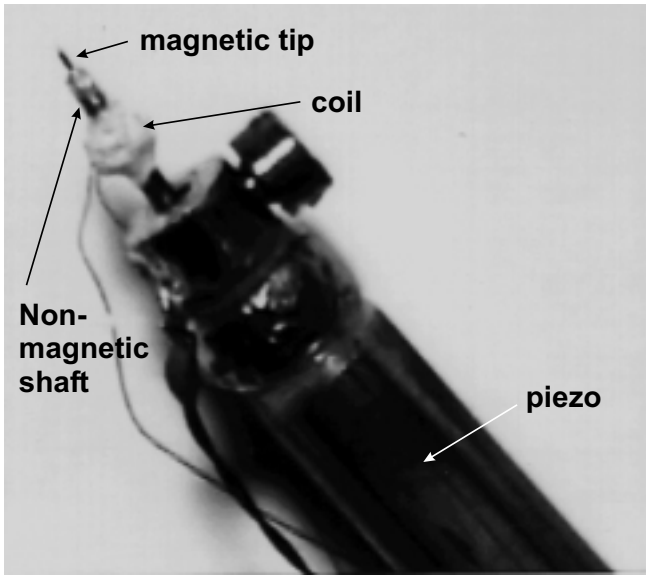

Figure 3.3: A picture of the Sp-STM scanner end

As the small coil used to switch the tip magnetization is located just around the tip, i.e., close to the signal line of the tunneling current, besides switching the tip magnetization the coil also generates an induction signal of the same frequency. The induction signal can also be picked up by the preamplifier and enters the lock-in amplifier. Therefore, an unwanted background signal is generated in the tunneling current besides the magneto-tunneling current. To subtract the background and obtain the pure magneto-tunneling signal, we retract the tip from the sample surface. When the tip is retracted the tunneling current becomes zero, i.e., there is no magneto-tunneling current. Only the induction generated by the AC current through the small coil remains. In this way, the background signal of the lock-in, which is caused by the induction of the coil, is obtained and can be used for checking the relative sign of magnetization component in the obtained structure.

In addition to magnetic imaging, in the limit of soft magnetic materials or strong stray fields of the tip, the sample magnetization can oscillate with the same frequency due to the influence of the stray field of tip. This behavior is related to the local magnetic susceptibility. As the change of both the tip and sample magnetization are of the same frequency and the TMR effect is proportional to the scalar product of both magnetization, a double frequency signal is generated. It can be obtained in the $2f$ channel of the lock-in amplifier.

In a brief summary of this technique, we can obtain the morphology in the z channel, the magnetic domains in the $1f$ channel of the lock-in amplifier, and the local magnetic susceptibility in the $2f$ channel of the lock-in amplifier. Moreover, these three images can be obtained simultaneously.

3.3 The magnetic tip

3.3.1 Tip material

To avoid vibrations of the tip during switching of its magnetization, special care has to be taken in the choice of the tip material. For optimal performance, one needs low coercive fields of the material to minimize magnetic dipole forces between the tip and the exciting coil. One needs a vanishing magnetostriction of the tip material to prevent changes of the tip length during switching. Besides, the magnetization loss should be low to avoid energy dissipation and by this periodic heating and thermal expansion of the tip and the tip material should have also low saturation magnetization to minimize the influence of the tip stray field on the sample. For these reasons, the tip material is carefully selected from an amorphous metallic glass of the FeCoSiB family with high Co concentration. The material offers extremely low coercivity in the range of 50 μT with high initial susceptibility, vanishing magnetostriction ($< 4 \times 10^{-8}$) and low saturation magnetization of only 0.5 T combined with low magnetization losses at frequencies up to 100 kHz. The magnetic tips are made of Co based amorphous wires with the diameter of 130 μm. The wire is obtained by the in-rotating-water quenching technique [55]. The FeCoSiB alloy ingots were molten in a quartz crucible with a 130 μm hole through which the melt was injected into a rotating water bath. The magnetic behavior of amorphous magnetic wires strongly depends on the concentration of different components. Co-rich alloys with adequate additives exhibit vanishing magnetostriction and do not show bistability [56]. Proper thermal treatments can reduce the internal stresses coming from the fabrication procedure and by this achieve low coercive fields, high initial susceptibility and vanishing magnetostriction [57]. The magnetic wires used in the experiments shown in this thesis have been kindly provided by M. Vázquez [58].

3.3.2 Etching of tips

Electrochemical etching is a common technique for preparing sharp STM tips. A sharp tip is crucial for Sp-STM as imaging with a magnetic tip needs microscopically sharp tips to minimize the stray field of the tip. Hence, we use electrochemical etching to produce the magnetic tip as this method is known to result in especially sharp tips [59].

As the tip material is a Co based FeCoSiB alloy, the material contains four different elements. We use a mixture of HCl and HF acids to etch the magnetic tip. Particularly, the HCl acid is used for etching Fe and Co and the HF acid for Si and B. The detailed concentration of the etching acid is 100 : 10 : 5 in volume for ion free water, 32% HCl and 40% HF. As shown in Fig. 3.4a, a magnetic wire of about 5 mm long is glued to two copper pipes at both ends to make it easier to handle. A Pt ring is used as one of the electrodes and the Cu pipe is served as the other one. First, the Pt ring is put into the acid and slowly pulled up to form a thin acid

membrane on the ring. The ring has to stay horizontally to obtain a homogeneous membrane. (A tilted ring usually causes the breaking of the membrane.) After the membrane is formed, the magnetic wire is brought to the proper position into the membrane. A DC voltage is applied between the Cu pipe and Pt ring to produce the etching current. As the Fe, Co ions are positive ions, the Cu pipe/Pt ring is connected as a positive/negative electrode, respectively, to carry these positive ions away from the magnetic wire so as to produce a sharp tip. The speed for etching influences the shape of the etched tip. This is due to the fact that different etching currents cause different ion distributions inside the membrane so as to induce different etching speed distributions. Usually, the etching speed is higher in the center and lower at the surfaces of the membrane. In this way, a tip is produced. If the etching speed is too fast, the etched tip usually is a dull one. If the etching speed is too low, the tip is too long and pointed. This kind of tip usually is not stable enough for STM imaging. Additionally, a good shape of the magnetic tip can avoid magnetic pinning which is not good for the completely switching of the tip magnetization. Hence, it is quite important to choose a correct speed to etch the Sp-STM tips. In our case, we use a two-step etching method. To control the speed of the etching, we choose a multimeter to select the desired current for etching. At the beginning, we used 1 mA for the etching current. The etching process is controlled under a microscope. When the diameter of the magnetic wire at the center of the membrane becomes around one quarter of its origin value, the tip already shows a good shape. After this pre-etching for the shape, we reduce the etching current to around 200 μA to form a very sharp apex.

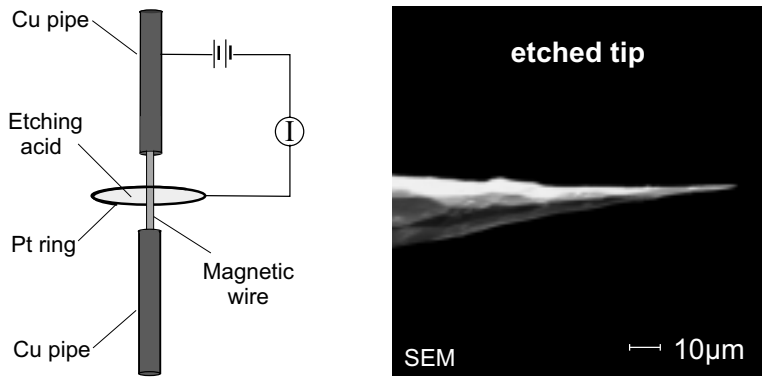

Figure 3.4: A simple sketch for etching (a) and a typical tip etched by this method (b). The image was kindly provided by Dr. G. Steierl.

Fig. 3.4b presents a scanning electron microscopy (SEM) image of the end of magnetic tip electrochemically etched with the technique above mentioned. It shows a conical like tip end with an opening angle of $\approx 12^{\circ}$.

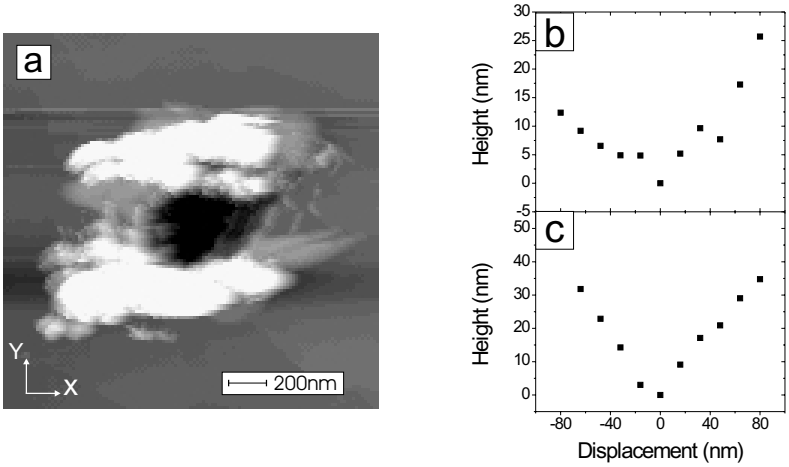

Figure 3.5: (a) A STM image of the position where a tip was crashed. (b)&(c) are line scans across the very end of the crash along the x&y- directions, respectively.

To estimate the sharpness of the tip further, we performed a simple measurement. We gently crashed the tip into the sample surface and after that we made a topographic measurement at the tip crashing position. When the tip was crashed it made a hole on the sample surface. The shape of the hole reflects the shape of the tip. Although it indicates the sharpness of the tip after the crash only, it still can give a good estimation of the sharpness of the tip when the tip was not severely crashed.

Fig. 3.5a presents the topography of the position where the tip was crashed. It shows a hole about 60 nm deep in the center of the image. Fig. 3.5(b) and (c) show the line scans across the very tip end along x- and y-direction, respectively. We can see that the diameter of the end of the tip is smaller than 20 nm indicating a sharp tip. Usually, the tip is getting worse after crashing. The freshly prepared tips which are normally used in our measurement should be sharper than 20 nm.

3.3.3 The stray field of the tip

Due to the magnetization of the tip a magnetic stray field is created outside its volume. This stray field is important for Sp-STM measurement as it might influence the domain structure of the sample. Since the tip is of mesoscopic size, it is impossible to perform complete micromagnetic calculations for the entire tip to obtain its stray field. However, one can still make a rough estimation of the stray field under certain approximations.

The stray field of the tip comes macroscopically from its shape, and microscopically from the apex of the tip. In the following, the magnitude of the stray field in both the macroscopic

and microscopic points of view will be discussed.

To estimate the stray field, we use the formula which describes the interaction between two magnetic dipoles [60]. In the general case, the potential energy of the dipole interaction between two magnetic dipoles $\vec{M}_1$ and $\vec{M}_2$ which are separated by a distance of $\vec{r}$ is given by

$$U = \frac{1}{4\pi\mu_0 r^3}\{\vec{M}_1 \cdot \vec{M}_2 - \frac{3}{r^2}(\vec{M}_1 \cdot \vec{r})(\vec{M}_2 \cdot \vec{r})\} \tag{3.3}$$

with μ_0 the magnetic permeability in the vacuum ($4\pi \times 10^{-7}$ Hm^{-1}). Due to the shape anisotropy of the tip, the magnetization of the tip is along the magnetic wire axis. The stray field at the position directly below the tip should be along the tip axis due to the symmetry. Therefore, we choose the magnetic moment of the test magnetic dipole, i.e., $\vec{M}_2$ to be along the magnetic wire direction. As $\vec{M}_1$ and $\vec{M}_2$ are in the same direction, the formula can be simplified into

$$U = \frac{3M_1M_2}{4\pi\mu_0 r^3}(\frac{1}{3} - \cos^2\theta) \tag{3.4}$$

in which, M_1,M_2 are the magnitude of magnetization of the two magnetic dipoles, respectively, and θ is the angle between the direction of magnetization and the line between the two dipoles. Assuming the magnetization of the test dipole to be 1, the stray field of the other dipole can be easily written as

$$h_{stray} = \frac{3M}{4\pi\mu_0 r^3}(\frac{1}{3} - \cos^2\theta) \tag{3.5}$$

in which, M is the magnetization of the tip. However, h_{stray} is only the stray field of one magnetic dipole. In order to calculate the real stray field, it is necessary to integrate over the volume of the tip.

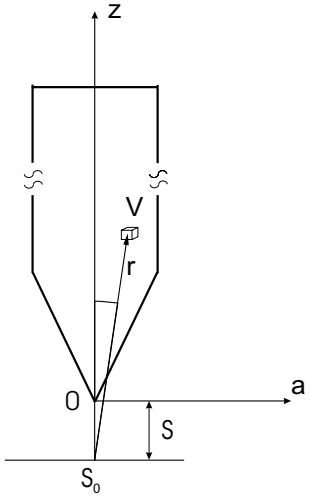

Figure 3.6: A simple sketch for the calculation of the stray field

As the tip is rotational symmetric around z-axis, cylindric coordinates are introduced to simplify the calculation. As shown in Fig. 3.6, the end of the tip is chosen as the origin, the z-axis/a-axis are chosen along/perpendicular to the magnetic wire direction. Assuming a separation S between the tip and the sample surface, the distance between the unit volume ΔV shown in Fig. 3.6 and the sample surface position directly under the tip can be obtained as $r = \sqrt{(z+s)^2 + a^2}$. Similarly, the angle between the $\vec{r}$ and z-axis θ can be obtained by $\cos\theta = \frac{z+s}{r} = \frac{z+s}{\sqrt{(z+s)^2+a^2}}$. Putting this into Eq. 3.5 and integrating over the whole magnetic volume of the tip, we can calculate the stray field of the tip at the sample surface directly under the tip, i.e., the stray field at the position S_0 shown in Fig. 3.6,

$$\begin{aligned} H_{stray} &= \int h_{stray} dV \\ &= \int\int \frac{3M}{4\pi\mu_0[(z+s)^2+a^2]^{\frac{3}{2}}}[\frac{1}{3} - \frac{(z+s)^2}{(z+s)^2+a^2}]2\pi a dz da \end{aligned} \tag{3.6}$$

In the following, the stray field caused by the macroscopic shape of the tip will be discussed. In Fig. 3.7a, a typical macroscopic shape of the tip is shown. The wire is 130 μm in diameter. The usual length to the tip is roughly 2 mm. The end of the tip has an opening angle α. For simplicity, the detailed sharpness of the tip end is neglected, i.e., the tip is assumed to be infinitely sharp at the end in this macroscopic shape estimation. Therefore, the stray field caused by the macroscopic shape of the tip can be estimated using the formula given above and taking the boundary showing in Fig.3.7a.

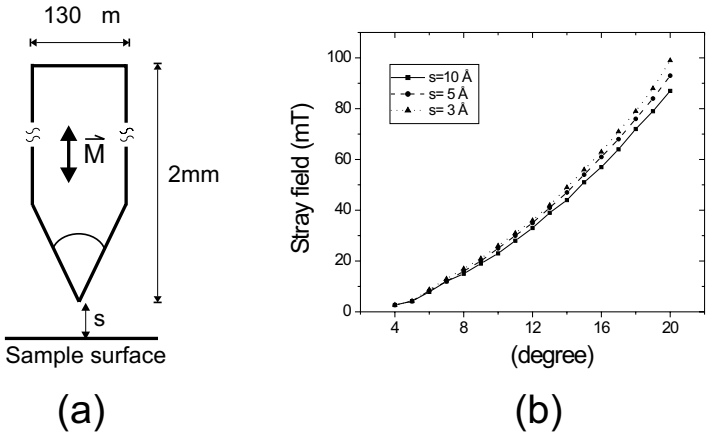

Figure 3.7: The macroscopic shape of the Sp-STM tip (a) and the dependence of the stray field of the tip on its shape, i.e., the opening angle α for 3 different tip-sample separations (b).

Fig. 3.7b shows the stray field at the sample surface directly under the tip for 3 different tip-sample separations as the function of the open angle α. The typical tip-sample separation during

imaging is around 5 Å. The stray field strongly depends on the opening angle. As expected, the smaller the angle, the smaller the stray field. With the etching technique mentioned above, the opening angle α can be controlled very well. Usually, α is between 8° and 14° (See Fig. 3.4b). Hence, the stray field caused by the macroscopic shape of the tip is in the range of 15 mT to 40 mT. Due to the decrease of the stray field with the separation distance to the third power (see Eq. 3.5), most of the stray field comes from the end of the tip. Therefore, further increase of the total length of the tip only causes a slight change of the stray field. To quantify this effect, further calculations were performed by extending the total length to 3 mm, i.e., 1 mm longer. If the tip to sample distance is 5 Å, the stray field is only increased by 0.04 mT. This kind of influence can be neglected.

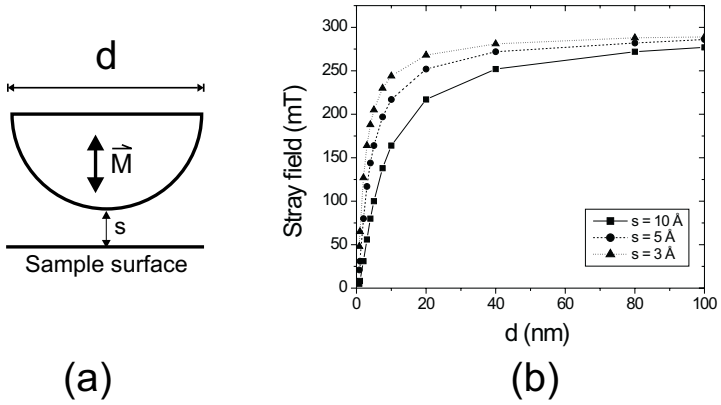

Figure 3.8: The microscopic shape of the Sp-STM tip end (a) and the dependence of the stray field of the tip on its shape, i.e., the diameter of the hemisphere for 3 different tip-sample separations (b).

In the following, the stray field induced by the microscopic shape of the end of the tip will be discussed. As shown in Fig. 3.8a, the end of the tip usually has a shape of a hemisphere. Similar to the calculation presented above and taking the boundary condition of the hemispheric shape, the stray field of the tip versus the diameter of the hemisphere is calculated. The results for 3 individual separations between the tip end and the sample surface are shown in Fig. 3.8b. A strong dependence of the stray field on the diameter of the hemisphere is found. If the diameter of the hemisphere is larger than 20 nm, the stray field of the tip is above 200 mT. For a further increase of the diameter, the stray field seems to approach a saturation value. However, if the diameter of the hemisphere is smaller than 5 nm, the stray field of the tip is below 100 mT and even below 50 mT if the diameter of the hemisphere is less than 2 nm. Hence, a sharp tip is highly required for Sp-STM measurement to minimize the influence of the stray field. The best way to obtain sharp tips is the electrochemical etching. For the details of the technique, please

see Sec. 3.3.2.

3.4 In-situ sample and tip preparation

Both the Co(0001) sample and the magnetic tips were cleaned in-situ by sputtering with 1 kV Ar^+ ions at an angle of incidence of 45°. The sample was annealed afterwards to 570 K for 20 minutes. Annealing to higher temperatures was avoided to stay below the well known hcp-fcc phase transition of Co at ≈ 690 K. During a heating cycle through the phase transition, a Co single crystal specimen can be destroyed [61]. The cleanness and the surface quality were checked by AES and LEED.

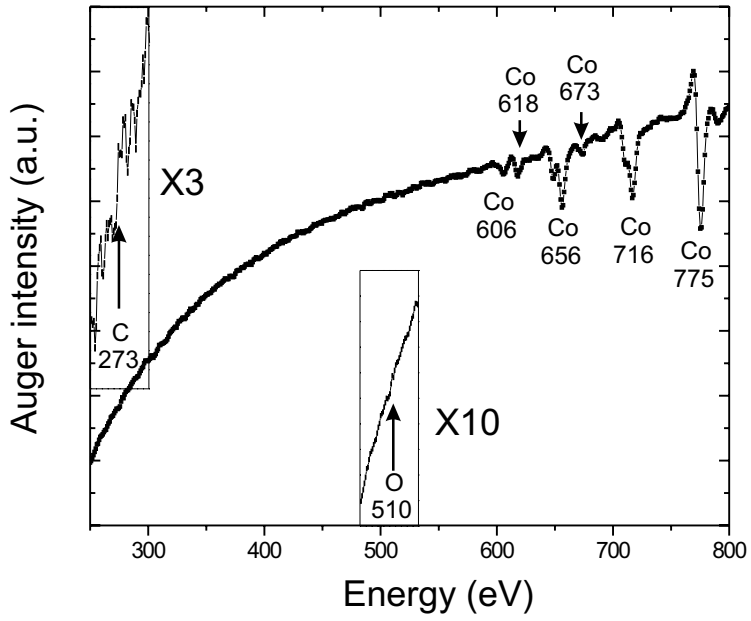

Figure 3.9: The Auger spectrum for a clean Co(0001) surface. The inserted parts are shown in higher sensitivities.

Fig. 3.9 presents a differential AES spectrum of the Co(0001) surface after annealing. All fine features of Co AES spectra can be observed. A weak C peak at 273 eV and an O peak at 510 eV are just within the noise level of our AES. The C and O peaks are less than 3% and 0.5% of the Co peak at 775 eV, i.e., a rather clean Co surface is obtained.

Fig. 3.10 presents a LEED image of the Co(0001) surface at 150 eV. It shows the expected sixfold diffraction pattern with sharp spots and low background intensity indicating a good

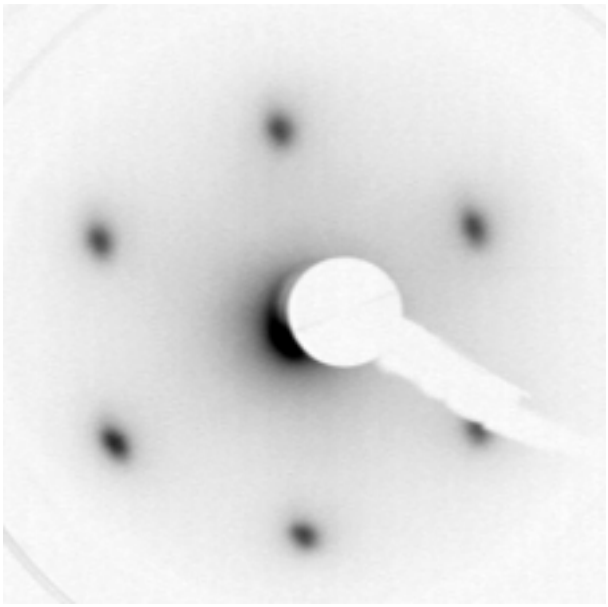

Figure 3.10: A low energy electron diffraction pattern of Co(0001) surface at $E = 150$ eV.

surface quality of the Co surface with low defect densities.

The tip can be directly used for Sp-STM measurement after sputtering. When the tip absorbs a nonmagnetic adatom at the tip end, it can be further cleaned with the field emission by applying a high bias voltage pulse. The bias voltage used for field emission depends on the detailed sharpness of the tip.

Chapter 4

Results and discussion

4.1 Magnetic imaging

Spin-polarized scanning tunneling microscopy is a new technique. For a new magnetic imaging technique, it is necessary to demonstrate that the observed contrast is real and related to magnetic domains. One might consider that the contrast could be caused by some other, static characteristic like compositional, structural, or orientational variations of the sample surface. The observed magnetic contrast (Fig. 4.1a), however, is quite different from the morphology image (Fig. 4.1b) of the same area. This rules out that the direct connection between the observed magnetic contrast and the morphology. As the contrast can be obtained on a well defined, clean single crystal surface, i.e., a Co(0001) surface, compositional or orientational variations of the sample surface can be excluded as the origin of the contrast as well. To rigorously prove the magnetic origin of the contrast observed by Sp-STM, two procedures have been carried out. First, the influence of an external field on the observed structures is studied, and second, the results of the new technique are compared with those obtained with a standard magnetic imaging technique, e.g., magnetic force microscopy (MFM).

4.1.1 Influence of the external field

The observation of domain wall movements and changes in domain structure during application of an external magnetic field is one of the easiest and most evident ways for checking the magnetic contrasts. When the strength of the applied external field is large enough, the field should be able to change the magnetization of the sample surface. Hence, the observed contrasts should exhibit some changes and the walls between domains should be moved by the external field if they are really of magnetic origin.

Fig. 4.1a shows a domain structure of a Co(0001) surface obtained with a dull tip of unknown magnetization direction. There are two regions of different contrast observed on the sample

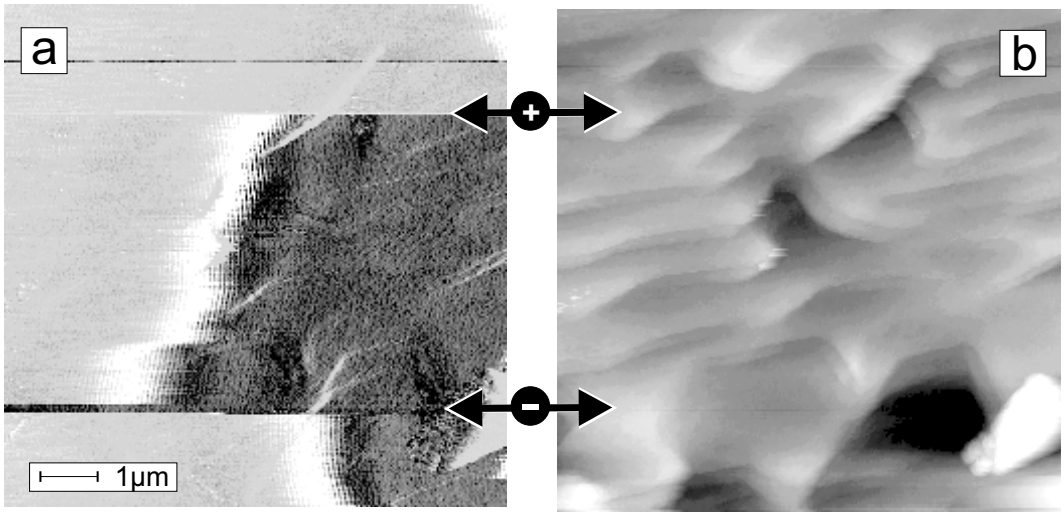

Figure 4.1: Sp-STM image of the domain structure (a) and topography (b) of the same area of the surface of Co(0001). When applying external magnetic field pulses of 5 mT during scanning (indicated by the arrows), the domain wall is moved to left or right depending on the direction of the field. No movement is observed in the topography.

surface. The image is taken by recording line scans from bottom to top. In the lower region, the domain wall is near the center. When applying a short pulse of a homogeneous magnetic field of the order of 5 mT perpendicular to the sample surface pointing downwards, the observed domain wall is moved a couple of μm to the left side during the scanning and the dark domain area becomes bigger. At the top part of the image, another pulse of magnetic field is applied in the opposite direction, i.e., along the magnetization direction of the light domain. The reversed situation is found and the domain wall is moved to the opposite direction, to the right border of the image. As the sample is magnetic, applying an external field might cause a movement of the whole sample so as to induce an additional movement of the domain wall. The effect has been cross-checked by a careful examination of the simultaneously obtained topography of the same area, Fig. 4.1b. The continuous step bunches prove that there is no observable movement in the topography. Hence, the movement of the whole sample can be safely excluded. Since the tip was a double tip, the step edges are displayed doubled.

The observation of the movement of a domain wall in an applied external field pulse while no movement of the topography is found, unambiguously proves the magnetic origin of the spin-signal. The observed structures are indeed magnetic domains and domain walls on the surface. Additionally, this illustrates that spin-polarized STM can be used for high resolution studies of domain wall motion dynamically during the scanning. The magnetic field used to move the domain wall, however, is much larger than the alternating field used to switch the magnetization of the tip. Therefore the tip magnetization is fixed for the duration of the pulse. Thus, during

the short magnetic pulses, the lock-in signal is lost and neither domain walls nor domains are observed in the parts of Fig. 4.1a indicated by the arrows.

4.1.2 Comparison with standard magnetic imaging techniques

The observed movement of the domain structure in an external field with no movement of the topographic signal obviously gives a strong proof of the magnetic origin of the obtained contrast. As an additional check, one should compare the obtained domain structure with the domain structure imaged by standard techniques. (The domain structure of the sample should be independent of the magnetic imaging techniques.) Hence, the comparison of the observed contrast with the domain structure of the same sample imaged by a standard magnetic domain imaging technique can serve as a straightforward procedure to test our new magnetic imaging technique.

Magnetic force microscopy (MFM) is one of the well known and easiest magnetic imaging techniques. With a tip which is magnetized along the tip axis, MFM is also sensitive to the perpendicular component of the sample magnetization. Further, the resolution of MFM is around several 10 nm [11]. It is closer to the resolution of Sp-STM than the resolution of the other standard magnetic imaging techniques. Hence, MFM is one of the best candidates for this purpose.

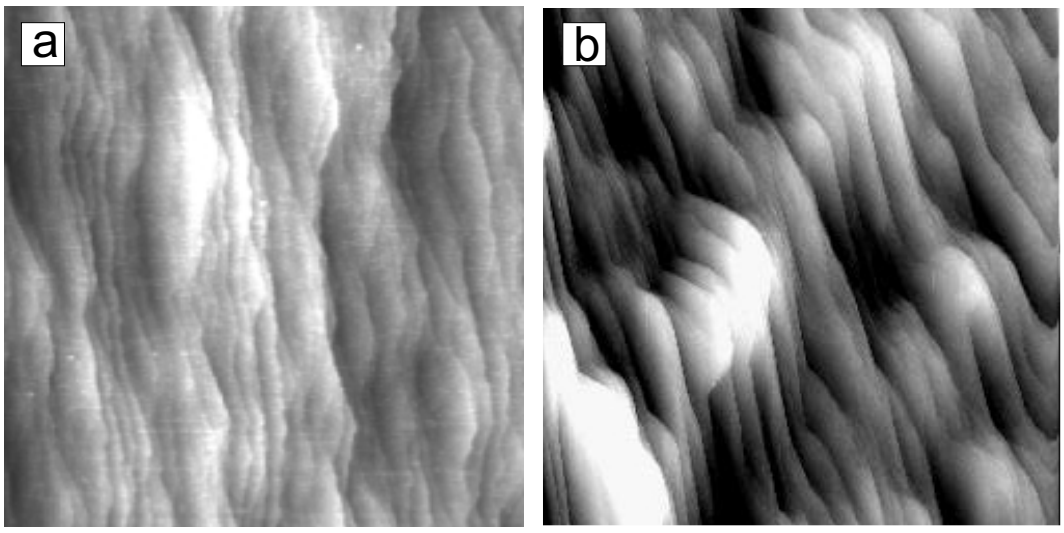

Figure 4.2: Typical topography images of Co(0001) surface obtained by MFM in air (a) and Sp-STM in UHV (b). Both images are of 8×8 μm^2.

The same Co(0001) crystal was chosen for both Sp-STM and MFM measurements. Tunneling images of the topography as well as the magnetic structure were recorded by Sp-STM at room temperature in ultra high vacuum. After the Sp-STM measurement was performed, the crystal

was taken out from the vacuum for the MFM measurement. The MFM images were taken at room temperature as well. Since the measurement was performed in air, the crystal was covered with native oxide. Nevertheless, the topographic images obtained with MFM at the same time as the magnetic images showed a similar terrace structure as the topographic STM images obtained in vacuum (see Fig. 4.2).

Single crystal hcp Co has a uniaxial anisotropy with the easy axis along the c-axis, i.e., perpendicular to the selected (0001) surface. Due to the natural 6-fold in-plane symmetry, it has a 6-fold in-plane magnetic anisotropy. Because the stray field energy and the perpendicular magneto-crystalline anisotropy energy are of the same order of magnitude and the crystal has a 6-fold in-plane anisotropy, the domain structure of Co(0001) shows complex surface closure domains. Usually, the crystal has a dendritic like domain pattern with closure domains that successively branch into finer structures as shown in Fig. 4.3.

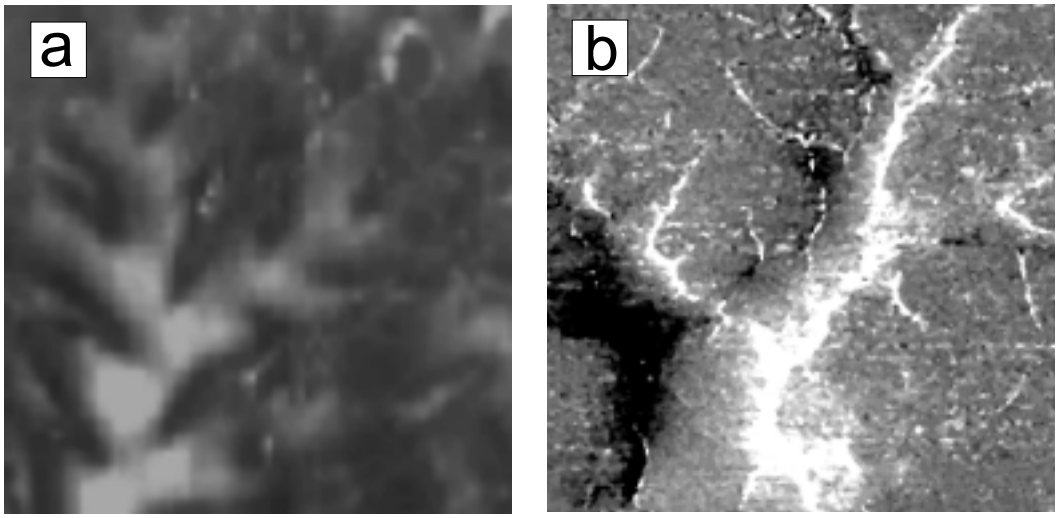

Figure 4.3: MFM (a) and Sp-STM (b) images of the branching closure domain pattern of Co(0001). Both images are of the same scale of 4×4 μm^2

Fig. 4.3 presents a MFM and a Sp-STM image of this typical branching structure. The structures observed with both techniques are similar, although the images were not recorded on the same area of the surface. At this magnification, the resolution limit of MFM of the order of several 10 nm to 100 nm becomes obvious (see Fig. 4.3a). The branch structure seems to be blurred in comparison with the images taken with Sp-STM at the same magnification (see Fig. 4.3b) and the ends of the branches seem to be rounded, while the Sp-STM image shows pointed ends of the branches.

Fig. 4.4 presents another characteristic domain structure of Co(0001) obtained by MFM (a) and Sp-STM (b). It shows that the roots of the domain branches forming a ring-like structure.

This may be due to the fact that these kind of ring-like structures minimize the domain wall energy and the stray field energy more efficiently. Both images are nearly the same. As our STM only has a simple viton damping system, mechanical noise may show up in the images when the contrast is not high enough to suppress it. Fig. 4.4b probably is one of these cases.

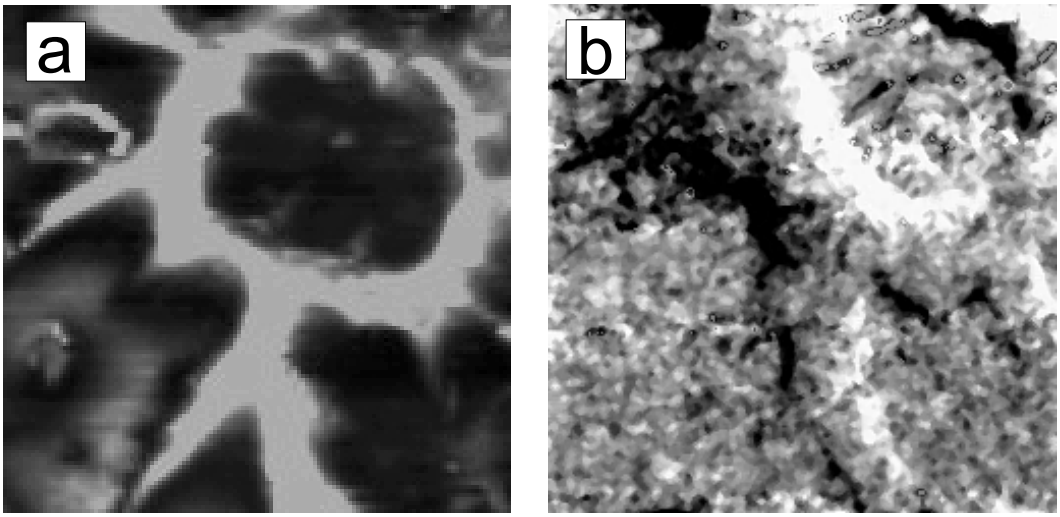

Figure 4.4: MFM (a) and Sp-STM (b) images of the ring-like structure of perpendicular magnetic pattern of Co(0001). Both images are of the same scale of 4×4 μm^2

It is evident that the images obtained with both MFM and Sp-STM are similar. They show identical features even though they are not recorded on the same areas of the sample surface. The maximum scan ranges of most high resolution imaging techniques like Sp-STM and MFM are rather limited. They are typically 10 μm for STM and 50 μm for MFM. Due to this limited scan range, it is nearly impossible to image the domain structures of the very same area with both techniques. Thus large area scans at many arbitrary chosen positions of the sample surface were performed. Fig. 4.5 presents one of these images. It clearly shows the dentritic structures almost in the whole image and a ring-like structure forms at the upper right part of the image. Similar images can also be seen with Sp-STM (Fig. 4.3b and Fig. 4.4b). The larger size images of MFM at different positions of the sample surface show similar structures (see Fig. 4.5) except that the sizes of the branches and the rings can be different at different positions. This identifies that the domain images shown in both figures are the typical vertical magnetic structures of the Co(0001) surface. Additionally, these two typical magnetic domain patterns of the Co(0001) are also found by Kerr microscopy [62] and SEMPA [63]. They are obtained even on different samples.

The similarity between the domain images obtained by Sp-STM and the images achieved with MFM, gives a second evidence for the magnetic origin of the obtained contrast of Sp-STM.

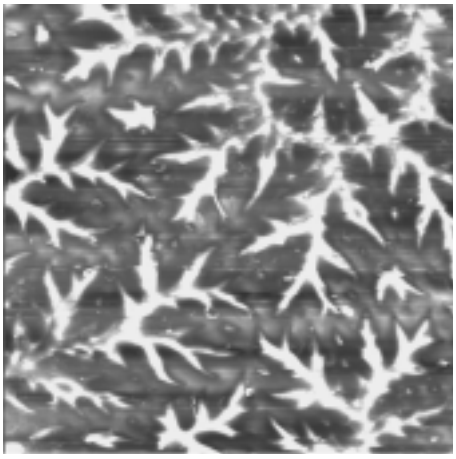

Figure 4.5: 10×10 μm MFM image on Co(0001) surface.

So far, we have proven that magnetic structures can be imaged with Sp-STM. In the following, the contrast mechanism of Sp-STM will be discussed. Besides the TMR effect, also magnetic forces act between the tip and the sample as both are magnetic. These forces, do not lead to noticeable mechanic vibrations and with this to changes of the tunneling current during magnetic switching of the tip, since in contrast to MFM, where the tip is mounted on a soft cantilever, in the Sp-STM the tip is rigidly fixed directly to the scanner. Hence, changes of the distance between the tip of the Sp-STM and the sample have to be accompanied by elastic deformations of the tip. The magnetic forces that occur in the Sp-STM are 4 to 5 orders of magnitude too small to cause noticeable fluctuations in the tunneling current by an elastic deformation of the tip. Hence, we can exclude a MFM mechanism to be responsible for the contrast in Sp-STM. Besides, we did test experiments in vacuum to verify that the contrast is indeed due to spin-polarized tunneling. We imaged the Co(0001) surface after a dosage of 10 Langmuir of oxygen and did not observe any contrast after this dosage in agreement with a surface sensitive contrast mechanism like tunneling and in contrast to the mechanism of MFM which is not even influenced by the ambient conditions in atmosphere. Further, we recorded the dependence of the contrast on the tunneling voltage and the gap width. The dependence on these two parameters is discussed in detail in section 4.4 and 4.5 and are consistent with spin-polarized tunneling. Additionally, for a hypothetical MFM like contrast that is caused by a small vibration Δd, the variations in the tunneling current ΔI are given by $\Delta I(d) = \Delta d \frac{\partial I(d)}{\partial d}$. Hence, by measuring both the contrast and tunneling current as a function of the tip-to-sample distance simultaneously, an MFM like contrast mechanism can be falsified.

Fig. 4.6 shows the result of the comparison between the observed magnetic signal and the hypothetical effect induced by vibrations. The experiment was performed on a Co(0001) surface on a small area which contains only two domains and one domain wall. The magnetic contrast

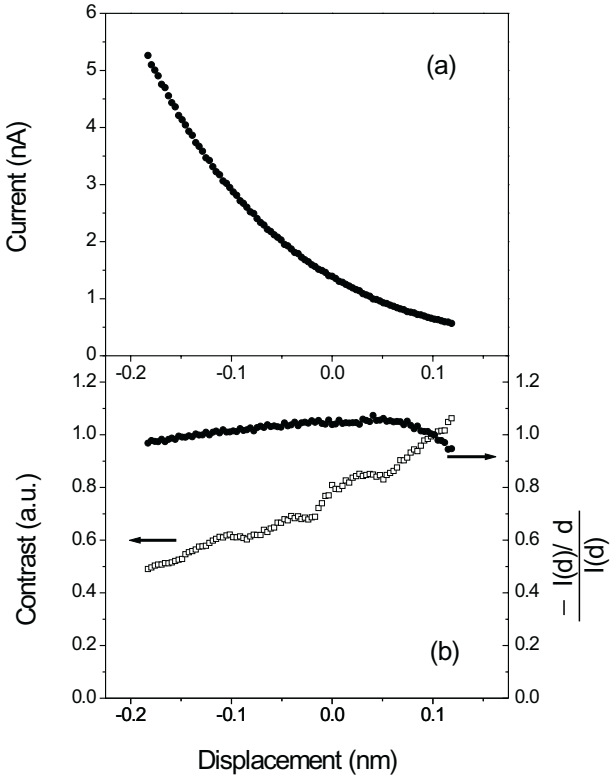

Figure 4.6: (a) Typical tip-to-sample distance dependence of the tunneling current. The sign of the displacement means the tip is closer (−) or further away (+) from the sample. (b) The comparison between the observed distance dependent magnetic contrast (open symbols) and the hypothetical vibrational contrast (filled symbols), i.e., $\frac{-\partial I(d)/\partial d}{I(d)}$. For comparison, both curves have been normalized to the same scale.

is obtained as the difference of the lock-in signals across the domain wall and normalized by the tunneling current. The tunneling current as well as the magnetic contrast were recorded simultaneously while changing the tip-to-sample distance. Fig. 4.6a, the tunneling current versus the tip-to-sample distance change shows a typical exponential dependence as expected in normal tunneling experiments. The derivative of the tunneling current I with respect to the distance d was calculated numerically. From the derivative, the hypothetical contrast $\frac{-\partial I(d)/\partial d}{I(d)}$ due to vibrations of the tip was calculated. As shown in the plot of Fig. 4.6b, it first increases a little bit and then slightly decreases (roughly 10% of the highest value) when the tunneling tip is closer to the sample surface. Our measured magnetic contrast, however, shows a strong decrease with decreasing tip-to-sample distance and deviates from the hypothetical vibrational

contrast significantly. This proves that the contrast we observed is not caused by a vibration related effect. We assumed that the vibration Δd caused by the magnetic force is constant during changing the tip-to-sample distance. If the change of the Δd is taken into account, the difference between the vibration effect and the measured magnetic contrast would be even bigger as the magnetic force becomes stronger when the tip is closer to the sample surface.

4.1.3 Estimation of resolution

From the comparison between the images obtained by Sp-STM and MFM, we can get a first glimpse of the lateral resolution of Sp-STM in comparison with that of MFM (see Fig. 4.3). The different resolutions come from the different principles that both techniques are based on. As introduced in the previous chapter, spin-polarized scanning tunneling microscopy is based on the tunneling magneto resistance effect. It measures the magneto-tunneling current which is part of the total tunneling current. Magnetic force microscopy, however, is based on the magneto-static interaction between tip and sample. In the following, the resolution of both techniques are compared more quantitatively in a simple model.

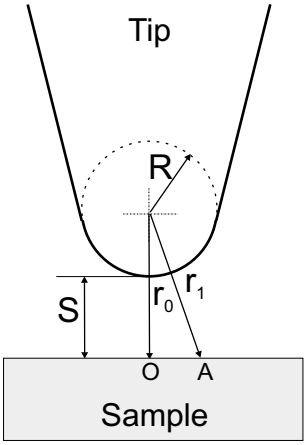

Figure 4.7: Schematic picture of Sp-STM/MFM geometry. The probing tip has an arbitrary shape but is assumed locally spherical with a radius of curvature R, where it approaches nearest the sample surface. The distance of nearest approach is S. O is the position nearest to the tip end. OA is the radius of the effective area which has considerable contribution to the contrast.

Identical tips with hemispheric ends are assumed to be used in both techniques (see Fig. 4.7). The radius of the hemisphere is R and it is separated by the distance S from the sample surface. To specify the resolution, an effective area which has a considerable contribution to the measured signal needs to be defined. It is defined as the area in which the measured effect (tunneling current in Sp-STM and magnetic force or its gradient in MFM) at the boundary is 10% of that at the center. The distances from the center of the hemisphere at the tip end to the effective

area center and boundary are r_0 and r_1, respectively. The resolution is defined as the radius of the effective area, OA.

In Sp-STM, the magneto-tunneling current is measured to obtain the magnetic structure of the sample. The estimation of the lateral resolution should be the same as in the case of STM. The lateral resolution of STM has been estimated by Tersoff and Hamann [64]. Here, we give a similar but simpler estimation. The tunneling current exponentially decays with the distance between the end of the tip and the sample surface. This exponential decay depends on the imaginary wave vector inside the barrier. Typically, the tunneling current decreases one order of magnitude when the separation is increased by 1 Å. We use this to estimate the lateral resolution. The distance between the center of the hemisphere and center of the effective area r_0 is 1 Å smaller than the distance between the center of the hemisphere and the boundary of the effective area r_1, i.e., $r_1 = r_0 + 1$ Å. With this, we can estimate the lateral resolution which is:

$$OA = \sqrt{r_1^2 - r_0^2} \approx \sqrt{2(R+S)\text{Å}} \tag{4.1}$$

The separation between the tip and the sample surface depends on the details of the bias voltage, the tunneling current is used and the sharpness of the tip. Typically, the tip is several Å above the sample surface. Here, we take $S \approx 5$ Å. Assuming the end of the tip is 5 nm in radius ($R = 50$ Å), the resolution of Sp-STM can be estimated to be ≈ 1 nm.

Magnetic force microscopy is based on the magneto-static interaction between tip and sample. In the experiments, two different modes can be chosen to obtain the magnetic contrast, i.e., either the magnetic force or its gradient is measured. An analysis similar to the one used above is taken to estimate the resolution for each case. In this analysis, the effective tip of the magnetic force microscopy is assumed to be a sphere with a radius of R. As shown in Eq. 3.4, the magnetic force between two magnetic moments is proportional to $\frac{1}{r^3}$ with r the distance between them. Assuming that the magnetic force between a local moment at position A and the magnetic tip is 10% of the interaction between the local moment at position O and the tip, we obtain that $r_1^3 = 10r_0^3$. Therefore, the resolution of MFM in the magnetic force mode can be estimated to be,

$$OA = \sqrt{r_1^2 - r_0^2} \approx 1.9(R+S) \tag{4.2}$$

Similarly, the resolution of MFM in the force gradient mode in which $r_1^4 = 10r_0^4$ can be estimated to be:

$$OA = \sqrt{r_1^2 - r_0^2} \approx 1.3(R+S) \tag{4.3}$$

The resolution in the force gradient mode is usually better than that in the force mode for magnetic force microscopy under the same conditions. For further estimation of the resolution, the detailed operation of MFM has to be considered. In a real measurement, the MFM is not only sensitive to the magnetic force. Instead it is sensitive to all the forces acting on the tip. These forces, however, do include not only magnetic forces but also atomic forces, e.g., van der

Waals forces. In order to minimize the contribution of the atomic forces, which decreases with the separation distance more rapidly, the tip is placed at least 10 nm above the sample surface, i.e., $S \geq 10$ nm. Assuming that identical tips are used in MFM and Sp-STM, i.e., the radius of the hemisphere at the tip end is also 5 nm. In reality, the radius of the effective magnetic tip is usually larger than this as the magnetic film thickness used for coating the MFM tip is around 15 to 200 nm [65]. In the situation of a 5 nm tip, the lateral resolution of MFM can be estimated to be 30 nm in the force mode and 20 nm in force gradient mode. They are more than one order of magnitude larger than the resolution of Sp-STM with the same tip.

Additionally, under favorable circumstances, the tip has a single adatom at its end. In this case, Sp-STM can achieve atomic resolution [66] as most of the tunneling current is focused on this adatom. For MFM, this would not change the resolution as the whole magnetic volume of the tip has to be taken into account.

4.1.4 Summary

In this section, two evidences are presented to prove the magnetic origin of the contrast obtained by Sp-STM. First, by applying an external magnetic field, domain wall movement is observed while no movement of the morphology signal is found. This unambiguously reveals the magnetic origin of the signal. The similarity between the domain images obtained by Sp-STM and MFM gives the second evidence for the magnetic origin of the obtained contrast by Sp-STM. Further, in a very simple model, we compared the resolution of the Sp-STM and MFM. Under the similar tip conditions, the resolution of Sp-STM is estimated to be more than one order of magnitude better than that of MFM.

4.2 Ultra narrow surface domain walls of Co(0001)

4.2.1 Surface closure domain of Co(0001)

Hcp cobalt displays an uniaxial magneto-crystalline anisotropy with an easy direction along the c-axis, i.e., perpendicular to the selected (0001) surface. Due to the minimization of the stray field energy and the net magnetic flux existing at the surface, the single domain state is unstable and splits up into a Landau-Lifshitz like closure domain pattern. Since the magnetic anisotropy energy and the stray field energy are of the same order of magnitude, no perfect and simple closure domain structure occurs on the (0001) surface. Instead, a complex dendritic structure is observed, where the magnetization of most areas of the surface of the closure domain is strongly rotated away from the surface normal as observed, e.g., with scanning electron microscopy with polarization analysis (SEMPA) [63]. The exchange length $\sqrt{A/K_d}$ with A the exchange energy constant and $K_d = 2\pi M_s^2$ the stray field energy constant, is ≈ 5 nm for bulk cobalt. Additionally, it was pointed out by Hubert and Rave [67] that sharp wall-like transitions can be formed in the closure domain pattern, especially when higher order in-plane and out-of-plane anisotropy terms are present as in the case for Co(0001). However, with the resolution of the established standard magnetic imaging techniques, e.g., ≈ 20 nm for SEMPA and ≈ 30 nm for MFM, the fine structure of the closure domains of Co(0001), especially the domain walls cannot be fully resolved. For this kind of study, a magnetic imaging technique with higher resolution, e.g., Sp-STM is highly required.

4.2.2 Experiments

Sp-STM is used to study this complex structure with high resolution. To minimize the influence of the stray field of the tip on the magnetic structures under investigation as well as to obtain images with high resolution, especially sharp tips are produced by slow electrochemical etching of a magnetic wire with 130 μm diameter. For the details of the tip etching, please see Sec. 3.3.2. After sample and tip preparation, the Co(0001) is inserted into the Sp-STM stage to perform magnetic imaging and topography measurement at room temperature.

The topographic STM scans showed terraces of the width of ≈500 nm separated by atomic steps, see Fig. 4.8a. As Co shows a well known hcp-fcc phase transition at $\approx$ 690 K, the annealing temperature was limited. Therefore, the surface remained with a low concentration of small defects - either sputter defects like adatom, vacancy islands or local fcc or misoriented hcp areas, as has been observed also by other authors [68]. Fig. 4.8b shows the perpendicular magnetization component of the sample in the same area obtained by Sp-STM. The displayed area was selected from large scans of closure domain pattern close to one end of the branches. The domain wall in the magnetic images (see Fig. 4.8b) is not correlated with the topography or pinned at the topographic defect (compare Fig. 4.8a). By retracting the tip, the background

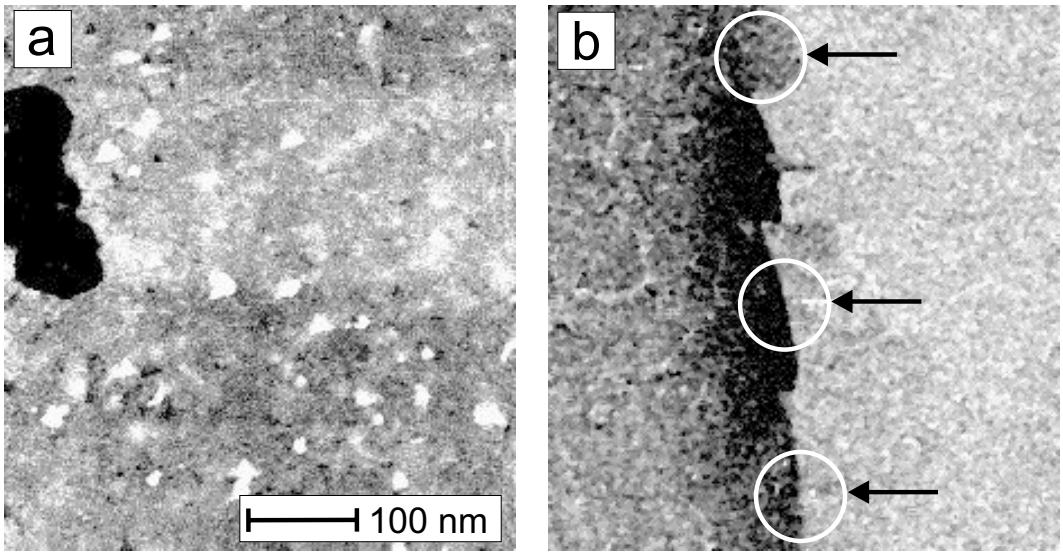

Figure 4.8: Details of the STM images of topography (a) and the perpendicular component of the magnetic domain structure near the domain wall position. Note that three different widths of domain walls are found in this image.

signal caused by the induction of the coil (see Sec. 3.2.2) is obtained to be almost in the middle of the signals shown in the magnetic image, Fig. 4.8b. This refers that the perpendicular components of the gray domain and that domain in darker color are of opposite sign. By applying a magnetic field (in vertical direction) and observing the wall movement with respect to the topography, it was crosschecked that the observed structure indeed is magnetic domain (see Sec. 4.1.1). When having a closer look, the wall shows some interesting fine structures. It splits up into several segments with different wall widths. In section α a gradual transition between the two domains is observed, while in section β it is considerably sharper. In section γ the transition seems to be abrupt on the scale of the image. The different, rather straight sections are separated by kinks in the domain wall.

To quantify the differences in the wall width, we recorded line scans across the different sections of the wall. Fig. 4.9 displays the measured wall profiles obtained by averaging 25 line scans across each section of the wall. The error bars represent the statistical error from averaging. Note that the line scans, especially across the narrow sections of the wall, have been taken with higher magnification than Fig. 4.8 to avoid lateral sampling noise. For a better exhibition of their features, they are shown in different x-axis scales. Additionally, the scanning speed was set such that the neighboring data points are separated by more than two times the integration time of the lock-in amplifier to ensure that the data points are statistically independent and the wall profile is recorded correctly (the data acquiring time for 1 pixel is 8 ms and the integration time of the lock-in signal is set to 3 ms). From the figure it is obvious that the wall width of the

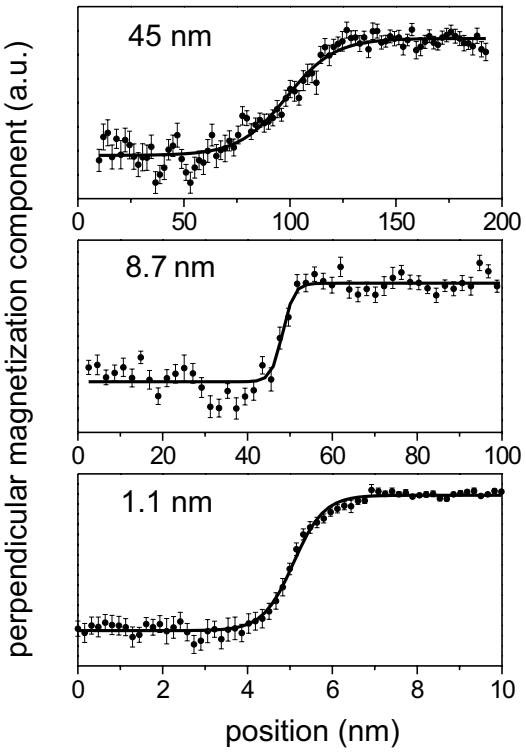

Figure 4.9: Averaged line profiles across different sections of the domain wall as indicated in Fig. 4.8b including the statistical errors and fits with the standard wall profile (solid lines). The fitted wall widths are given in the figure. Note that the different scales of the x-axis of individual line profiles.

different sections varies by more than one order of magnitude (note the different scales on the x-axes). To estimate the wall width $w = 2\delta$, we fit the profiles $m_z(x)$ with the standard wall profile for uniaxial system[1] :

$$m_z(x) = \tanh\left(\frac{x}{\delta}\right) \tag{4.4}$$

resulting in the following width for different sections: $\alpha : w = 45 \pm 8$ nm, $\beta : w = 8.7 \pm 3.2$ nm, $\gamma : w = 1.1 \pm 0.3$ nm. The wall width of section α is broader than the width of a bulk 180° domain wall, which is ≈ 11 nm for bulk cobalt. The broadening of domain walls at the surface is well known and has also been seen for this particular surface of Co [63]. However, sections β and especially γ are much narrower than the bulk 180° domain wall. At first glance, section γ

[1]There are four different kinds of definition for the width of domain wall [1]. Here, we take one of the classic domain wall width which is defined as the changed magnetization component divided by its slope in the center of the wall.

seems to be unphysically narrow. To check for the instrumental reasons for observation of such narrow walls, we made the following considerations.

One possible mechanism that might lead to the seemingly ultra-narrow walls could be a non-linear response of the instrument to the perpendicular component of the magnetization, e.g., a response like a step function. The TMR effect, however, is a linear effect with the projection of the magnetization of the sample onto that of the tip as has been discussed in Chapter 2. Hence, the observed signal should be proportional to the perpendicular component of the sample magnetization. Additionally, a step shaped response function should narrow all the domain walls, while we observe walls of largely different width with continuous transitions in the wall profiles even in a single scan of the surface together with the ultra-narrow domain walls (see Fig. 4.8b and Fig. 4.9 profile of section α). This rules out that we have a transfer function that artificially sharpens the walls.

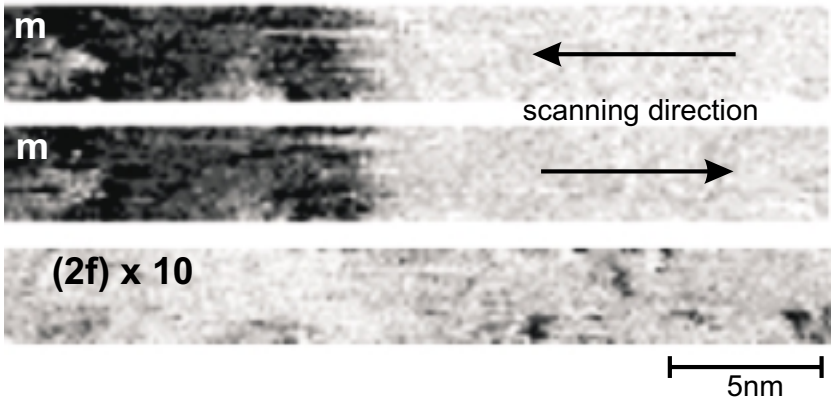

Figure 4.10: Detailed Sp-STM images of perpendicular component of the local magnetization m scanning from the right to the left (top) from the left to the right (middle) and the magnetic susceptibility χ (bottom) taken simultaneously at the same area which is across a narrow wall section of the Co(0001). Note that the magnetic susceptibility is shown in 10 times higher sensitivity.

As the tip used for Sp-STM is magnetic, it has a certain stray field. Therefore, the magnetic tip might pick up the domain wall and drag it along during scanning until it snaps off. In that case a sharp transition would be observed at the point of snapping off. This is a typical problem for most of the scanning imaging technique, like MFM. To test this mechanism, we recorded the wall while scanning from the right to the left and in the opposite direction (see Fig. 4.10). If the wall was dragged along and snaps off at a certain position, it would be dragged along the opposite direction as the scanning direction is opposite. Hence, an opposite displacement of the wall for scanning in the two opposite directions should be seen. The domain wall, however, appears at exactly the same position for both scanning directions (see Fig. 4.10), ruling out any

significant dragging. Note that a weak cross talk of the topography to the magnetic image is present at defects position in this scanning scale. No shift of the relative position between the cross talk and the domain wall can be found in both directions. As drift is a typical problem for high resolution imaging techniques like STM, especially in small scanning scale, a shift of the morphology signal is usually found between the images scanned in opposite directions. For this reason, the scans of the domain wall which related to topographic defects were selected to eliminate drift.

Additionally, we also studied the influence of the magnetic stray field of the tip on the wall by measuring the magnetic susceptibility. When scanning with dull tips, the stray field of the tip can move (and widen) the domain walls of Co(0001). This can be quantified by measuring the second harmonic signal of the switching frequency in the tunneling current. The second harmonic is directly related to the magnetic susceptibility. In the case that the wall is influenced by the stray field of the tip, a maximum in the susceptibility is observed in the center of the wall and a wall contrast is obtained. (The detailed discussion of the magnetic susceptibility measurement will be presented in the next section.) In the bottom part of Fig. 4.10, the susceptibility signal of the same area is shown. With a close examination of the image, however, no significant contrast is found at the domain wall position. Note that the susceptibility signal is shown in 10 times higher sensitivity compared to the magnetization signal. Hence, the influence of the stray field of the magnetic tip on the domain wall can be excluded. The very good resolution of the tip (better than 1 nm; see the bottom line profile of Fig. 4.9) also indicates that the tip is brilliantly sharp. Probably, in this case, the stray field of the tip is fully minimized so that it is not strong enough to cause an observable influence on the sample magnetization which is considerably magnetically hard.

Hence, the observed ultra-narrow domain walls are real. This, at first sight, might contradict the common knowledge about domain walls. The wall in segment γ is one order of magnitude narrower than a 180° domain wall in bulk Co. This is very surprising, since the walls observed on the surface originate from domains that penetrate the bulk of the crystal. Also the geometrical constraints, that in some cases lead to a narrow wall [69], can be ruled out as the observed domain walls are found to be neither related to the step edges nor pinned at the surface defects by a careful comparison of the morphology and magnetic structure of the same area which were obtained simultaneously.

4.2.3 Surface closure domain model

To understand the origin of the narrow walls, we focus on the complex nature of the closure domain pattern of Co(0001). Hcp Co has an uniaxial anisotropy with the easy axis along its c-axis, i.e., perpendicular to the selected sample surface. One easy axis means two easy directions, either positively or negatively aligned along the easy axis. In order to minimize the magnetic

anisotropy energy, the magnetization of the sample prefers to stay either along one of these two directions (single domain state) or parts of the sample magnetization stay in one easy direction while the remains occupy the other one (multi-domain state). The stability of the different states depends on the total energy also including exchange and stray filed energy.

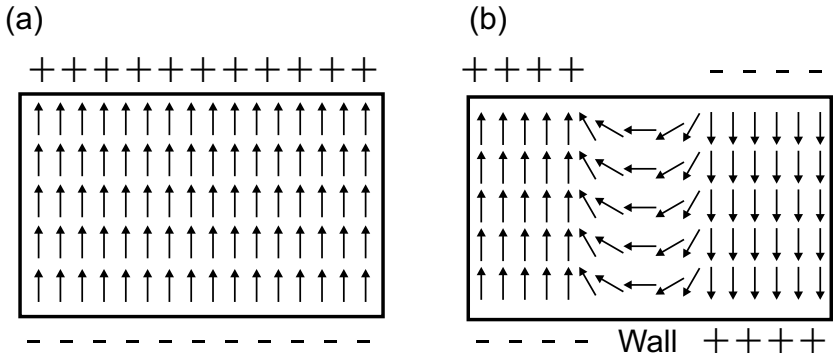

Figure 4.11: Comparison of single domain state (a) and multi-domain state (b) of a sample which has perpendicular easy axis. The arrows indicate the magnetization orientation inside the sample. Note that in case (a) magnetic charges are formed at both upper and lower surfaces while in case (b) the magnetic charges are reduced, however, a domain wall is formed between the two opposite domains.

For a finite sample, the single domain state will cause magnetic charges on the sample surfaces(see Fig. 4.11a). This induces an additional energy term – the stray field energy. The stray field energy depends on the saturated magnetization M_s, the shape of the sample and its volume, i.e.,

$$E_d = 2\pi M_s^2 \cdot N \cdot V = K_d \cdot N \cdot V \tag{4.5}$$

Here, V is the volume of the sample and N $(0 \leq N \leq 1)$ is the shape factor. $K_d = 2\pi M_s^2$ is so called shape anisotropy constant or stray field energy constant, i.e., the difference of the magnetostatic energy density for an infinitely thin film being magnetized either parallel or perpendicular to its surface. The multi domain state has transitional boundaries between different domains (see Fig. 4.11b), the domain walls. At the domain wall positions, the magnetization rotates from the magnetization direction of one domain to the magnetization direction of the neighboring domain. Therefore, the magnetization direction in the wall is neither fixed nor aligned along one of the easy axis. This causes two additional energy contributions, i.e., the exchange energy and magnetic anisotropy energy. The sum of both the exchange energy and the magnetic anisotropy energy of the domain wall is called domain wall energy. The domain wall energy per unit area is called domain wall energy density γ_w. The competition of the stray field energy and domain wall energy determines whether a single domain state or a multi domain state is observed. The stray field energy increases with the volume of the sample and the domain wall

energy increases with the area of the domain wall. For a sample of spherical shape, the stray field energy increases with the cube of its diameter and the domain wall energy increases with the square of its diameter. Therefore, the domain wall energy becomes lower than the stray field energy when the diameter of the sphere is big enough. Hence, a small sphere will be in a single domain state and above a critical diameter a transition to a multi-domain state will be observed. This critical diameter of the sphere was estimated by Kittel [70] and Néel [71] to be $\approx 9\gamma_w/K_d$, which is typically in the several nanometer range. Hence, from the energetic point of view, for a macroscopic sample like the bulk cobalt used in our measurement, the single domain state is not stable. The sample is in a multi-domain state.

The above mentioned states are very simple magnetic domain configurations. Usually, the domain structure is much more complicated than this. It depends on the minimization of the total energy which usually needs complicated micromagnetic calculation. For a thick sample like bulk cobalt, the magnetization at the sample surface is tilted towards the sample surface to minimize the stray field energy further and by this lower the total energy. Therefore, a surface closure domain pattern is formed (see Fig. 4.12). The details of the closure domain pattern crucially depend on the material parameters. One of them, the reduced anisotropy constant, $Q = K_u/K_d$ is of great importance. Here, K_u is the first order crystalline anisotropy constant and $K_d = 2\pi M_s^2$ is the shape anisotropy constant. With $K_u = 5 \times 10^5$ J/m^3 and $M_s = 1440$ emu for bulk cobalt [72], one obtains $Q \approx 0.4$. Hubert et al. [1] have shown that for a sample with $Q = 0.4$, the tilted closure domain pattern shown in Fig. 4.12 is the best choice for the energy minimization as it is both simple and efficient.

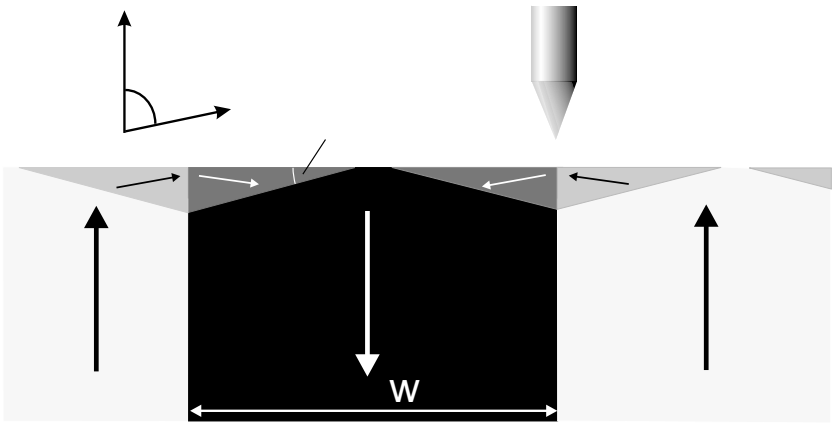

Figure 4.12: A simple sketch for the tilted closure domain model. The tilted closure domain model is the best choice for small anisotropy materials (including cobalt with $Q = 0.4$) as it is both simple and efficient [1].

The detailed analysis of the closure domain pattern can be found in the book of Hubert and Schäfer [1]. Here, we will briefly discuss how the canting angle θ of the magnetization in

the surface closure domain (the domain with canting magnetization) shown in Fig. 4.12 can be calculated by minimizing the total energy. At the closure domain region, the magnetization is tilted closer to the sample surface so as to minimize the stray field energy. However, when the magnetization is tilted to the sample surface, it is also out of the easy axis. This increases the magnetic anisotropy energy. The equilibrium tilting angle of the magnetization at the closure domain depends on the balance of the stray field energy and the anisotropy energy. The stray field energy E_d (taken per unit area of one sample surface) was calculated by Kittel [70]:

$$E_d = \frac{1}{2} K_d S_c W \cos^2\theta \quad with \quad S_c = \frac{1}{2\pi} 1.705... \tag{4.6}$$

From the model shown in Fig. 4.12 as well as the domain images shown in previous section, one finds the area of the bulk domains (fully perpendicular domain) reaching the surface is small in comparison with the area of the tilted surface closure domains. The surface closure domains dominate the images. Therefore, the width of each single closure domain at the sample surface can be considered as $W/2$ in first order approximation. Hence, the anisotropy energy E_K (taken per unit area of one sample surface) can be estimated to be:

$$E_k = \frac{1}{4} K_u W \tan\beta \sin^2\theta \tag{4.7}$$

To calculate the canting angle, the angle β needs to be determined. This can be derived from the condition of zero charge on the internal closure domain boundaries, i.e., the magnetization component perpendicular to the wall surface should be continuous across the domain wall. As shown in Fig. 4.12, the magnetization of the fully perpendicular bulk domains has an angle of $\frac{\pi}{2} - \beta$ with the internal closure domain wall surface. And the angle between the internal closure domain wall surface and the magnetization of the closure domain is $\frac{\pi}{2} - \theta + \beta$. This turns into the following condition which needs to be fulfilled:

$$\sin(\frac{\pi}{2} - \beta) = \sin(\frac{\pi}{2} - \theta + \beta) \tag{4.8}$$

With this, the reduced total energy density (the sum of the stray field energy density and the anisotropy energy density) in units of $K_u W$ becomes:

$$e = (S_c/Q)\cos^2\theta + \frac{1}{4}(1 - \cos\theta)\sin\theta \tag{4.9}$$

For bulk cobalt, the stray field anisotropy coefficient K_d is 2.5 times larger than the first order anisotropy constant, i.e., K_u. Therefore, a large angle of tilting should be expected. In Fig. 4.13, the total energy as a function of the tilting angle is shown. It indicates a energy minimum at $\theta \approx 80°$. This leads to the model that the magnetization in the closure domains at the sample surface is canted either 10° up or 10° down. That means that the wall between two surface closure domains has only a small rotation angle of $\approx 20°$.

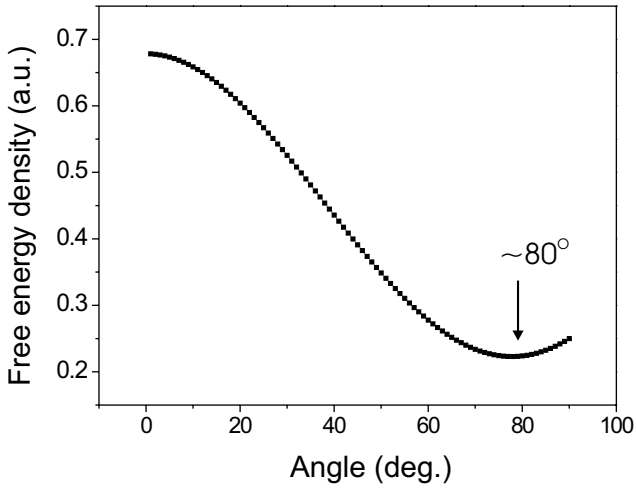

Figure 4.13: The total energy as a function of the tilted angle of the closure domain for Co(0001). It indicates an energy minimum at $\approx 80°$.

The canting angle of the surface closure domains can be estimated experimentally, too. If the full contrast can be obtained, we can compare the contrast across the narrow domain walls with the full contrast between the perpendicular bulk domains. The ratio gives the projection of the angle as the TMR effect is a linear response of the magnetization component projected to the tip magnetization. After carefully reading the surface closure domain model shown in Fig. 4.12, one immediately figures out that there are some areas where the fully perpendicular bulk domains reach the surface. This has been found experimentally with SEMPA as well [63]. Hence, it is possible to obtain the full contrast between the fully perpendicular up/down domains by large area scan. Indeed, we find this kind of signal. Fig. 4.14 shows a large area scan of the morphology (a) and magnetic structure (b) on Co(0001) surface by Sp-STM. A typical dendritic structure domain pattern is shown in Fig. 4.14b. Most of the areas are in gray color which means that the surface closure domains are dominant as predicted by Hubert (see Fig. 4.12). Additionally, the image shows a black contrast at the bottom part and a white one on the top. They are the fully perpendicular bulk domains at the surface. The magnetization in the black area points into the sample surface while in the white region the magnetization point out of the sample surface, respectively.

A line scan between these two bulk domains (see the inserted line in Fig. 4.14b), yields 8 ± 1 V as the full contrast of the magneto-tunneling signal. The average signal is -3.7 ± 0.1 V (see Fig. 4.15a) in agreement with the background signal obtained by retracting the tip. When zooming into one end of the dendritic structure, the ultra narrow domain wall is found (see the

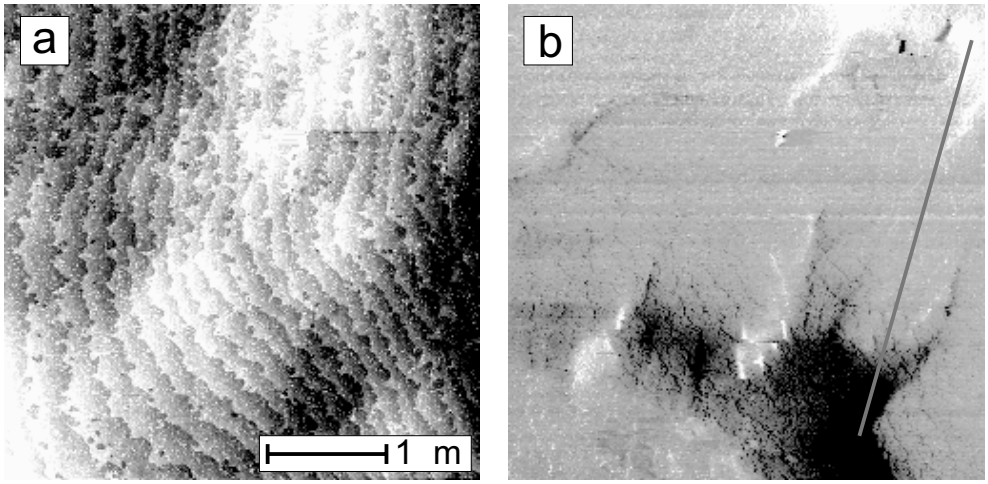

Figure 4.14: Large STM images of topography (a) and the perpendicular component of the magnetic domain structure (b) of the same area of Co(0001). The black/white domains are the bulk domains which reach the sample surface. The inserted line is used to estimate the full contrast.

line profile across the narrow wall shown in Fig. 4.15b). The magneto-tunneling signal difference across the narrow wall is obtained to be 1.4 ± 0.1 V, i.e., $\approx 18\%$ of the full contrast and it is in the middle between the maximum and minimum values of the full contrast. With these values, the canting angle of the surface closure domain on Co(0001) surface can be estimated. It turns out to be $10.1 \pm 1.5^\circ$. This is in good agreement with the theoretical prediction, i.e., $\approx 10^\circ$ mentioned above.

Hence, the domain wall across the two surface closure domains only has $\approx 20^\circ$ rotation in perpendicular direction. This small magnetization change probably only needs smaller space for magnetization rotation, i.e., leads to a much narrower domain wall than the 180° domain wall of bulk cobalt. With a rule of thumb argument, the wall width can be simply estimated in a very crude calculation. A 180° domain wall has a width of ≈ 11 nm. A 20° domain wall width could be only a fraction of 20/180 of the 180° domain wall. The result turns out to be 1.2 nm which is already in good agreement with our experimental data.

We can calculate the domain wall width in a more accurate way. For this purpose, we carried out the standard procedure for domain wall calculation which minimizes the sum of the exchange energy and anisotropy energy inside the domain wall. In one dimensional model, the exchange energy density of the unit wall area can be written as:

$$e_{ex} = A \int (dm_z/dx)^2 dx \tag{4.10}$$

with A the exchange constant. The anisotropy energy density of the unit wall area can be

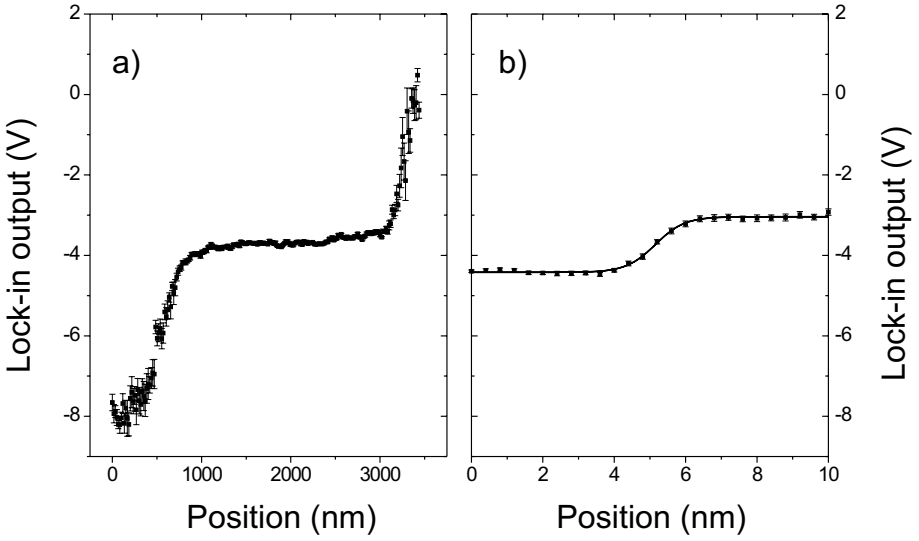

Figure 4.15: (a) a line scan across two bulk domains penetrating out of the sample surface (see the inserted line of Fig. 4.14) and (b) a detail line scan across the the ultra narrow domain wall which was obtained by zooming one end of the dendritic domain shown in Fig. 4.14. The error bar displays the statistic error of 25 line scans.

written as:

$$e_{an} = K_u \int \sin^2(\arccos m_z) dx \tag{4.11}$$

with K_u the first order magnetic anisotropy constant. As mentioned above, the surface domain wall has the rotation of magnetization between $+10^\circ$ and -10°. With the standard domain wall profile of uniaxial system, the domain wall profile as a function of the position can be written as:

$$m_z = \sin\theta \tanh\left(\frac{x}{\delta}\right) \tag{4.12}$$

with $\theta = 10^\circ$. Taking the material parameter of bulk cobalt, i.e., the exchange constant $A = 1.5 \times 10^{-11}$J/m and the first order magnetic anisotropy constant $K_u = 5.0 \times 10^5$ J/m^3 [72], the wall energy, i.e., the sum of the exchange energy and anisotropy energy inside the domain wall can be calculated. Fig. 4.16 shows the calculated domain wall energy as a function of the half domain wall width δ. It indicates a energy minimum at $\delta = 7.5$ Å which is given by the balance of the exchange energy and anisotropy energy inside the wall. Therefore, the wall width is obtained to be $w = 2\delta = 1.5$ nm in good agreement with our experimental observation of the wall width in the section γ. Hence, our experimental findings can be explained by micromagnetic calculations. For simplicity, the magneto-static energy is neglected in this calculation. However,

the surface charge density is small due to the shallow angle of the magnetization of the closure domain. Additionally, surface anisotropy at the Co-vacuum interface might also reduce the wall width.

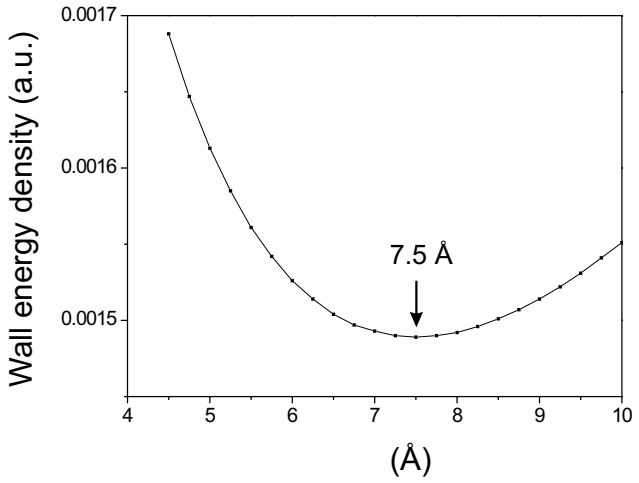

Figure 4.16: The domain wall energy density as a function of δ for a wall which rotates between the $+10°$ and $-10°$. It indicates an energy minimum for a wall width of $w = 2\delta = 1.5$ nm.

So far, only the domain wall which has perpendicular magnetization rotation has been considered. Hcp cobalt, however, has a sixfold in-plane magneto-crystalline anisotropy, i.e., the in-plane component of the magnetization can align along six possible directions. This meas that in addition to a 20° out-of-plane magnetization rotation, an in-plane rotation of magnetization of 60°, 120° or 180° can take place. Since the total angle of rotation becomes bigger than that in the previous case, the corresponding wall widths are considerably wider. Unfortunately, an analytical calculation for the profile of these kind of two dimensional walls is not possible following the standard methods. Assuming that the in-plane anisotropy constant is in the same order of the magnitude as the perpendicular anisotropy constant, the lower limit for the wall width can be estimated to ≈ 5 nm for a 60° and ≈ 10 nm for a 120° in-plane magnetization rotation involved domain wall.

With our experimental set-up only the sensitivity of the perpendicular component is achieved. That means within the simple domain model, walls that display a rotation only in-plane are invisible and all domains that have the same out-of-plane magnetization have identical contrast. At the ends of a fractal branch of the closure domain structure, several small domains touch as can be seen from SEMPA images. Hence, different types of domain walls are present at that point. This explains our Sp-STM observations. The different sections of the visible domain wall correspond to domain walls with different in-plane rotation, possibly 0° for section γ, 60° for

section β and 120° for section α, while the domain walls where only the in-plane angle changes are nearly invisible within the noise level. However, the points where the in-plane domain walls meet the clearly visible out-of-plane wall, the out-of-plane wall displays kinks. A detailed image of low noise level of such a kink is shown in Fig. 4.17, displaying a third, nearly invisible triangular domain of very weak contrast in the upper part, indicated by an arrow. The lower part of the domain wall belongs to the ultra-narrow section γ of Fig. 4.8. In the uppermost part, the wall widens and the wall has the same width of the section β. The widening of the wall could possibly correspond to a wall with 60° in-plane rotation. The very faint domain contrast on the top parts may come from a weak in-plane contrast. If the tip is orientated in a direction which is slightly out of the perpendicular axis, a very weak sensitivity for the in-plane signal is obtained. Note the contrast between the triangular domain and the right side domain is less than 10% of the contrast between the two main domains. This indicates the very good alignment of the tip, i.e., nearly fully perpendicular to the sample surface (keeping in mind that the perpendicular component has only 20° rotation while the in-plane component has 60° rotation of magnetization). These findings support our assumption, that the angle of rotation in the sample plane across the different sections of the domain wall is different leading to different wall widths.

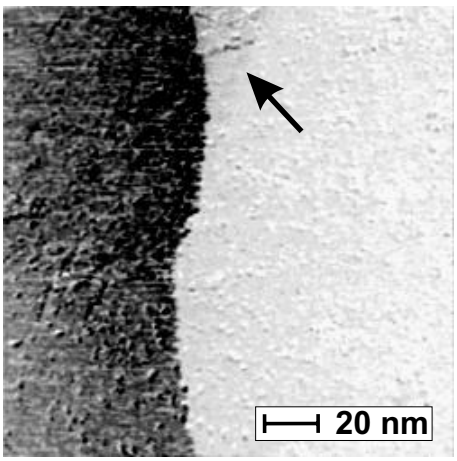

Figure 4.17: STM images of the perpendicular component of the magnetic domain structure of the same area of Co(0001). Note a nearly invisible triangular third domain at the top of image, indicated by an arrow.

The observation of sharp domain walls on the surface of Co(0001) also gives some experimental evidence for the theoretical predictions of Hubert and Rave [67] that sharp wall-like transitions can be formed at the surface of a closure domain pattern, especially when higher order in-plane and out-of-plane anisotropy terms are present as in the case for Co(0001).

The observation of the ultra narrow sections in the domain walls of the closure domain pattern

of Co(0001) is not only a very surprising micromagnetic result but also yields an estimation for the lateral resolution of our instrument of about 1 nm. This high a resolution opens up a new view to experimental micromagnetism and illustrate the potential of Sp-STM.

4.2.4 Summary

With the high resolution of Sp-STM, the fine structure of surface closure domain of Co(0001) is fully resolved. Experimentally, we found three different sections of domain wall separated by kinks. The wall widths were fitted with standard domain wall profile for uniaxial system to be: $\alpha : w = 45 \pm 8$ nm, $\beta : w = 8.7 \pm 3.2$ nm, $\gamma : w = 1.1 \pm 0.3$ nm. By comparing the contrast obtained across the narrow wall with the full contrast achieved in large area scan, we confirmed the surface closure domain model predicted by Hubert [1], i.e., the surface closure domain is aligned along either 10° up or 10° down from the surface. This small magnetization rotation angle of 20° explains the width of the ultra-narrow domain wall in section γ when no in-plane magnetization rotation is involved. Due to the natural sixfold in-plane anisotropy, the domain wall width becomes wider when the in-plane magnetization rotation is involved. Consequently, this explains the different wall widths found in our experiments. The finding of the ultra narrow section of the domain wall also gives an estimation of the resolution of Sp-STM of better than 1 nm.

4.3 Local magnetic susceptibility

In contrast to previous sections where we minimized the influence of the tip magnetization on the sample by using a sharp tip, we now want to have a measurable influence. Freshly prepared tips that are also sharp on the mesoscopic scale produce a rather localized stray field. As a consequence, the domain walls of hard magnetic materials are not influenced and can be resolved with high resolution as shown in previous sections.

When a tip is used that is dull from the beginning by optical inspection or is dull due to several severe tip crashes, domain walls are smeared out as in Fig. 4.18b. This is due to a periodic domain wall movement induced by the alternating field of the tip. The walls rapidly vibrate with the magnetization frequency f. In such a way the resolution is limited to ≈ 1000 nm (see Fig. 4.18b), while the topographic resolution is still good (see Fig. 4.18a). This magnetic interaction between tip and sample can be used to locally measure the magnetic susceptibility of a sample.

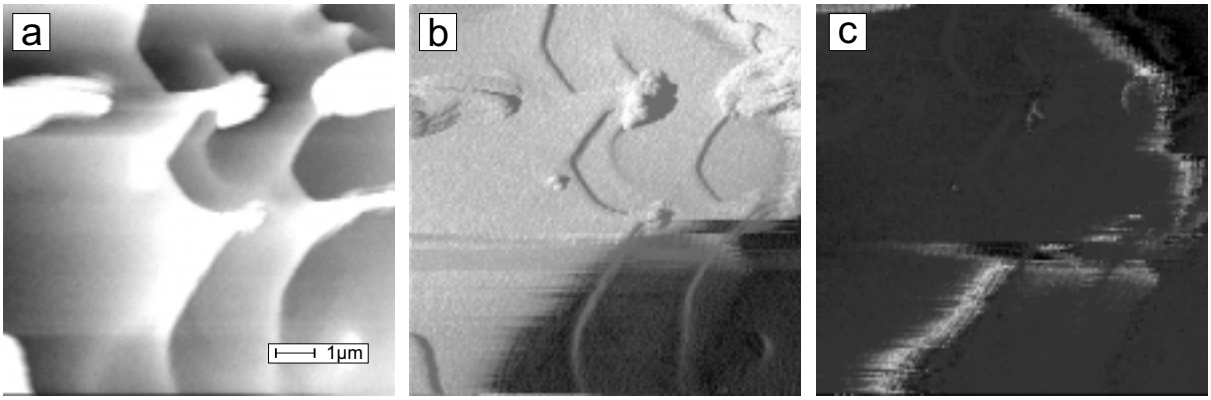

Figure 4.18: Topography (a), magnetic structure (b) and local susceptibility (c) measurement on Co(0001) surface. Note the tip has been severely crashed into the sample surface several times before the image was obtained, therefore a dull tip with much larger stray field is expected.

As the magnetic tip is very soft, its magnetization is switched by the current flowing through the coil, and its magnetization shows a square like wave as a function of time as shown in Fig. 4.19(a). When the stray field of the tip is small and not high enough to switch the sample magnetization, the local magnetization of the sample is a constant with perpendicular component $m_z = \sin\theta$ with θ the angle between the sample magnetization and the sample surface normal. When the stray field of the tip is not negligible, it influences the local sample magnetization. This causes a modulation of the sample magnetization with magnitude of $\delta\theta$ at the frequency of the tip magnetization change. Since the sample magnetization cannot follow instantaneously the local stray field of the tip, a phase difference between the magnetization of the tip and the sample exists. A typical perpendicular component of the local sample magnetization as a

function of the time is shown in Fig. 4.19(b).

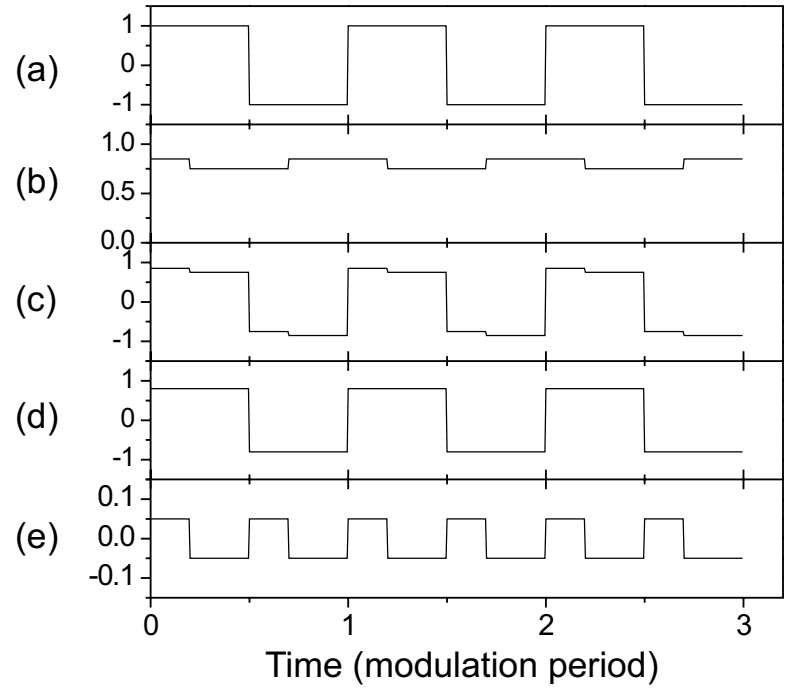

Figure 4.19: (a) Magnetization of the tip (in the unit of the saturation magnetization of the tip) as a function of the time. (b) The perpendicular component of the local magnetization of the sample surface (in the unit of the saturation magnetization of the sample) as a function of the time. Note that the small modulation is caused by the flipping of the tip magnetization, however, with a phase shift. (c) The magneto-tunneling current (in the unit of IP_tP_s, I is the total tunneling current, P_t and P_s are spin polarization of the tip and sample, respectively) as a function of time which is obtained as the product of (a) and (b) following Slonczewski's formula [34]. (d) and (e) are the $1f$ and $2f$ components of the magneto tunneling current deconvoluted from (c).

With both the time dependent tip and sample magnetization, we can calculate the response of the magneto tunneling current. As addressed by Slonczewski [34], the magneto-tunneling current is proportional to the projection of the magnetization between the tip and sample surface. Therefore, we can write down the magneto tunneling current across the barrier which is the product of (a) and (b) shown in Fig. 4.19 in the unit of $I_0P_tP_s$, I_0 is the total tunneling current, P_t and P_s are spin polarization of the tip and sample, respectively. Fig. 4.19(c) presents the calculated magneto tunneling current. Besides the square like wave, it shows an additional feature which corresponds to the change of the sample magnetization induced by the stray field of the tip, i.e., the local magnetic susceptibility. The magneto-tunneling current can be split into

two square like waves with two different frequencies. Fig. 4.19(d) and (f) presents the result of the separation. The magneto-tunneling current has two components, (d) has the same frequency as the modulation field, (e) has 2 times of the frequency of the modulation field. Hence, higher harmonics are produced in the tunneling current due to the nonlinearity of the magnetization process. These contribution can be detected with a second lock-in amplifier simultaneously with the magnetic signal and morphology signal (Fig. 4.18). This mechanism may be used to obtain domain wall contrast as shown in Fig. 4.18c ($2f$-signal). From the observed width of the susceptibility signal around the wall and the switching frequency f, a local domain wall speed of $\approx$10 cm/s can be estimated.

Hence, not only static measurements of the sample magnetization can be carried out with Sp-STM, but the intrinsic stray field of dull tips may be used to carry out dynamic studies while recording magnetization and topography at the same time. This technique in combination with higher switching frequencies might even allow local studies of the switching behavior of individual magnetic nanostructures. Note that in case of sharp tips and magnetically hard samples like bulk cobalt used in the previous section, no measurable susceptibility signal was detected in the domain walls, showing that the magnetostatic interaction in that case can be suppressed efficiently.

4.4 Tip-to-sample distance dependence of the TMR through a vacuum barrier

In Chapter 2, two different models, the phenomenological Jullière model [30] and the Slonczewski model [34] in the free electron approximation, have been reviewed that explained the TMR effect. The Jullière model has been commonly used in many studies [73, 74], sometimes with the extension that the polarization P_i is the polarization of the ferromagnet/barrier interface [46, 47, 75, 76]. MacLaren et al. investigated the validity of both Jullière and Slonczewski's model by comparing both models with first principle calculations of the TMR between iron electrodes separated by a vacuum barrier showing that Slonczewski's model gives a better description [77]. However, an experimental verification for these two models is still missing. Due to the experimental difficulties, to fabricate similar planar junctions with different barrier heights and widths without changing other parameters like the spin polarization of the interfaces, it is nearly impossible to perform a systematic check in this way. Besides, the influence of impurities inside the barrier is not always avoidable in planar junctions [78–80]. It is hard to distinguish whether changes of the TMR are due to the change of the barrier or the influence of impurity assisted tunneling. Spin-polarized tunneling through a vacuum barrier studied by spin-polarized scanning tunneling microscopy (Sp-STM) offers a good opportunity to test these two models as it has the unique property of an impurity free vacuum barrier. In this section, measurements of the TMR through a vacuum barrier as a function of the barrier width is studied. With this we discuss the validity of the two models given by Jullière and Slonczewski.

The experiments are performed on a Co(0001) single crystal bulk sample. The crystal as well as the tip were cleaned in situ with Ar^+ ion sputtering as mentioned in Chapter 3. With Sp-STM, a dendritic like domain structure of the surface closure domains on Co(0001) is observed. In order to reduce the noise caused by the morphology, we zoom into a small area which contains only two domains with a domain wall in between. After that the same scan line across the wall is repeatedly imaged and the contrast across the wall is studied as a function of the gap width. The TMR is obtained as the difference of the lock-in signals across the domain wall normalized by the total tunneling current, i.e., $\Delta I/I$. To reduce the noise, the TMR is measured by averaging the signal over 20 line scans. By changing the tunneling current, the tip-to-sample distance is adjusted according to:

$$I \propto \frac{V}{d} \exp(-A\overline{\phi}^{\frac{1}{2}} d) \tag{4.13}$$

where the constant $A = 1.025\ (\mathrm{eV})^{-1/2}\mathrm{\AA}^{-1}$, $\overline{\phi}$ the average barrier height between the two electrodes, V the bias potential between the sample and the tip, and d the gap distance [81]. The above formula is only valid for small bias voltages. For a more rigorous formula, please see the formula given by J. G. Simmons [82].

Fig. 4.20 presents the result of tunneling current dependence of the TMR effect at 3 dif-

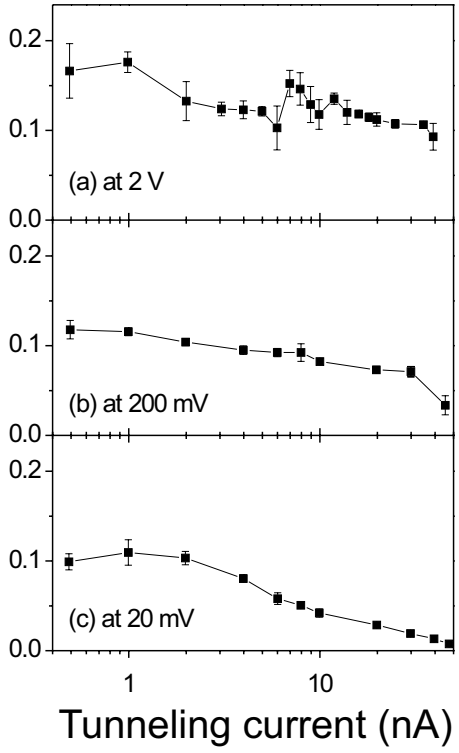

Figure 4.20: Tunneling current dependence of the TMR effect ($\Delta I/I$) through the vacuum barrier at (a) 2 V (b) 200 mV (c) 20 mV. Note, the tip approaches the sample surface when the tunneling current increases and the voltage decreases.

ferent bias voltages. The error bar displays the statistic error of 20 line scans averaging. The dependence of TMR with tunneling current is found to be varied with the applied bias voltage. At 2 V, the TMR shows only a slight decrease when the tunneling current increases. When the bias voltage decreases, the tendency of the decrease becomes stronger. At 200 mV, this decrease becomes clearer. At 20 mV bias voltage, the TMR value decreases much quicker than at 200 mV and 2 V. When the tunneling current is close to 40 nA, the TMR nearly reaches zero. As the bias voltage is fixed during each measurement, the change of the TMR effect with current cannot be attributed to the influence of the voltage. Hence, we have to consider an effect related to the change of the gap distance between the tip and the sample surface as it changes with the tunneling current. The tip approaches the sample surface when the tunneling current increases. The decrease of the TMR could be caused by the tip approaching. The difference of the tendency for the TMR change with tunneling current at different bias voltage could be caused by the different starting points for the tip approaching the sample surface. As shown in Eq. 4.13, at a fixed tunneling current, the tip-to-sample distance is different when different bias voltages are applied. The tip approaches the sample surface when the bias voltage decreased.

Due to the fact that it is not easy to determine the separation of the tip and sample surface by a simple measurement, all the measured TMR values are plotted as a function of the tunneling resistance which is an indirect measure for the tip-sample separation.

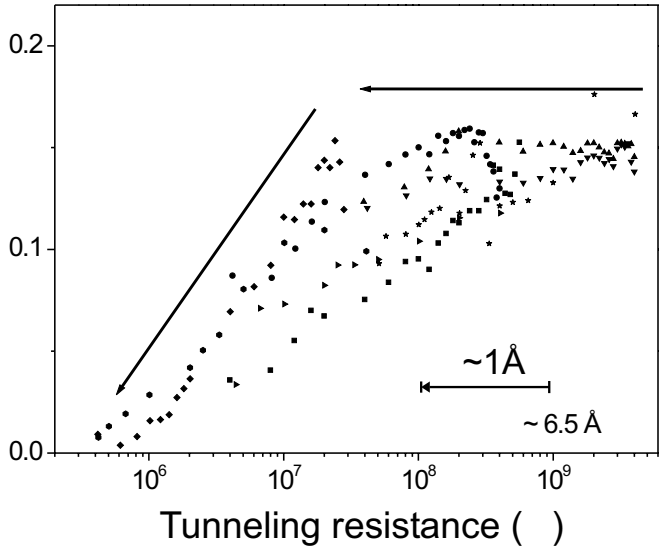

Figure 4.21: The TMR ($\Delta I/I$) as a function of the tunneling resistance. The different symbols indicate different bias voltage measurements. The arrows are guides to the eye.

Fig. 4.21 shows the dependence of the TMR with the tunneling resistance. The different symbols indicate different data sets obtained at different bias voltages. The inserted two arrows indicate the tendencies of the TMR change. Roughly speaking, the tip approaches 1 Å towards the sample surface when the tunneling resistance decreases by one order of magnitude. The TMR is nearly independent on the tunneling resistance at large tip-sample separations (1×10^{-9} Ohm corresponding to about 6.5 Å). At small tip-sample separation, however, the TMR strongly decreases with the tunneling resistance. The scattering of the data may be attributed to bandstructure effects caused by different bias voltages. Also, the tunneling resistance is not exactly an exponential function on the barrier width as shown in Eq. 4.13. Furthermore, the barrier height may change with bias voltage and barrier width so as that the exponential coefficient may change. Nevertheless, the figure still clearly indicates that the TMR effect strongly correlates with the separation between the tip and sample surface.

To study the TMR as a function of the tip-to-sample distance quantitatively, further measurements are performed in a way that the gap width is under better control. Fig. 4.22a shows a typical tunneling current versus the tip-to-sample distance change obtained at 20 mV sample bias. For this measurement, the feed back loop was opened for a short time and the tip was approached or retracted in a controlled way. The tunneling current measured in this way in-

creases nearly exponentially when the tip approaches the sample surface as expected in normal tunneling experiments. Fig. 4.22b presents the TMR as a function of the tip-to-sample distance measured at the same time. It shows that the TMR is nearly constant at large tip-to-sample distance and decreases strongly when the tunneling resistance is smaller than 5 MΩ (20 mV,4 nA). Assuming a contact resistance of $\approx 24\ k\Omega$, the resistance of 5 MΩ corresponds to a tip-to-sample distance of ≈ 4.5 Å [83–85]. As the bias voltage used in this measurement is fixed, no change of the TMR is expected due to bias voltage. Therefore, we have to attribute the TMR change to change of the tip-to-sample distance, either directly or indirectly via changes of other barrier properties induced by it.

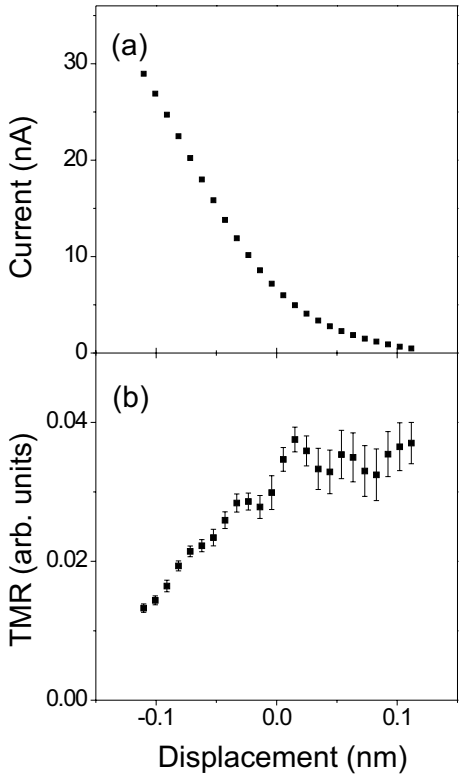

Figure 4.22: (a) Typical tip-to-sample distance of the tunneling current. The sign of the displacement means the tip is closer (−) or further away (+) from the sample. (b) The simultaneously measured the tip-to-sample distance dependent TMR (magnetic contrast). The bias voltage is 20 mV.

To further understand this effect, we come back to theory. In the model given by Jullière, the TMR effect does not depend on the barrier width, i.e., the tip-to-sample distance in our experiments. The TMR only depends on the spin polarization of the ferromagnetic electrodes P_f. In the simple theory where parabolic bands are considered, the spin polarizations are defined

as the asymmetry of the wave vectors for spin-up and spin-down electrons at the Fermi level:

$$P_{1(2)} = \frac{k^{\uparrow}_{1(2)} - k^{\downarrow}_{1(2)}}{k^{\uparrow}_{1(2)} + k^{\downarrow}_{1(2)}} \tag{4.14}$$

As the $k_f^{\uparrow}$ and $k_f^{\downarrow}$ are the wave vectors inside the ferromagnetic electrodes, no significant change should be expected. With the simple model given by Jullière, the observed drop of the TMR with the decrease of the tip-to-sample distance cannot be explained.

In the free electron approximation, Slonczewski calculated the TMR and pointed out that it does not only depend on the two ferromagnetic electrodes but also on the barrier as pointed out in Chapter 2. The effective spin polarization and by this the TMR depends on the barrier height V_b, to be more specific on the imaginary wave vector $i\kappa$ in the barrier (see Eq. 2.16). In the limit of small bias voltage where only the electrons near the Fermi level tunnel, κ is defined by $\hbar\kappa = [2m(V_b - E_F)]^{1/2}$. Hence, through κ, the TMR effect depends on the height of the barrier. When the local barrier height varies with the tip-to-sample distance, the TMR effect also changes. It is well known that the local barrier height in STM measurements decreases when the tip is approached closer than ≈ 4 Å [83–85]. The decrease is due to the fact that electron densities of the tip and the sample start to overlap significantly and the tunneling electrons do not have to overcome the full work function but only a fraction of it. At small bias voltages, the local barrier height can be obtained from the tunneling current as a function of the tip-to-sample distance according to the following formula [85]:

$$\phi(eV) = 0.952 \left(\frac{d\ lnI}{dS} \right)^2 \tag{4.15}$$

where the barrier width S is in Å. Fig. 4.23a presents the local barrier height versus the tip displacement calculated from the data shown in Fig. 4.22a. It is nearly constant at large tip-sample separation and decreases when the tip further approaches the sample surface. The observed change of local barrier height is similar to the tip-to-sample distance dependent TMR effect shown in Fig. 4.22b. This suggests a correlation between the barrier height and the TMR effect.

To quantify the influence of the local barrier height on the TMR effect, we performed calculations in the free electron model proposed by Slonczewski [34]. With the local barrier height measured above, the imaginary wave vector inside barrier for electrons tunneling near the Fermi level is determined. Therefore, applying the formula given in Eq. 2.3 and Eq. 2.16, the TMR effect as a function of the tip displacement is calculated. As one parameter, the exchange energy is chosen to be 1 eV for Co [41]. As there is no direct measurement for the spin polarization of single crystal Co(0001), we calculate the TMR for 3 different spin polarization values. The 3 different spin polarization values are, 33% chosen from early measurement by Meservey and Tedrow [86], 45% chosen from recently reported values by Moodera [53], and 65% selected just

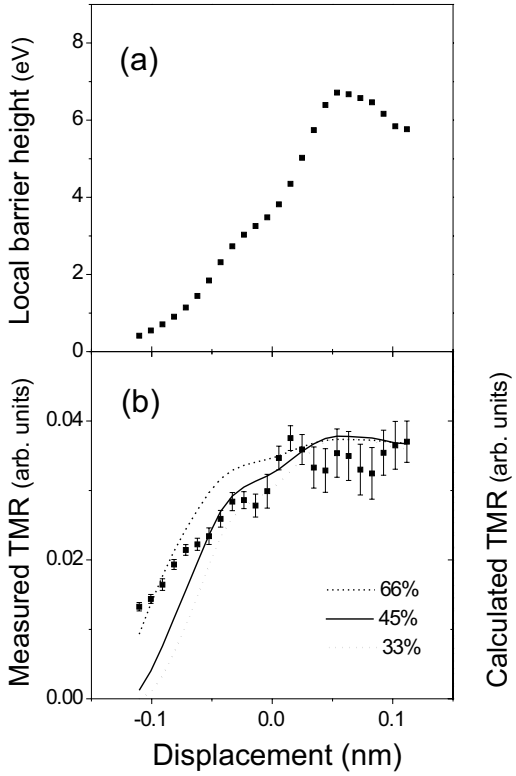

Figure 4.23: (a) The tip-to-sample distance dependent local barrier height calculated with tip-to-sample dependent tunneling current shown in Fig. 4.22a. (b) Comparison between the measured tip-to-sample distance dependent TMR with the calculated TMR using the free electron model proposed by Slonczewski with the local barrier height given in (a) for 3 different spin polarization values. The calculated curves are normalized with the measured TMR at large tip-sample separation.

for comparison reasons. Same spin polarization values are chosen for the magnetic tip as the tip material is dominated by Co ($\approx 92\%$). As the spin polarization values mentioned above are obtained with Al_2O_3 barriers of a barrier height of $\approx$ 2.5 eV [53], Eq. 2.16 and the exchange energy of 1 eV are used to calculated the wave vectors for spin-up and spin-down electrons. With these 3 different sets of calculated wave vectors and the distance dependent local barrier height, the TMR as a function of the tip-to-sample distance for 3 different spin polarization values are calculated. Fig. 4.23b presents the results of the calculated TMR. For comparison, the experimentally measured tip-to-sample distance dependent TMR (filled squares) is inserted in this figure. All curves are normalized to the TMR value at large tip-sample separation. The figure shows that the calculations for all three spin polarization values reproduce very well the drop of the TMR with the tip approaching, even though the spin polarization values are varying

by a factor of 2. To confirm our experimental result, we also take 10% error for the calibration in z-piezo coefficient into account and perform further calculations. This results in a 20% error for the measured local barrier height. However, no significant change is found when this error is taken into account.

Besides the reduction of the TMR due to a reduced barrier height, two other mechanisms might also contribute to the distance dependence. First, when the tip is approached to the sample surface, the tip and sample interact with each other. This may influence the spin polarization and as a consequence of this the TMR. The interaction between an Fe(001) surface and a spin-polarized tip has been investigated by Fang et al. from the first principle theory [87]. Although the calculation is carried out for Fe, similar effects should be expected for Co. With first principle calculation, they found a decrease of the spin polarization when the tip-to-sample distance is below 2.88 Å. Above this separation, the spin polarization is nearly constant. Therefore, this mechanism most likely does not contribute to the TMR change in our measurement as it is observed at larger tip-to-sample distance($\approx$ 4.5 Å). Second, at large tip-sample separations, the s-,p-electrons are expected to dominate tunneling. The d-electrons could also be involved in the tunneling process at smaller barrier width. This change would reduce the spin polarization of the tunneling electrons as the sign of the spin polarization for s-, p-electrons and d-electrons are opposite for Co [49] and may further cause an additional reduction of the TMR effect. This change of the character of the tunneling electrons, however, is expected to happen at small tip and sample separation as d-electrons are much more localized due to their principle quantum number is lower by 1. In the calculation of Fang et al. [87], the magnetic moment of Fe surface atoms remains almost constant when the tip-to-sample distance is above 2.88 Å. This indicates that there is no strong overlap of d-d states above this thickness as it will induce a change of magnetic moment. This most likely excludes d-electron tunneling in our experiment. Besides, the free electron model has already given a good explanation for the drop of the TMR and we can expect that the change of s-, p- and d-electrons tunneling is not an important effect. Hence, we can conclude that the local barrier height change is the dominant mechanism for the TMR drop. This verifies Slonczewski's model which gives a good approximation for the distance dependent TMR effect.

In conclusion, with both the tip-to-sample distance dependent TMR and local barrier height measured by Sp-STM simultaneously, we give an experimental verification of the two theoretical models given by Jullière and Slonczewski. Slonczewski's model is found to be a better description for the TMR in good agreement with the result of theoretical investigation by MacLaren et al. Our experimental findings also give a guidance for the practical measurement of Sp-STM. For the optimal performance, it is necessary to work at large tip-to-sample distance to achieve a high value of magnetic contrast.

4.5 Bias voltage dependence of the TMR through a vacuum barrier

Although the tunneling magneto resistance effect has already stimulated a lot of research, many details of the effect itself are still far beyond complete understanding. For instance, the question why the tunneling magneto resistance decreases as the bias voltage increases, which is found in most planar junctions, still remains unanswered. In most cases, the tunneling barriers were fabricated by deposition of a metal layer (Al or Mg etc.) and subsequent oxidation of this metal layer. This preparation method has led to either unoxidized remains of the metal inside the barrier or oxidization of the ferromagnetic electrode at the interfaces between the barrier and the ferromagnetic electrode. The presence of metal impurities inside the tunneling barrier or oxidized ferromagnetic layers apparently influence the behavior of the magnetic tunneling junction. The influence of impurities is difficult to understand as it is hard to be controlled. Hence, a vacuum barrier is desired for further understanding of the TMR effect as there are no impurities inside such a barrier and one can work with clean surfaces. In this sense, magneto-tunneling through a vacuum barrier is of great importance. Before going into details of the spectroscopy of the TMR through a vacuum barrier, a brief summary of the spectroscopy of the TMR across insulator barriers is given.

4.5.1 Brief summary of the TMR across an insulator barrier

Using Fe-Ge-Co junctions, Julliere [30] observed a change of nearly 14% at 4.2 K in the tunnel conductance at zero bias with the application of a magnetic field. A bias voltage dependence of the TMR is also given in his paper(see Fig. 4.24). The TMR decreases strongly with the bias voltage. At nearly 3 mV, the TMR value decreased to half of the maximum value, i.e., $V_{1/2} =$ 3 mV. Julliere explained this strong decrease of the TMR by spin-flips taking place at metal-barrier interfaces. Many groups have attempted magneto-tunneling between ferromagnetic films prior to 1995. The results, however, either failed to exhibit any spin polarization of the tunnel current or were not able to show large TMR at room temperature. The failure of these attempts might be due to the difficulty of producing a tunneling junctions of good quality. Particularly, forming the insulator barrier by oxidizing a metal layer is difficult. Consequently, they found that the TMR effect seems to decrease rapidly with increasing temperature.

In 1995, Moodera et al. reported the first observation of a large TMR at room temperature [73]. With a tunneling junction of two ferromagnetic layers (Co, Fe, Ni or their alloys) and a carefully fabricated Al_2O_3 barrier in between, large TMR values of $\approx 10\%$ were obtained. Surprisingly, a completely different bias voltage and temperature dependence of the TMR was found(see Fig. 4.25). There is no strong temperature dependence of the TMR. The TMR value at 77 K is nearly the same as that at 4.2 K. Even at room temperature, it still has $\approx 50\%$ of

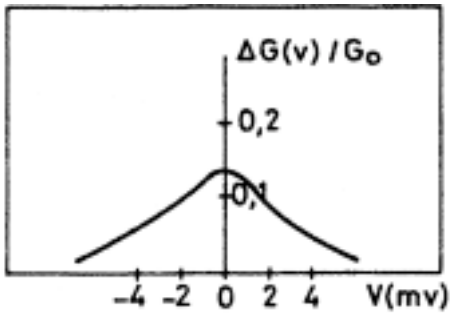

Figure 4.24: Relative conductance ($\Delta G/G$) versus DC bias for Fe-Ge-Co junctions at 4.2 K. ΔG is the difference between the two conductance values corresponding to parallel and antiparallel magnetization of the two ferromagnetic films (after Ref. [30]).

the value at 4.2 K. Secondly, the TMR is nearly constant for a bias voltage below 90 mV which completely disagrees with the above mentioned experiments of Julliere. The bias voltage value at which the TMR ratio decreases in value by half ($V_{1/2}$) is increased to ≈200 mV.

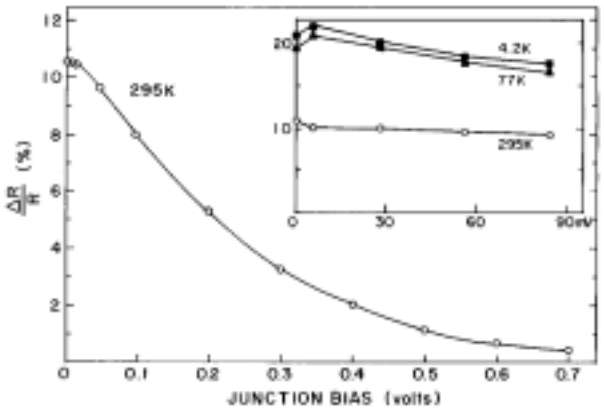

Figure 4.25: The ratio of ΔR/R plotted as a function of the bias for CoFe/Al_2O_3/Co junction. Inset: Low bias region at three different temperature. The abscissa in the inset is for 4.2 K data, which are twice the values at 295 K. The increase in ΔR/R as T decreased is seen in the inset. (after Ref. [73]).

One may attribute the different dependence to different types of junctions. For the same type of Fe/Al_2O_3/$Fe_{50}Co_{50}$ junctions, however, Yuasa et al. [75], found that the bias voltage dependence of the TMR varies with the thickness of the Al_2O_3 barrier. The thicker the barrier, the stronger the bias voltage dependence for the junctions with barrier thickness from 14 to 30 Å. The $V_{1/2}$ changes from 700 mV for the junction with 14 Å barrier thickness to 300 mV when the barrier thickness increased to 30 Å. They attributed the effect to the increase of impurity

scattering with the barrier thickness.

This discrepancy stimulated many theoretical and experimental studies. Not only based on basic research interests, but also from the application point of view, the decrease of the TMR ratio with increasing bias voltage across the junction is a serious problem, because it limits the sensing voltage for devices and by this, the signal-to-noise ratio. Additionally, a temperature independence of the TMR is also desirable for practical reasons. Up to now, several mechanisms have been proposed to explain the decrease of the TMR with the bias voltage. They are briefly summarized as the following:

1. **Bandstructure effects:**
   Bratkovsky attributed the effect to the electric field that is present in a biased barrier [88, 89]. The electric field skews the barrier's shape, thus making it more transparent for "hot" electrons to tunnel at energies where the difference between the DOS of majority and minority carriers is reduced. As a result, the TMR in the direct tunneling decreases with increasing bias voltage.

2. **Magnon excitation:**
   In magneto-tunneling spectroscopy, a zero bias anomaly is usually found at low temperatures. Zhang et al. [90] explained this effect with hot electrons producing excitations like magnons. This mechanism was expanded to explain the decrease of the TMR with increasing bias by Moodera et al. [91]. Due to the excitation of magnons, the magnetization of the tunneling electrodes are not strictly parallel or antiparallel. Besides, the excitation of magnons might also cause spin-flip scattering. Hence, a reduction of spin polarization and the TMR effect is expected. With inelastic electron tunneling spectroscopy (IETS), they found additional peaks which could be attributed to magnons generated in the FM electrodes.

3. **Nonmagnetic impurity induced two-step tunneling:**
   As the barrier of the tunneling junction is usually formed by the oxidation of a nonmagnetic metal, amorphous layers are formed. The amorphous layer has locally different electronic structures which cause localized states available for tunneling. Additionally, in most cases either the oxidation of the barrier layer is incomplete or an oxide of the ferromagnetic metal may form at the interface. The existence of impurities causes localized defect states in the barrier. Excitation of electrons from these states, either thermally or by hot electron impact, create states available for two-step tunneling. Because these states are not spin-polarized, the two-step tunneling is spin independent and has no contribution to the TMR. Hence, the TMR effect decreases with bias voltage. Theoretically, the calculation by Tsymbal and Pettifor [49] reveals a strong influence of impurities within the barrier on the TMR. Experimentally, similar tunneling junctions prepared with different methods and of different concentration of impurities show a different dependence of the TMR on the

bias voltage [78, 79]. Further, intentionally doped junctions show stronger dependence on the bias voltage. These results obviously support the strong influence of impurities on the TMR effect.

4. **Spin dependent scattering caused by magnetic impurities:**
   Jansen and Moodera [92] studied the influence of magnetic impurities inside the barrier by comparing the bias dependence of the TMR effect with dopants inside the barrier. They found the TMR effect shows a stronger dependence on the bias voltage when the dopants are magnetic ions. The magnetic ions inside the barrier form spin-flip scattering centers. The spin-flip scattering can be enhanced by the applied voltage. In this way, the TMR effect decreases.

5. **Interface effects:**
   Besides the above mentioned mechanisms, orange peel coupling due to surface roughness may also influence the bias dependence of the TMR effect [93, 94].

Which one, among all these mechanisms, plays the most important role for the decrease of the TMR with bias voltage is still unclear. Unfortunately, it is hard to exclude one of the mechanisms mentioned above in planar junctions due to the complicated barriers. Magneto-tunneling through a vacuum barrier studied by Spin-polarized STM is obviously of great advantage in the sense that it offers a tunneling junction with the best quality barrier. There are neither nonmagnetic impurities nor magnetic impurities inside the barrier. Moreover, a constant tip-to-sample distance is kept in STM, the influence of the surface roughness can be safely excluded.

4.5.2 Voltage dependence of the TMR across a vacuum barrier

For the study of voltage dependence of the TMR across a vacuum barrier, two different methods are used to measure the magneto-tunneling spectroscopy. First, we record the magnetic contrast as a function of the bias voltage with a fixed tunneling current, i.e., the tip-to-sample distance is not a constant. Second, the tunneling current and magnetic contrast are recorded simultaneously as a function of the bias voltage with the feedback off. In this way, we avoid a change of the TMR due to the tip-sample separation.

First, we discuss the results obtained with the first method. We recorded the magnetic contrast as a function of the bias voltage while keeping the tunneling current constant. The magnetic contrasts are recorded as the average values of 20 line scans. Fig. 4.26 presents the bias voltage dependence of the TMR for 3 different tunneling currents obtained with the first method. The error bars display the statistical errors. We can see that they show a different behavior for different tunneling currents. At 0.5 nA, the magnetic contrast seems nearly independent on the bias voltage. At 5 nA, the magnetic contrast decreases when the bias voltage is approaching zero. In case of 45 nA, the decrease becomes much stronger and the TMR nearly disappears at zero

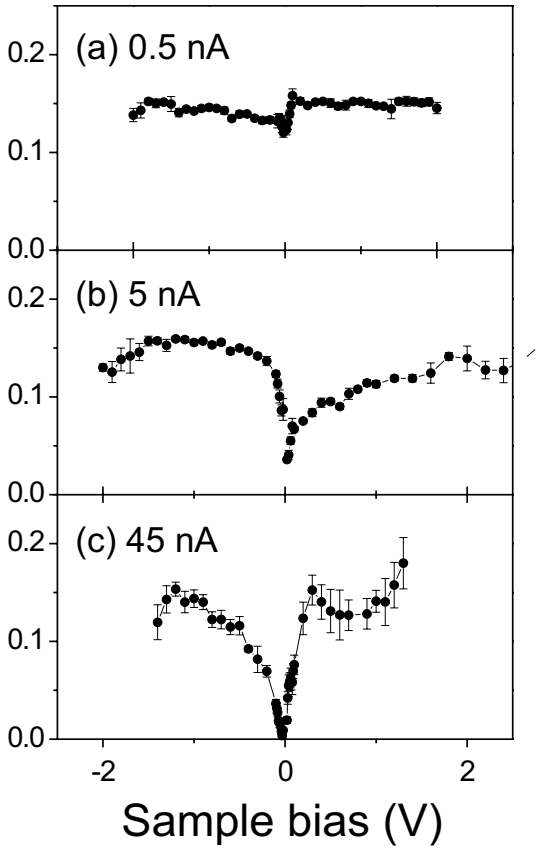

Figure 4.26: Bias voltage dependence of the TMR at different tunneling current conditions obtained on a clean Co(0001) sample. (a) 0.5 nA, (b) 5 nA, (c) 45 nA. Note, the tip-to-sample distance also changes as the bias voltage changes.

bias. In the constant tunneling current mode, the distance between the tip and sample changes with the bias voltage (see Eq. 4.13). When the bias voltage is reduced, the tip approaches the sample surface. Assuming that the TMR is not strongly dependent on the bias voltage, this would add an additional evidence for the distance dependent TMR discussed in previous section as the tip-to-sample distance decreases when the tunneling resistance decreases. As pointed out above, when the tip is situated at large distance above the sample surface, the magnetic contrast is nearly independent on the tip-to-sample distance. Hence, we may attribute the spectroscopic measurement at 0.5 nA shown in Fig. 4.26a as a pure voltage dependent measurement. It indicates an independent behavior on the bias voltage. This is indeed surprising as in all planar junction measurements, the tunneling magneto resistance effect is found to strongly decrease with increasing bias voltage.

To further confirm our experimental results and fully exclude distance dependent effects, we also investigated the pure voltage dependent TMR effect. At each pixel, the feedback loop

was switched off for a short time. In this way, a constant tip-sample separation is kept during the spectroscopic measurement. The lock-in output signal as well as the tunneling current were recorded simultaneously as the function of the bias voltage.

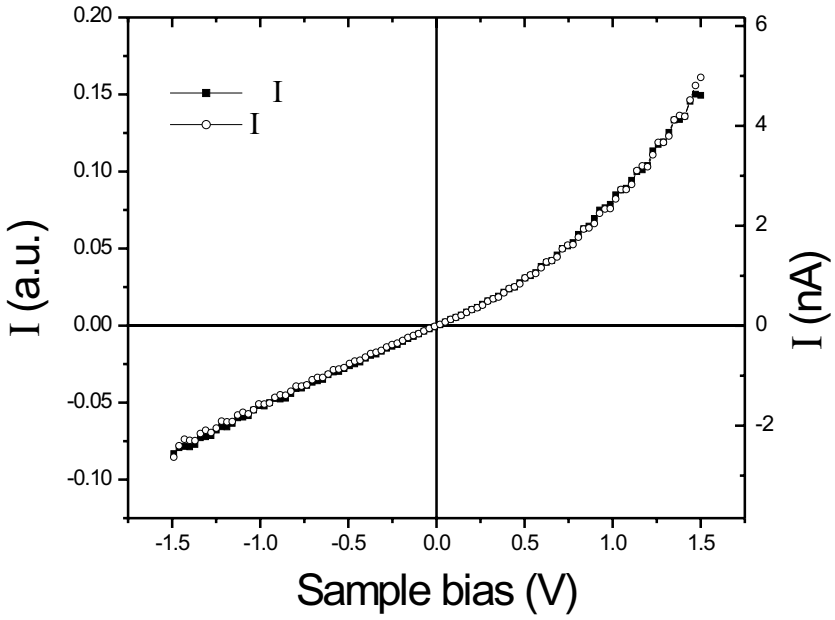

Figure 4.27: The magnetic contrast across a magnetic domain wall ΔI and the tunneling current as a function of the bias voltage in a constant tip-sample separation condition. The tip is stabilized at 1 V, 1 nA.

Fig. 4.27 presents the result of the bias voltage dependent tunneling current (empty circles) and the difference of the lock-in signal across the domain wall (filled squares). The tunneling condition for stabilizing the tip was 1V, 1nA. For comparison, we plot both the tunneling current and the difference of lock-in signal across the domain wall in the same plot. From the figure, we can clearly see that both curves are almost identical except that their scales are different. The TMR effect, which is obtained as the difference of the lock-in signal across the domain wall normalized to the tunneling current, i.e., $\Delta I/I$ is obviously a constant in the bias voltage range from -1.5 V to 1.5 V.

As two independent measurements show the same result, we have to attribute the effect to physics although it is completely different to the behavior of planar junctions. To understand the effect, we have to consider the difference of the magneto tunneling through a vacuum barrier and the tunneling junction across an insulator barrier. As summarized above, the decrease of the TMR effect with the bias voltage for planar junctions may be correlated with five major

mechanisms. They are, bandstructure effects, magnon excitation, nonmagnetic impurity induced two step tunneling, spin scattering caused by the magnetic impurities and the interface quality related effects. In our case of magneto-tunneling through a vacuum barrier, the experiments are performed in ultra high vacuum on a clean Co(0001) single crystal with Sp-STM. Neither nonmagnetic impurities nor magnetic impurities are present inside the barrier. As Sp-STM is working on a small area of a clean single crystal in a constant current mode (a constant tip-sample separation), the effect caused by the interface quality should also be minimized. Hence, the last three mechanisms mentioned above can be safely excluded. In the following, bandstructure effects and the effect caused by magnon excitation will be discussed.

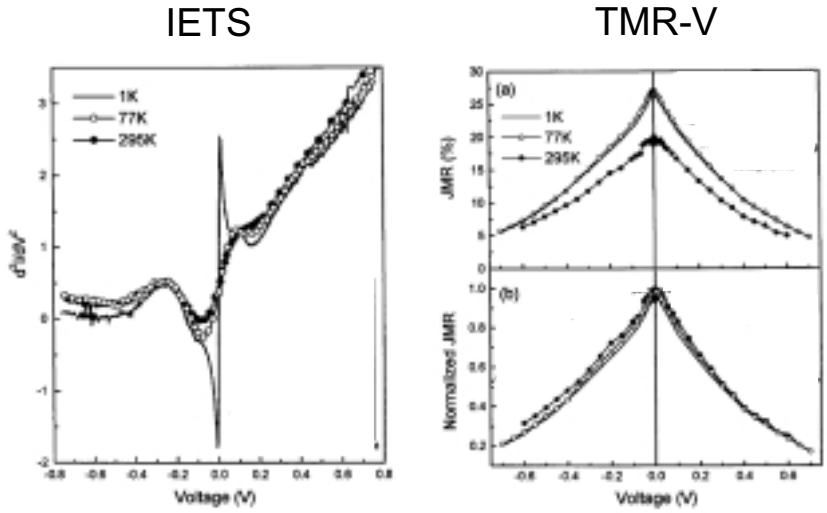

Figure 4.28: Comparison of IETS and bias dependent TMR at different temperatures. Figures are cited from [91].

The mechanism of magnon excitation was first proposed by Zhang et al. [90] to explain the zero bias anomaly in the conductance and tunneling magneto resistance of ferromagnetic tunnel junctions. Later, the mechanism was expanded by Moodera et al. [91] to explain the decrease of the TMR with the bias voltage. In their paper, they tried to confirm their argument with inelastic tunneling spectroscopy (IETS) measurements. Theoretically speaking, the existence of magnons would cause a reduction of magnetization and spin polarization of the electrodes so as to decrease the TMR. However, whether the magnons influence the bias voltage dependence of the TMR or not is still unclear. From the temperature dependent IETS spectrum and the TMR spectrum shown in their paper, it seems there is no direct correlation between these two effects. Even assuming the observed peaks in IETS are caused by magnon excitation as they claimed, it is still hard to find the correlation between magnons and the decrease of tunneling magneto resistance effect with increasing bias voltage. From the IETS spectra shown in Fig. 3 in that paper (see the left part of Fig. 4.28), the IETS spectrum at 77 K is quite similar to

that obtained at 295 K and they are completely different to the spectrum obtained at 1 K. However, the bias voltage dependence of the TMR is just the opposite (see the right upper part of Fig. 4.28). The data obtained at 1 K and 77 K are nearly identical and they are different to the data obtained at 295 K. Hence, magnon excitation might not be the dominant mechanism for the decrease of the TMR with bias voltage and in some cases (at room temperature) it could even be neglected. Further, in the paper of Moodera [91], the normalized TMR with the bias voltage at different temperatures can be fitted in a single curve (see the right lower part of Fig. 4.28). This cannot be explained with the picture of a drop of the TMR with bias voltage caused by magnon excitation as it should be different at different temperatures. Additionally, the zero bias anomaly have been extensively studied [95] specifically in nonmagnetic junctions where magnetic impurities or impurity layers were placed within one of the electrodes or within the insulating barrier. The effect found in magneto-tunneling junctions could be also related to the spin-flip scattering due to magnetic impurities existing inside the tunneling barrier [96]. It is not trivial to make a magneto-tunneling junction without magnetic impurity inside the barrier except when vacuum barrier is used as in our experiments.

Bratkovsky [88] included bandstructure effects into the calculation for the bias voltage dependent TMR effect. He pointed out that the presence of the electric field in a biased barrier skews the barrier's shape, thus making it more transparent for "hot" electrons tunneling at energies where the difference between the DOS of majority and minority carriers is changed so as to cause a bias voltage dependent TMR effect. The application of this calculation for Fe-Al_2O_3-Fe [91] and CoFe-Al_2O_3-NiFe [89] junctions resolves a similar decrease of the TMR with bias voltage. In both calculations, the bias voltage at which the TMR value is half of the TMR value at zero bias, $V_{1/2}$ is around 750 mV. A similar junction, Co-Al_2O_3-$Ni_{80}Fe_{20}$, prepared with a better technique [78], however, shows less tendency of the TMR decrease with increasing bias voltage. The $V_{1/2}$ is above 800 mV. In the paper, the authors also compared the magneto-tunneling junctions prepared with different techniques and emphasized the importance of the quality of the tunneling barrier. The better quality of the tunneling barrier, the less bias voltage dependence of the TMR. Even with this good preparation technique, the effective barrier height and effective barrier thickness are still smaller than the expected values, i.e., the tunneling barrier is still far from perfect. One can imagine that a smaller dependence of the TMR with the bias voltage would be expected if the barrier is getting better, for instance an impurity free barrier like a vacuum barrier. Additionally, the decrease of the TMR with bias voltage is found experimentally to depend on the barrier height. The higher the barrier, the less bias voltage dependence of the TMR. In planar junction, the barrier is formed by metal oxide and the electrodes are ferromagnetic metals or their alloy, the barrier hight is around 2-3 eV in the best case. In our experiments, the tunneling is through a vacuum barrier, the barrier height is estimated to be around 6 eV, which is more than the double value of the barrier height for planar junctions. Hence, for the tunneling through a vacuum barrier, a much smaller dependence

of the TMR value on bias voltage should be expected. Besides, as addressed by Bratkovsky, one really needs to consider the real bandstructure of both the tunneling electrodes and tunneling barrier to calculate the bias dependent TMR effect.

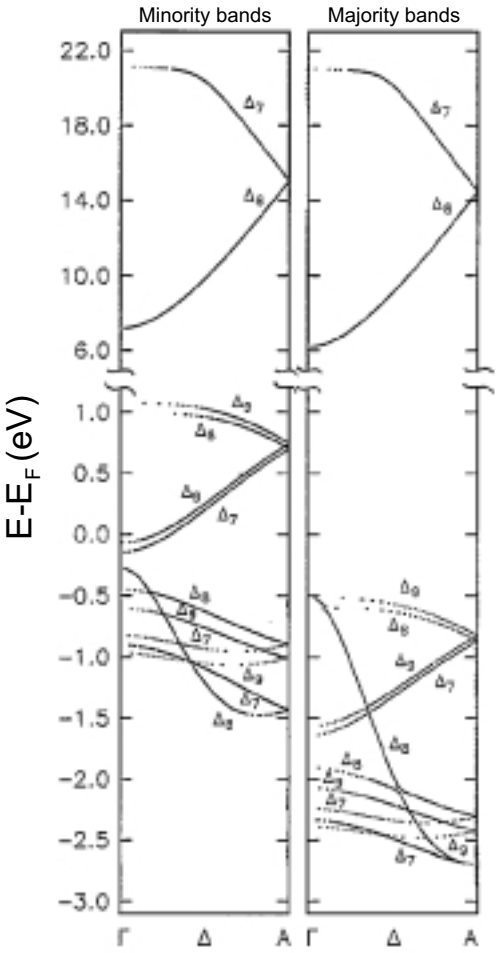

Figure 4.29: Calculated relativistic band structure of hcp-Co(0001) for majority and minority electrons along the $\Gamma-\Delta-A$ direction corresponding to the bands with wavevector perpendicular to Co(0001) surface. After Ref. [97].

Fig. 4.29 presents the calculated relativistic band structure of hcp-Co(0001) for both majority and minority electrons along the $\Gamma-\Delta-A$ direction corresponding to the bands with wave vector perpendicular to Co(0001) surface. At large tip-sample separations, states with wave vector perpendicular to the sample surface dominate the tunneling as the electron wave functions in the vacuum region decay asymptotically as $\exp[(\kappa^2 + k_{\|}^2)^{1/2} z]$ where κ is the imaginary wave vector inside the vacuum and $k_{\|}$ is the wave vector parallel to the sample surface [64]. Therefore, the states showing in Fig. 4.29 dominate the tunneling when electrons tunnel between the tip

and Co(0001) surface. From this figure, we can see that there is no majority band available for the tunneling from 0.5 eV below the Fermi level up to 6 eV above the Fermi energy. At positive bias voltage, the electrons tunnel from the tip Fermi surface into the empty states of the sample. As shown in Fig. 4.29, there is only one band available for tunneling around $k_{\|} = 0$. Therefore, no voltage dependence is expected. At negative bias voltage, the electrons tunnel from the sample Fermi energy into the tip. In this case, the density of states of the tip determine the bias voltage dependence of the TMR. Usually, the density of states in an amorphous tip has no features, i.e., no bias voltage dependence. Hence, a constant TMR behavior should be found. This explains our experimental finding, i.e., an independent TMR on the bias voltage.

Above, we discussed the TMR at large tip-sample separation. It is nearly constant from -1.5 V to 1.5 V. At this large tip-sample separation, the states with wave vector perpendicular to the sample surface dominate the tunneling as pointed above. When the tip further approaches towards the sample surface, states with $k_{\|} \neq 0$ contribute to the tunneling. As one example, the surface states, which $k_{\perp} = 0$, can be much more pronounced in the spectra when the tunneling tip approaches to the sample surface [98]. For Co(0001), there are several surface states near the Fermi energy. Therefore, a bias voltage dependent TMR effect could be found at small tip-sample separation. In order to check this, we performed magneto-tunneling spectroscopic measurements at 100 mV, 1 nA, i.e., similar measurements as in Fig. 4.27 but at smaller tip-sample separation.

Fig. 4.30 presents the result of magneto-tunneling spectroscopic measurements where the tip was stabilized at 100 mV,1 nA. Fig. 4.30(a) shows the bias voltage dependent tunneling current. It is nearly linear with bias voltage at small bias and becomes exponentially at large bias. Very interestingly, the bias voltage dependent TMR (c) shows a completely different behavior as the measurement performed at 1 V, 1 nA (d). It shows a strong drop at ≈ 0.2 V. The TMR value obtained at 1 V, 1 nA is almost 2 times higher than that at 100 mV, 1 nA is caused by the tip-to-sample distance change as has been discussed in previous section. When the tip is closer to the sample surface, not only the electrons with wave vector fully perpendicular to the sample surface but also the other electrons are involved in the tunneling. Even the surface states with wave vectors fully parallel to the sample surface can be observed by STM at small tip-to-sample distances. The drop of the TMR at +0.2 V may come from the bulk states with wave vectors not strictly perpendicular to the sample surface or from the surface states. This is still an open question and needs further theoretical calculations to be understood, completely.

In summary, the bias voltage dependent TMR across a vacuum barrier is studied. At large tip-to-sample distance, the TMR is independent on the sample bias. This finding excludes the magnon excitation as the dominant mechanism for the TMR drop with bias voltage. In comparison with the bias voltage dependent TMR for planar junctions, we conclude that impurities inside the tunneling barrier or at the interface, which cause two-step tunneling or spin dependent scattering, are the dominant mechanisms for the TMR decrease with increasing bias voltage.

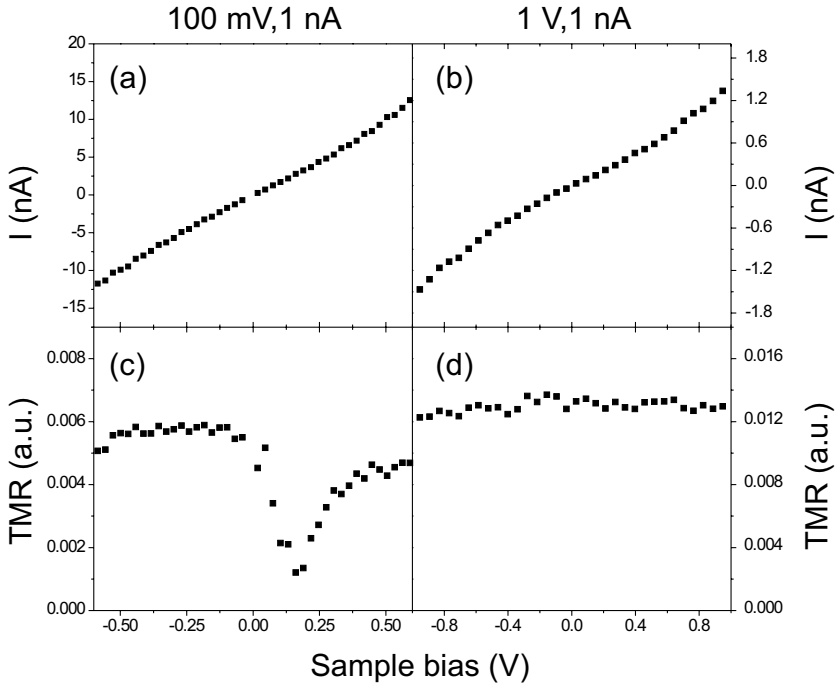

Figure 4.30: A typical tunneling current (a) and TMR (c) as a function of the bias voltage on a clean Co(0001) surface obtained with the tip stabilized at 100 mV, 1 nA. (b)&(d) is the similar measurement as (a)&(c) with the same tip, but obtained with the tip stabilized at 1 V, 1 nA.

For small tip-to-sample distances a strong drop of the TMR at ≈0.2 V is found. This may be caused by the contribution of electrons with wave vector not fully perpendicular to the surface.

4.6 Spin-polarized tunneling through a nonmagnetic spacer

In general, spin-polarized scanning tunneling microscopy is a surface sensitive technique to probe the magnetic structure of the sample surface. From how deep Sp-STM obtains the information, however, still remains an open question. Covering the magnetic sample with a thin nonmagnetic metal layer and studying the spin contrast as a function of the thickness of this layer gives the direct answer to this question.

In case of planar junction, the TMR in the presence of a nonmagnetic spacer layer inserted between the insulating layer and one of the magnetic electrodes has been studied intensively. In the first experiments, Moodera et al. [99] measured the spin polarization in $Al/Al_2O_3/Au/Fe$ junctions as a function of the Au interlayer thickness d, finding that the polarization decreases rapidly for the first 2 ML Au but decreases with $1/d$ at larger thickness. In the context of magneto-tunneling junctions, the calculations by Vedyayev et al. [100] and Zhang et al. [101] predicted oscillations of the TMR as a function of the thickness of the nonmagnetic layer. These calculations show that the interface layer induces quantum well states (QWS) when a resonance condition is fulfilled. Later Moodera et al. indeed found weak oscillations and further confirmed the QWS with spectroscopic measurements [52]. The experimental results by Sun et al. [102] also show a fast decay of the TMR for thin nonmagnetic layers and a slow decrease of the TMR at larger nonmagnetic layer thickness. When Parkin et al. [103] investigated the TMR as a function of the thickness of a nonmagnetic layer grown on Al_2O_3, a large spin polarization was maintained over distances in excess of 10 nm, in striking contrast to the earlier experiments of Moodera et al. as well as later experiments of Sun et al. To clarify these conflicting results, Zhang et al. [104] have argued that the behavior of the TMR in the presence of an interfacial nonmagnetic layer critically depends on the quality of the interfacial layer, e.g., the thickness fluctuations in a short length scale. Mathon et al. recently found that quantum well states in the metallic interlayer are necessary for a non-vanishing TMR, even in the limit of coherence loss [105]. Experiments by LeClair et al. [106], however, show an opposite behavior. They compared tunneling junctions of $Co/Al_2O_3/Co$ with a nonmagnetic Cu spacer inserted at different positions, i.e., under or over the Al_2O_3 barrier and found different decay behaviors for the TMR as a function of the Cu thickness. The junctions with Cu films of better quality have a stronger decrease of the TMR effect. In all these experiments, the tunneling barriers were formed by amorphous Al_2O_3. During the preparation of the tunneling barriers, i.e., the oxidation of a Al metal layer, there could be either unoxidized Al impurities remaining in the tunneling barrier or oxidation of magnetic electrode may happen at the interface. Intermixing of the nonmagnetic spacer with the barrier or the tunneling electrodes may be present when it is inserted between them. In our experiments, a UHV Sp-STM is used and all experiments are performed in ultra-high vacuum. The tunneling barriers are formed by vacuum, the effect of impurities can surely be excluded.

The system Au/Co(0001) is chosen for our measurements. Since the surface energy of

Au(111) is lower than that of Co(0001) [107], Au atoms will remain on top of Co atoms and wet the surface, i.e., no strong roughness and intermixing is expected. The Au films are deposited on the Co(0001) surface by means of e-beam evaporation at room temperature. The Au source mounted in a Mo crucible is heated by e-beam bombardment for evaporation. To check the growth mode of Au/Co(0001) as well as to calibrate the growth rate of the evaporation, we performed STM measurement before and after the deposition of Au.

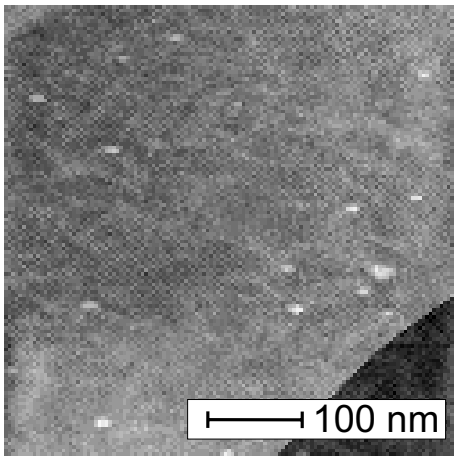

Figure 4.31: Topography measurement of a clean Co(0001) surface with one monolayer step.

Fig. 4.31 presents an STM measurement on a clean Co(0001) surface. Due to the limited annealing temperature, the surface remains with a low concentration of small defects - either sputter defects or local fcc or misoriented hcp areas as pointed in Sect 4.2. The island concentration was estimated to be less than 0.05 ML.

Fig. 4.32a shows a STM image of Co(0001) after 20 min depositing of Au which corresponds to ≈2.6 ML coverage. The substrate is nearly filled and only a small concentration of islands appear on top of the closed film. The figure shows that Au deposited on Co(0001) grows in a two dimensional mode. With a line profile across the several islands shown in Fig. 4.32b, the island height is estimated to be roughly 4.5 Å, indicating a double layer growth. Hence, the deposition rate of Au can be estimated to be ≈ 0.13 ML/min. Additionally, the deposition rate was crosschecked with the film after 5 min deposition of Au. The same deposition rate is obtained which indicates a good stability of the evaporator and a high reproducibility of the experiments.

Since the domain pattern on the Co(0001) surface is rather complex with a variety of different types of domains, it is not trivial to study the domain contrast as a function of Au thickness. In the case that the sample is transferred out of STM stage for the deposition and inserted back for observation, it is practically impossible to find back the same domain. In order to compare the magnetic contrast of different Au coverages it is better to compare the change of contrast of the

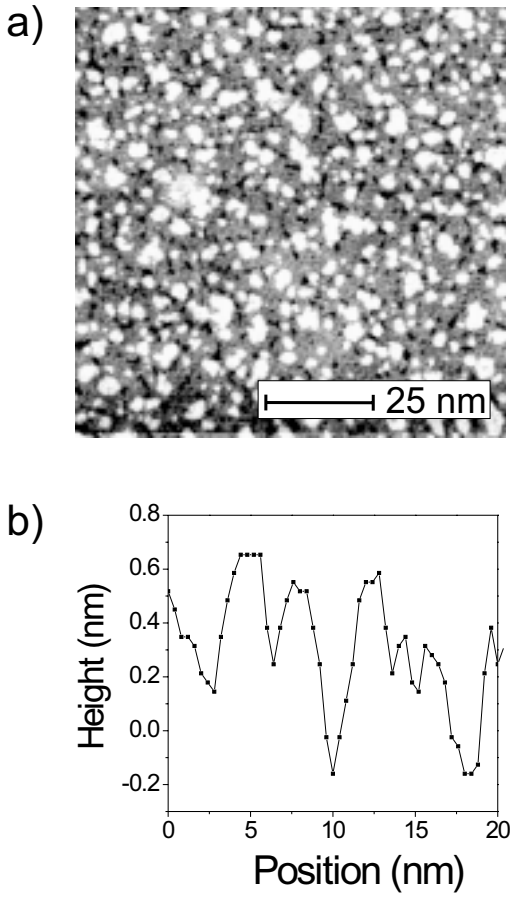

Figure 4.32: (a) STM measurement of Co(0001) surface with 20 min deposition of Au. (b) A line profile of the morphology indicates a double layer growth.

very same domain, i.e., a domain at the same sample position. To satisfy this condition, the Au evaporator is mounted in the STM stage to perform a real in-situ measurement. It is mounted in such a way that deposition is carried out under a glacing incidence between the sample and the tip. After scanning each image, the tip is retracted by several coarse steps ($\approx$ 30 μm) from the sample surface for the deposition of Au. With this relatively short retraction, the same position of the sample surface can be found after a new approach. Note that the above mentioned deposition rate was calibrated with tip retracted by several coarse steps. We also performed the calibration with the tip fully retracted. No difference was observed. Hence, the tip-to-sample distance is sufficient for Au deposition.

Fig. 4.33a presents a magnetic domain image obtained with Sp-STM on a clean Co(0001) surface. It shows a dendritic like domain pattern as usually found on Co(0001). Fig. 4.33b-d present the magnetic domain pattern with 1.3, 2.6 and 3.9 ML of Au cover layer. The domain

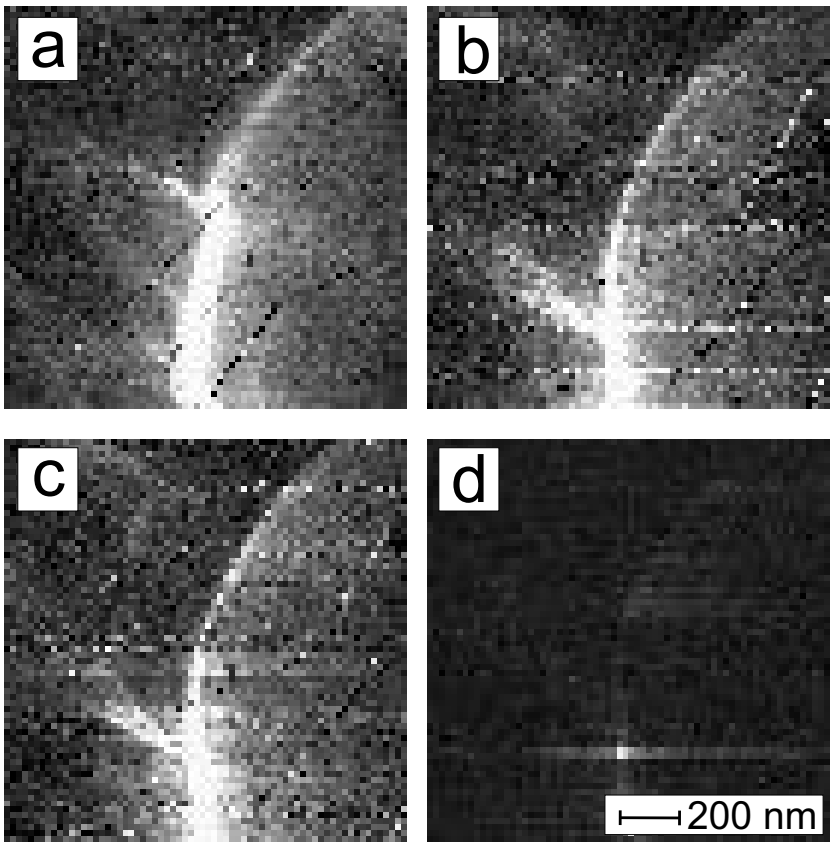

Figure 4.33: Sp-STM image of Co(0001) with the same tip for different coverages of Au. (a) clean Co(0001) (b),(c) and (d) are images with ≈ 1.3, 2.6 and 3.9 ML of Au.

pattern remains almost the same after covering the Au layer. The relative contrast, however, is different for different Au coverages. The contrast of the sample with 1.3 ML coverage of Au is only a little bit weaker than the sample without Au layer. When the thickness of the Au layer is increased to 3.9 ML, the contrast, however, nearly vanishes. With a deposition of 1.3 ML more of Au, no contrast was observed within our Sp-STM sensitivity.

To further quantify the decrease in contrast with increasing Au thickness, the contrast across each scan line was recorded and averaged for each coverage. The result and its error margin is shown in Fig. 4.34. The magnetic contrast shows an almost linear decrease with Au coverage. The TMR effect almost reaches zero when the thickness of the covered Au layer is ≈4 ML.

During the deposition of Au, the evaporator source also degases as it is heated up to high temperature. There are some gases coming from the evaporator source (most of it is H_2). To demonstrate that there is no influence of the gas adsorption on the TMR effect as well as exclude effects caused by tip changes during the deposition of Au, we performed Sp-STM measurement in the shadow of the tip. At this position, no Au is present since it was shadowed by the tip during

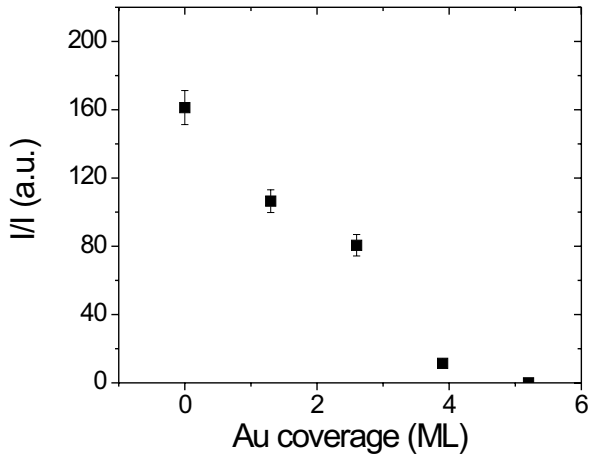

Figure 4.34: The TMR ($\Delta I/I$) as a function of Au coverage.

the previous deposition. If gas like CO absorbed, it would strongly reduce the spin polarization of the surface atom so as to reduce the TMR [108]. As CO gas sticks more efficiently to Co than Au, a stronger decrease of the TMR would be expected in the shadow of the tip. In other words, if large TMR signals can be found in the shadow of the tip, the influence of the gas absorption on the sample and the tip can be excluded.

To check this, we moved the tip along its shadow to another position which is nearly 50 μm away from the position where above mentioned measurements were performed. As Au islands can be distinguished in size with STM from the Co islands after annealing (see Fig. 4.31 and Fig. 4.32), we can cross-check if the observed area is in the shadow of the tip. We found indeed that there was no Au at this position. Sp-STM measurements show magnetic domains with high contrast in the shadow. Therefore, we can conclude that there is no significant change of the tip during the whole experiment. The influence of gas absorption can also be excluded. To check the reproducibility of the previous mentioned measurement, ≈2.6 ML of Au was deposited at this position and repeated the Sp-STM measurement. The obtained contrast is found to be nearly 50% of its original value which reveals the good reproducibility of the above measurement with this tip.

When the same measurement was repeated with different tips, the Au thickness dependence of the TMR, however, is different. Fig. 4.35 presents the TMR as a function of the Au coverage for 3 different tips. They are normalized to the value obtained on clean Co(0001) surface. The results for 3 different tips are different. The TMR can either strongly/weakly decrease or even slightly increase with the Au coverage. As the tunneling conditions (bias voltage and tunneling current) used for these measurements are exactly the same, the influence of bias voltage can be

excluded. Besides, as we addressed above, the influence of gas absorption can be neglected. One might suspect that the evaporation rate can change for different measurement. The evaporation rate estimated from the topographic images, however, gave almost the same result. Additionally, AES measurements also confirmed identical Au deposition rates. Besides, double layer growth mode was always found for these measurement when the thickness is below 6 ML. Therefore, a different dependence of the TMR on Au thickness due to a different surface roughness can be excluded. Hence, we have to attribute the different dependence of the TMR on the Au coverage to the different tips. As we used amorphous CoFeSiB tips whose ends are hard to control, the apexes could have different composition or different structures. This might influence the Au coverage dependence of the TMR.

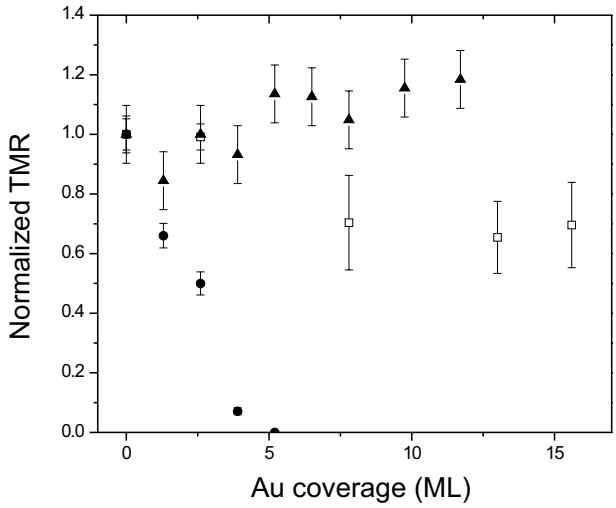

Figure 4.35: The TMR ($\Delta I/I$) effect as a function of Au coverage for 3 different tips.

Generally speaking, there are 2 different physical phenomena that influence the TMR when the electrons cross the additional deposited Au layer. First, as the potential of the Au layer is lower than that of both vacuum and Co electrode, quantum well states (QWS) may form in this layer and resonant tunneling may occur. Due to the exchange splitting of the Co, the spin-up and spin-down electrons occupy different energies. This would cause a different transmission and reflectivity for spin-up and spin-down electrons at Au/Co interface, i.e., the quantum well states are different for spin-up and spin-down electrons. Hence, a change of the TMR due to the inserted Au film is expected. And second, spin scattering in the Au layer decreases the spin polarization of the tunneling electrons. The mean free path (the distance for electrons propagating coherently) in Au has been estimated to be around 25 nm near the Fermi energy [109] and a few eV above [110]. Hence, a slow decay is expected.

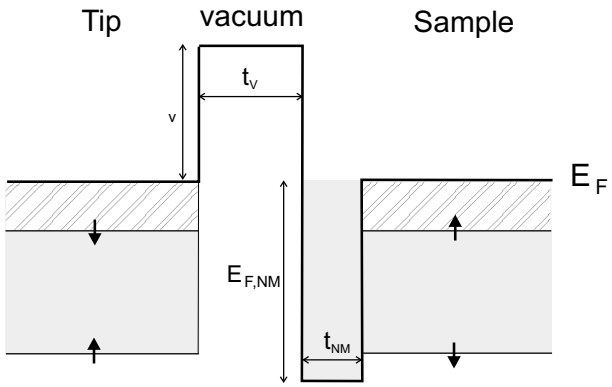

Figure 4.36: Schematic potential for the electrons tunneling between the tip and the sample surface in the presence of a nonmagnetic metal layer inserted between the sample and vacuum. The antiparallel configuration between the tip and the sample magnetization is displayed in this figure.

In the following, we will discuss how the quantum well states influence the TMR in one dimensional free electron model which was first proposed by Slonczewski [34]. Similar calculations have been carried out by Moodera et al [52]. The configuration used in this calculation consists of two ferromagnetic electrodes, the tip and the sample, a vacuum barrier with the width of t_v, and a nonmagnetic metal layer with the width of t_{NM} (see Fig. 4.36). For simplicity, the tip and the sample are assumed to have the same bandstructure. The Fermi energy is chosen to correspond to the spin-split free electron like itinerant d-electron bands of Co, i.e., $E_{F,FM\sigma} = 0.83 \pm 0.5$ eV for the majority (minority) spin electrons [41]. The barrier height and barrier width are chosen, $\phi_v = 5$ eV and $t_v = 0.7$ nm, respectively. The electronic parameters of the NM metal layer of thickness t_{NM} are chosen to correspond to those of Au [111], i.e., $E_{F,NM} = 5.51$ eV. All electrons are assumed to have free electron mass and the calculations are performed for zero temperature.

Fig. 4.37 shows the calculated TMR as the function of the nonmagnetic film thickness t_{NM}. As can be seen, the TMR rapidly oscillates between positive and negative values due to QWS which develop when the round trip phase accumulation equals 2π. The period equals $\pi/k_{F,NM}$, with $k_{F,NM}$ the Fermi vector inside the NM layer. It seems that the TMR oscillates forever if there is no phase coherence breaking or spin scattering. The breaking of phase coherence in a thick interface layer results in quenching of the TMR [100, 104]. As in experiments t_{NM} is varied in monolayer steps only, Fig. 4.37 also shows intersections for several monolayer thicknesses $t_{ML,NM}$. This aliasing effect results in oscillations with a much longer period. For a monolayer thickness of 0.2355 nm, corresponding to the perpendicular bulk lattice parameter of Au(111), the TMR initially increases and crosses zero value when the thickness is around 6-7 ML. However, the nonmagnetic layer thickness dependent TMR effect strongly depends on the monolayer

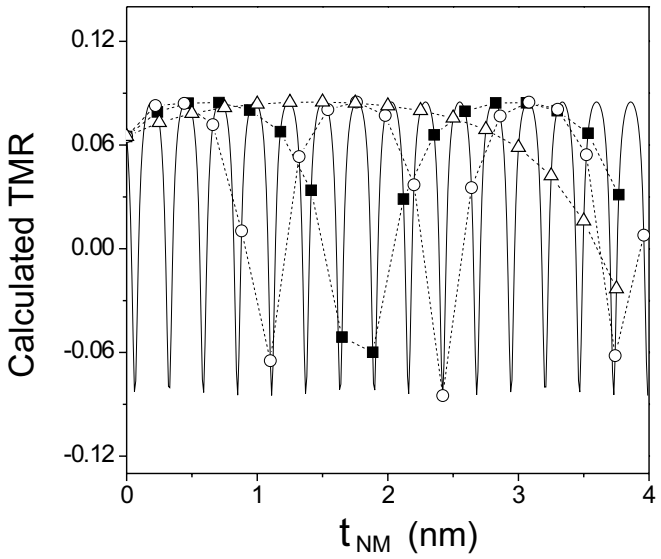

Figure 4.37: Calculated nonmagnetic metal layer thickness dependence of the TMR at zero bias, using $E_{F,FM} = 0.83 \pm 0.5$ eV for both the tip and the sample, $E_{F,NM} = 5.51$ eV, $\phi_v = 5$ eV, and $t_v = 0.7$ nm. The continuous variation is intersected at full monolayer coverages (dashed lines): (○)$t_{ML,NM} = 0.22$ nm, (■) 0.2355 nm (Au(111)), and (△)0.25 nm.

thickness of the nonmagnetic layer. When a different ratio between the monolayer thickness and the Fermi wavelength inside the NM layer is used, the result is different. For a monolayer thickness of 0.22 nm, a much quicker decrease in comparison with the monolayer thickness of 0.2355 nm is found. A much slower decrease can also be found for $t_{ML,NM} = 0.25$ nm. One can imagine that when the monolayer thickness is exactly the same as the oscillation period, $t_{ML,NM} = \pi/k_{F,NM}$, no thickness dependent TMR behavior is expected. Hence, with different ratios between the monolayer thickness and the Fermi wavelength inside the NM layer, different thickness dependent TMR behaviors are expected.

In the one dimensional free electron model, the transmission coefficient of a quantum well depends only on both the incident and emitted wave vector as well as the properties of the well itself, the wave vector and well width [112]. The emitted wave vector is the wave vector of the Co sample which should be constant for different measurements. The incident wave vector is the wave vector inside the vacuum barrier which is determined by the barrier height. The barrier height might be different for the different tips as their sharpness can be different. However, the magnitude of the barrier height change should not be large. Fig. 4.38 presents the calculated TMR as a function of the nonmagnetic thickness with $t_{ML,NM} = 0.2355$ nm for 3 different barrier heights. We can see that there is only a small difference for the NM thickness dependent TMR between 3 and 5 eV barrier height.

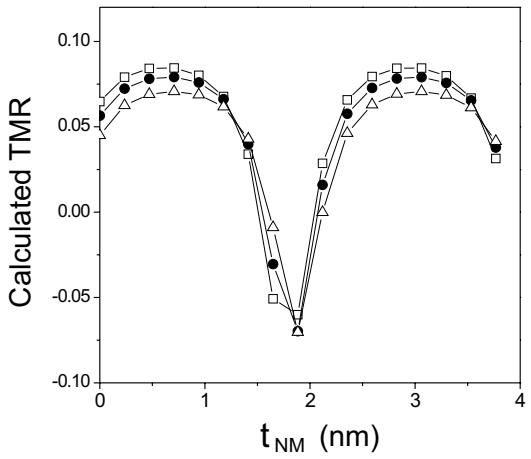

Figure 4.38: Similar calculation as in Fig. 4.37 with $t_{ML,NM} = 0.2355$ nm for 3 different barrier heights: (□)$\phi_v = 5$ eV,(•)$\phi_v = 4$ eV , and (△)$\phi_v = 3$ eV.

Above, only one wave vector is considered. This simple one dimensional free electron model cannot explain our experimental findings. Why this NM thickness dependent TMR strongly depends on the tip used in the experiments still remains puzzling. When different tips are used in the experiments, the tip-to-sample distance may be different due to the different sharpness of the tip. As addressed in previous section, the tunneling electrons with nonzero transverse momentum can be involved in tunneling when the tip to sample distance is small. For different transverse momentum, the longitudinal momentum in the nonmagnetic layer, which determines the period of oscillation caused by quantum well states, is different when different tips are used. This causes oscillations of the TMR with different periods and the sampling effect may decrease the TMR effect strongly.

Additionally, the different multi-component amorphous CoFeSiB tips may have slightly different bandstructures which match to the Au covered sample bandstructure differently. In this way, different dependence may be expected. However, this requires more complicated calculations which include all bandstructure effects.

In summary, we studied the Au coverage dependence of the TMR effect on Co(0001) surface by comparing the same domain structure with different Au coverage. The TMR does not vanish quickly in the presence of a nonmagnetic spacer. Several different behaviors of the dependence of the TMR effect on the Au coverage are observed with different tips. The different dependencies may be caused by the different sharpness of the tip or details in the bandstructure of the tip apex.

Chapter 5

Main conclusions and summary

This thesis is devoted to spin-polarized scanning tunneling microscopy (Sp-STM) which is a new magnetic imaging technique with nanometer resolution. In this chapter, a short summary of the main topics discussed in the thesis and the final conclusions will be given.

1. Details of the Sp-STM technique are described. It is based on the tunneling magneto resistance (TMR) effect between a ferromagnetic tip and a ferromagnetic sample. By periodically changing the magnetization of the soft magnetic tip with frequencies between 40-80 kHz and in combination with lock-in technique, topographic and spin-dependent parts of the tunneling current are separated and the topography and the magnetic structure of the sample are recorded simultaneously with high resolution. For the functionality of this method it is important to avoid mechanical vibrations and keep constant tip-to-sample distance during the switching process of the tip magnetization. For optimal performance, CoFeSiB amorphous tips with low coercive fields (50 μT), vanishing magnetostriction ($< 4 \times 10^{-8}$), low saturation magnetization (0.5 T) and low magnetization losses at frequencies up to 100 kHz were chosen. To minimize the influence of the stray field of the tip on the sample, electrochemical etching is used to prepare very sharp tips.

2. To verify the magnetic origin of the obtained contrast by Sp-STM, two proofs were given. First, with external magnetic field pulses, domain walls can be moved depending on the field direction while the topography remains unchanged. Second, the observed domain structure is similar to that obtained with standard magnetic imaging techniques, such as Kerr microscopy, SEMPA and MFM. The contrast mechanism of Sp-STM is discussed. It is evidenced that contributions of vibrations caused by the static magnetic force between the tip and the sample can be excluded. In a simple model, the lateral resolution of Sp-STM is estimated to be one order of magnitude better than that of MFM if the same tip is used.

3. Using Sp-STM, the closure domain structure of Co(0001) is studied with high resolution. Further insight in the fine structure of the complicated magnetic domain structure is obtained. Besides the well established wide surface domain walls, ultra narrow sections of the wall are found. The narrowest width of these walls is only 1.1 nm, which is more than an order of magnitude smaller than previously observed in bulk Co. Artifacts like dragging or modification of the wall by the magnetic tip can be excluded. In comparison with the full contrast between the fully perpendicular domains obtained in large area scan, the ultra narrow domain walls are found to have a rotation of magnetization from $-10.1 \pm 1.5^\circ$ to $+10.1 \pm 1.5^\circ$ with respect to the sample surface. This is in very good agreement with the surface closure domain model which predicts a surface closure domain wall width of 1.5 nm and a rotation of magnetization from -10° to $+10^\circ$ with respect to the sample surface. The observation of ultra narrow domain walls demonstrates that the lateral resolution of our technique is better than 1 nm.

4. The technique also allows to study locally the wall mobility and magnetic susceptibility. The magnetic susceptibility signal can be detected by the second harmonic of the modulation frequency. In the limit of soft magnetic materials or strong stray fields of the tip, this signal shows a contrast at domain wall locations. In combination with higher switching frequencies, the technique in principle allows to perform local studies of the switching behavior of individual magnetic nanostructures.

5. With Sp-STM, the barrier width dependent TMR effect through a vacuum barrier is investigated. By varying the tip-to-sample distance in a controlled way at constant bias voltage, the TMR as a function of the gap width is measured. At large tip-to-sample distances the TMR is constant. At distances below ≈ 4.5 Å, a drop of the TMR is found in contrast to the prediction of Jullière. The drop is correlated to the strong decrease of the local barrier height which is measured simultaneously. These observations give a quantitative verification of Slonczewski's model. The experimental finding also gives a guidance for magnetic imaging with Sp-STM. For the optimal performance of Sp-STM, it is necessary to work at large tip-to-sample distances to achieve a high value of magnetic contrast.

6. In contrast to planar junctions, in which a strong decrease of the TMR with bias voltage is found, the TMR through a vacuum barrier for a Co(0001) sample is independent on the bias voltages between -1.5 V and 1.5 V for large tip-sample separation (1 V, 1 nA). The experimental results show that the TMR drop with increasing bias voltage in planar junctions is not due to the magnon excitations. Our findings reveal that the mechanism is dominated by impurities. At smaller tip-sample separations (100 mV,1 nA), a strong decrease of the TMR at $\approx +0.2$ V is found. The effect could be caused by the involvement

of bulk states with $k_{\|} \neq 0$ or surface states with lower or opposite spin polarization for tunneling at small tip-to-sample distance.

7. The influence of a nonmagnetic Au layer deposited on top of Co(0001) on the TMR effect is discussed. Large values of TMR can still be found even if Co(0001) sample is covered by Au layer as thick as 3 nm. This suggests that Sp-STM could be used for studies of magnetic structures covered by protective layers. For different tips, different Au thickness dependent TMR effects are found. The effect may correlate with different tip-sample separations caused by the different sharpness of the tips or with different bandstructure matchings between the tip and the sample for different tips.

Bibliography

[1] A. Hubert, R. Schäfer, *Magnetic domains*, Springer-Verlag Berlin, (1998).

[2] H. Barkhausen, Phys. Z. **20**, 401 (1919).

[3] F. Bitter, Phys. Rev. **38**, 1903 (1931).

[4] H.J. Williams, F.G. Foster, E.A. Wood, Phys. Rev. **82**, 119 (1951).

[5] M.E. Hale, H.W. Fuller, H. Rubinstein, J. Appl. Phys. **30**, 789 (1959).

[6] K. Koike, K. Hayakawa, Appl. Phys. Lett. **45**, 585 (1984)

[7] H. Matsuyama, K. Koike, J. of Electron Microscopy **43**, 157 (1994).

[8] T. Duden, E. Bauer, Phys. Rev. B **59**, 468 (1999).

[9] G. Schönhense, J. of Phys. Condensed Matter, **11**, 9517 (1999).

[10] P. Fischer, T. Eimüller, G. Schütz, P. Guttmann, G. Schmah, K. Pruegl, G. Bayreuther, J. of Phys. D **31**, 649 (1998).

[11] L. Abelmann, S. Porthun, M. Haast, C. Lodder, A. Moser, M.E. Best, P.J.A. van Schendel, B. Stiefel, H.J. Hug, G.P. Heydon, A. Farley, S.R. Hoon, T. Pfaffelhuber, R. Proksch and K. Babcock, J. Magn. Magn. Mater. **190**, 135 (1998).

[12] W. Wernersdorf, E. Bonet Orozco, K. Hasselbach, A. Benoit, B. Barbara, N. Demoncy, A. Loiseau, H. Pascard, D. Mailly, Phys. Rev. Lett. **78**, 1791 (1997).

[13] C. Chappert, H. Bernas, J. Ferré, V. Kottler, J.P. Jamet, Y. Chen, E. Cambril. T. Devolder, F. Rousseaux, V. Mathet and H. Launois, Science **280**, 1919 (1998).

[14] T. Aign, P. Meyer, S. Lemerle, J.P. Jamet, J. Ferré, V. Mathet, C. Chappert, J. Gierak, C. Vieu, F. Rousseaux, H. Launois and H. Bernas, Phys. Rev. Lett. **81**, 5656 (1998).

[15] H. Brune, M. Giovannini, K. Bromann and K. Kern, Nature **394**, 451 (1998).

[16] O. Fruchart, M. Klaua, J. Barthel and J. Kirschner, Phys. Rev. Lett. **83**, 2769 (1999).

[17] G. Binnig, H. Rohrer, Ch. Gerber and E. Weibel, Physica(Utrecht) **107B+C**, 1335(1981), Proceedings of the Sixteenth International Conference on Low-Temperature physics, Los Angeles,19-25 August 1981 and Appl. Phys. Lett. **40**, 178 (1982).

[18] G. Binnig, H. Rohrer, Ch. Gerber and E. Weibel, Phys. Rev. Lett. **50**, 120 (1983).

[19] M. Johnson, and J. Clarke, J. Appl. Phys. **67**, 6141 (1990).

[20] R. Wiesendanger, H.J. Güntherodt, G. Güntherodt, R.J. Gambino and R. Ruf, Phys. Rev. Lett. **65**, 247 (1990).

[21] S.F. Alvarado and P. Renaud, Phys. Rev. Lett. **68**, 1387 (1992).

[22] M.W.J. Prins, R. Jansen and H. van Kempen, Phys. Rev. B **53**, 8105 (1996).

[23] Y. Suzuki, W. Nabhan and K. Tanaka, Appl. Phys. Lett. **71**, 3153 (1997).

[24] Y. Suzuki, W. Nabhan, R. Shinohara, K. Yamaguchi and T. Katayama, J. Magn. Magn. Mater. **198-199**, 540 (1999).

[25] H. Kodama, T. Uzumaki, M. Oshiki, K. Sueoka and K. Mukasa, J. Appl. Phys. **83**, 6831 (1998).

[26] M.W.J. Prins, R.H.M. Groeneveld, D.L. Abraham, H. van Kempen, H.W. van Kesteren, Appl. Phys. Lett. **66**,1141 (1995).

[27] P. Bruno, Phys. Rev. Lett. **79**, 4593 (1997).

[28] M. Bode, M. Getzlaff and R. Wiesendanger, Phys. Rev. Lett. **81**, 4256 (1998).

[29] W. Wulfhekel and J. Kirschner, Appl. Phys. Lett. **75**, 1944 (1999).

[30] M. Jullière, Phys. Lett. **54A**, 225 (1975).

[31] R. Jansen, R. Schad and H. van Kempen, J. Magn. Magn. Matter. **198-199** 668 (1999).

[32] O. Pietzsch, A. Kubetzka, M. Bode and R. Wiesendanger, Phys. Rev. Lett. **84**, 5212 (2000).

[33] M. Kleiber, M. Bode, R. Ravlić and R. Wiesendanger, Phys. Rev. Lett. **85**, 4606 (2000).

[34] J.C. Slonczewski, Phys. Rev. B. **39**, 6995 (1989).

[35] P.M. Tedrow and R. Merservey, Phys. Rev. Lett. **26**, 192 (1971).

[36] R. Merservey and P.M. Tedrow, Phys. Rev. Lett. **25**, 1270 (1970).

[37] I.I. Mazin, Phys. Rev. Lett. **83**, 1427 (1999).

[38] W. Gerlach and O. Stern, Zeitschrift für Physik, **9**, 349 (1922).

[39] D.A. Papaconstantopoulos, *Handbook of the band structure of elemental solids*, Plenum press, New York and London, (1986).

[40] T. Miyazaki and N. Tezuka, J. Magn. Magn. Matt. **139**, L231 (1995).

[41] M.B. Stearns, J. Magn. Magn. Mater. **5** 167 (1977).

[42] C. B. Duke, *Tunneling in solids*, Academic press, New York, (1969).

[43] W.H. Butler, X.-G. Zhang, X.D. Wang J. van Ek and J.M. MacLaren, J. Appl. Phys. **81**, 5518 (1997).

[44] J.M. MacLaren, X.-G. Zhang and W.H. Butler, Phys. Rev. B **56**, 11827 (1997).

[45] J. Mathon, Phys. Rev. B **56**, 11810 (1997).

[46] M. Sharma, S.X. Wang and J.H. Nickel, Phys. Rev. Lett. **82**, 616 (1999).

[47] J.M. De Teresa, A. Barthélémy, A. Fert, J.P. Contour, F. Montaigne and P. Seneor, Science **286**, 507 (1999).

[48] J.M. De Teresa, A. Barthélémy, A. Fert, J.P. Contour, R. Lyonnet, F. Montaigne, P. Seneor, and A. Vaurés, Phys. Rev. Lett. **82**, 4288 (1999).

[49] E. Yu Tsymbal and D.G. Pettifor, J. Phys. Condens. Matter. **9**, L411 (1997).

[50] A. Vedyayev, N. Ryzhanova, C. Lacroix, L. Giacomoni and B. Dieny, Europhys. Lett. **39**, 219 (1997).

[51] W.S. Zhang, B.Z. Li, X. Zhang and Y. Li, J. Appl. Phys. **83**, 5332 (1998).

[52] J.S. Moodera, J. Nowak, L.R. Kinder, P.M. Tedrow, R.J.M. van de Veerdonk, B. A. Smits, M. van Kampen, H.J.M. Swagten and W.J.M. de Jonge, Phys. Rev. Lett. **83**, 3029 (1999).

[53] J.S. Moodera and G. Mathon, J. Magn. Magn. Mater. **200**, 248 (1999) and references therein.

[54] Micro-STM, Omicron Vakuumphysik GmbH, Idsteiner Str. 78, 65232 Taunusstein, Germany.

[55] I. Ohnaka, Intl. J. Rapid Silidfn. **1**, 219 (1985).

[56] M. Vázquez, J. González and A. Hernando, J. Magn. Magn. Mater. **53**, 323 (1986).

[57] C. Gómez-Polo and M. Vázquez, J. Magn. Magn. Mater. **118**, 86 (1993).

[58] Prof. M. Vázquez, Instituto de Magnetismo Aplicado, Apartado de Correos 155, 28230 Las Rozas, Madrid, Spain.

[59] M. Fotino, Rev. Sci. Instrum. **64**, 159 (1993).

[60] See for instance, S. Chikazumi, *Physics of Ferromagnetism* Oxford University Press, New York (1997).

[61] E. Wetli, T.J. Kreutz, H. Schmid, T. Greber, J. Osterwalder and M. Hochstrasser, Surf. Sci. **402-404**, 551 (2000).

[62] W. Rave, E. Zueco, R. Schäfer and A Hubert, J. Magn. Magn. Mater. **177-181**, 1474 (1998).

[63] J. Unguris, M.R. Scheinfein, R.C. Celotta and D.T. Pierce, Appl. Phys. Lett. **55**, 2553 (1989).

[64] J. Tersoff and D. R. Hamann, Phys. Rev. Lett. **50**, 1998 (1983).

[65] Digital Instrument Support Note No. **257**, Rev. B (1999).

[66] S. Heinze, M. Bode, A. Kubetzke, O. Pietzsch, X. Nie, S. Blügel and R. Wiesendanger, Science **288**, 1805 (2000).

[67] A. Hubert and W. Rave, J. Magn. Magn. Mater. **196-197**, 325 (1999).

[68] G.F. Cabeza, P. Légaré, A. Sadki and N.J. Castellani, Surf. Sci. **457**, 121 (2000).

[69] P. Bruno, Phys. Rev. Lett. **83**, 2425 (1999).

[70] C. Kittel, Rev. Mod. Phys. **21**, 541 (1949).

[71] L. Néel, J. de Phys. **5**, 265 (1944).

[72] G. Bertotti, *Hysteresis in Magnetism*, Academic Press (1998).

[73] J.S. Moodera, L.R. Kinder, T.M. Wong and R. Meservey, Phys. Rev. Lett. **74**, 3273 (1995).

[74] Y. Lu, R.A. Altman, A. Marley, S.A. Rishton, P.L. Trouilloud, G. Xiao, W.J. Gallagher and S.S.P. Parkin, Appl. Phys. Lett. **70**, 2610 (1997).

[75] S. Yuasa, T. Sato, E. Tamura, Y. Suzuki, H. Yamamori, K. Ando and T. Katayama, Europhys. Lett. **52**, 344 (2000).

[76] P. LeClair, J.T. Hohlhepp, H.J.M. Swagten and W.J.M. de Jonge, Phys. Rev. Lett. **86**, 1066 (2001)

[77] J.M. MacLaren, X.-G. Zhang and W.H. Butler, Phys. Rev. B, **56**, 11827 (1997).

[78] H. Boeve, E. Girgis, J. Schelten, J. De Boeck and G. Borghs, Appl. Phys. lett. **76**, 1048 (2000).

[79] J. Zhang and R. M. White, J. Appl. Phys. **83** 6512 (1998).

[80] E. Yu. Tsymbal and D.G. Pettifor, J. Appl. Phys., **85**, 5801 (1999).

[81] Y. Kuk, *Scanning Tunneling Microscopy I*, edited by H.-J. Güntherodt and R. Wiesendanger, Springer-Verlag, Berlin, (1994).

[82] J.G. Simmons, J. Appl. Phys. **34**, 1793 (1963).

[83] J.K. Gimzewski and R. Möller, Phys. Rev. B **36**, 1284 (1987).

[84] N.D. Lang, Phys. Rev. B **36**, 8173 (1987); **37** 10395 (1988).

[85] Y. Kuk and P.J. Silverman, J. Vac. Sci. Technol. A **8**, 289 (1990).

[86] R. Meservey and P.M. Tedrow, Solid State Communications, **11**, 333 (1972).

[87] C.M. Fang, R.A. de Groot, M.M.J. Bischoff and H. van Kempen, Surf. Sci. **436**, L648 (1999).

[88] A.M. Bratkovsky, Phys. Rev. B **56**, 2344 (1997); JETP Lett. **65**, 452 (1997).

[89] A.M. Bratkovsky, Appl. Phys. Lett. **72**, 2334 (1998).

[90] S. Zhang, P.M. Levy, A.C. Marley and S.S.P. Parkin, Phys. Rev. Lett. **79**, 3744 (1997).

[91] J.S. Moodera, J. Nowak and R.J.M. van de Veerdonk, Phys. Rev. Lett. **80**, 2941 (1998).

[92] R. Jansen and J. S. Moodera, Phys. Rev. B **61**, 9047 (2000).

[93] See, for example, A. Yelon, in *Physics of Thin films*, edited by G. Hass, M.H. Francombe and R.W. Hoffman (Academic, New York, 1971), Vol. 6, p.205.

[94] J.S. Moodera and L.R. Kinder, J. Appl. Phys.,**79**, 4724 (1996).

[95] E.L. Wolf, in *Principles of Electron Tunneling Spectroscopy*, (Oxford university Press. London, 1985), ch. 8, for an extensive review.

[96] N. Tezuka and T. Miyazaki, Jpn. J. Appl. Phys. **37**, L218 (1998).

[97] M. Getzlaff, J. Bansmann, J. Braun and G. Schönhense J. Magn. Magn. Matt. **161**, 70 (1996).

[98] J.A. Stroscio, D.T. Pierce, A. Davies, R.J. Celotta and M. Weinert, Phys. Rev. Lett. **75**, 2960 (1995).

[99] J.S. Moodera, M.E. Taylor and R. Meservey, Phys. Rev. B. **40**, 11980 (1989).

[100] A. Vedyayev, N. Ryzhanova, C. Lacroix, L. Giacomoni and B. Dieny, Europhys. Lett. **39**, 219 (1997).

[101] W.S. Zhang, B.Z. Li and Y. Li, Phys. Rev. B **58**, 14959 (1998).

[102] J.J. Sun and P.P. Freitas, J. Appl. Phys. **85**, 5264 (1999).

[103] S.S.P. Parkin, U.S. Patent No. 5764567 (1998).

[104] S. Zhang and P.M. Levy, Phys. Rev. Lett. **81**, 5660 (1998).

[105] J. Mathon and A. Umerski, Phys. Rev. B **60**, 1117 (1999).

[106] P. LeClair, H.J.M. Swagten, J.T. Kohlhepp, R.J.M. van de Veerdonk and W.J.M. de Jonge, Phys. Rev. Lett. **84**, 2933 (2000).

[107] CRC-handbook of Chemistry and Physics, 74th ed., CRC Press, Boca Raton, 1993-1994.

[108] S. Pick and H. Dreyssé, Surf. Sci. **474**, 64 (2001).

[109] J. Corno, M. Galtier, D. Renard, J.P. Renard and F. Trigui, Eur. Phys. J. B **10**, 223 (1999).

[110] M.K. Weilmeier, W.H. Rippard and R.A. Buhrman, Phys. Rev. B, **59**, R2521 (1999).

[111] C. Kittel, *Introduction to Solid State Physics* (John Wiley & Sons, New York, 1986), 6th ed.

[112] L.D. Landau and E.M. Lifshitz, *Quantum Mechanics (Non-relativistic Theory)*, Pergamon Press, 1999, 3rd ed.

Appendix A

Component resolved Kerr effect

Besides the work mentioned in this thesis, I also spent 9 months working in developing a new technique, i.e., the component resolved Kerr effect.

In the spin-reorientation transition (SRT) when the magnetization changes between perpendicular and in-plane orientations at least two components of magnetization can be involved in the reversal process due to a field sweep. This causes a mixing of polar and longitudinal Kerr signal. This kind of mixing is also commonly found when the external field is not strictly aligned. As the longitudinal and polar Kerr signals are mixed with a field-dependent strength, quantitative data analysis is difficult. To overcome this problem, we developed a new experimental method to deconvolute the polar and longitudinal signals by two measurements of the Kerr signal in reversed geometries. By including the transverse component, the method is expanded to 3-D studies of magnetization by simple Kerr measurements, i.e., the component resolved Kerr effect. By using four different geometries, related to each other by mirror symmetry and a 90° rotation, all the polar, longitudinal and transverse components of the magnetization can be obtained. The technique has been used to study the spin-reorientation transition in Co/Au(111). With thickness within the SRT region we find hysteresis loops with non-vanishing remanence in all three components when a field is applied within the film plane. A vertical field, however, drives the same film into a single domain state exhibiting full remanence. The fact that remanence is found in all magnetization components, and full remanence is obtained in a vertical field, rules out that the transition proceeds via a state of canting of magnetization and indicates that it proceeds via a state of coexisting phases. As the details of the technique has been published, I attached the original publication in this thesis as reference.

ELSEVIER

Journal of Magnetism and Magnetic Materials 212 (2000) L5–L11

Journal of magnetism and magnetic materials

www.elsevier.com/locate/jmmm

Letter to the Editor

Experimental method for separating longitudinal and polar Kerr signals

H.F. Ding, S. Pütter, H.P. Oepen*, J. Kirschner

Max-Planck-Institut für Mikrosturphysik, Weinberg 2, 06120 Halle, Germany

Received 18 August 1999; received in revised form 10 November 1999

Abstract

A new procedure is presented which can be easily applied to separate longitudinal and polar Kerr signals. The method is advantageous particularly in systems where in-plane and out-of-plane states of magnetization are involved in the reversal process. The feasibility of the method is demonstrated at the spin-reorientation transition in Co/Au(1 1 1) films. © 2000 Elsevier Science B.V. All rights reserved.

PACS: 78.20.L; 33.55.F; 78.20.J

Keywords: Magneto-optical effect; Kerr effect; Spin-reorientation transition; Magnetic hysteresis; Thin films

1. Introduction

Moog and Bader have demonstrated that the magneto-optical Kerr effect (MOKE) is very well suited for the study of thin film magnetism [1]. Since this pioneering experiment MOKE has become a very important technique for the investigation of magnetism in monolayer films [2,3]. Three main experimental geometries are known, i.e. the polar, longitudinal and transverse Kerr effects. They are classified with respect to the orientation of the magnetization to the light scattering plane. Usually, the polar Kerr signal is one order of magnitude larger than the longitudinal signal [3]. Hence, a small perpendicular component can cause considerable polar contribution in the Kerr signal in longitudinal geometry. Particularly, in the spin-reorientation transition when the magnetization changes between perpendicular and in-plane orientations at least two components of magnetization can be involved in the reversal process due to a field sweep. The mixing of the two components will get even worse if the external field is slightly misaligned. Then, within the spin-reorientation the longitudinal, and polar Kerr signals are mixed with a field-dependent strength. This makes the quantitative data analysis difficult. Hysteresis loops revealing such a mixture have only qualitatively been discussed in Ref. [4]. To overcome this problem Yang and Scheinfein suggested to measure the exact polar signal in normal incidence geometry [5]. Up to now the deconvolution of mixed longitudinal and polar signals has not been addressed. In this paper we propose a new method to separate

* Corresponding author. Tel.: + 49-345-5582624; fax: + 49-345-5511223.

E-mail address: oepen@mpi-halle.mpg.de (H.P. Oepen)

0304-8853/00/$ - see front matter © 2000 Elsevier Science B.V. All rights reserved.
PII: S0304-8853(99)00790-8

longitudinal and polar Kerr signals and demonstrate the feasibility of the proposed procedure.

2. Principle

In first-order approximation the Kerr signal is a function of the direction cosine between the propagation vector of the incident light $\boldsymbol{k}$ and the direction of the magnetization M, i.e. $\boldsymbol{k}\cdot\boldsymbol{M}$ [3].[1] In polar geometry the angles between k and M are exactly the same for inverted geometries (see Fig. 1a). Hence, the polar Kerr signal is an even function of the incident angle. Exactly the same hysteresis loops will be obtained in both geometries. On the contrary (see Fig. 1b), in the longitudinal geometry the two angles between $\boldsymbol{k}$ and $\boldsymbol{M}$ are supplementary angles in the reversed experiments. This means that the longitudinal signal is an odd function of the incident angle. It will change sign if the incident and scattered beams are exchanged. These basic symmetry properties are used to disentangle the mixed Kerr signals which may occur with a general geometry (neither strictly polar nor strictly longitudinal).

A phenomenological description of the magneto-optical Kerr effect can be given by utilizing the Fresnel coefficients of reflectivity. The Fresnel reflection coefficients r_{ps}, r_{ss} are given in Table 1 [5–8]. The first and the second subscripts indicate the polarization of the scattered light and the incident light, respectively. For the sake of simplicity a single interface nonmagnetic/magnetic has been assumed for deducing the formulae corresponding to a semi-infinite sample (bulk). For ultrathin films the effect of the substrate has to be considered. Similar formulae with the same characteristic features are obtained in first-order approximation [5–8]. The quotient of the coefficients r_{ps}, r_{ss} is the Kerr signal. The real/imaginary part represents the Kerr rotation/ellipticity, respectively. For s-polarized incident light the ratio of the longitudinal signal to the polar signal is proportional to $-\tan\theta_1$ (the ratio is $\tan\theta_1$ for p-polarized light). It is an odd function of the incident angle θ_0. This proves that both geometries are of different symmetry with respect to θ_0. Utilizing the reflection coefficients from Table 1 we can calculate the Kerr signals which reveal the above-mentioned symmetries. Particularly, for s-polarized light one can derive from Table 1 the ellipticities for $\pm\theta_0$:

$$\varepsilon^{\pm\theta_0} = \varepsilon^{\mathrm{p}} \pm \varepsilon^{\mathrm{L}} \tag{1}$$

with $\varepsilon^{+\theta_0}$, $\varepsilon^{-\theta_0}$ the Kerr ellipticities for the respective angles of incidence, and ε^{p}, ε^{L} the ellipticities for the polar and longitudinal Kerr effects.

Hence, by two measurements of the Kerr signal in reversed geometries, one can obtain the sum and difference of the polar and longitudinal Kerr signals, respectively. This allows one to determine the individual contributions: by taking the sum of both signals one obtains twice the polar Kerr ellipticity, by taking the difference one obtains twice the longitudinal Kerr ellipticity. This procedure is thus very well suited to separate the response of the longitudinal and polar Kerr effects.

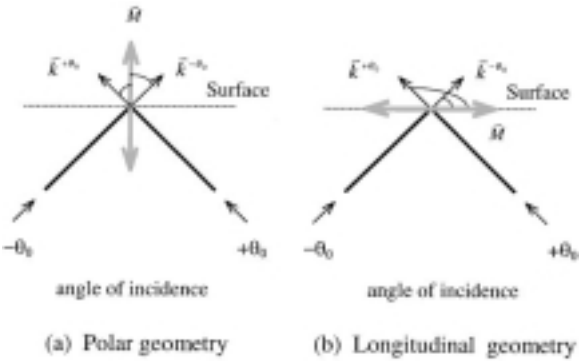

Fig. 1. Sketch of the experimental set-up for the polar and longitudinal Kerr effects. (a) In polar geometry the angles between k and M are exactly the same and $\boldsymbol{k}\cdot\boldsymbol{M}$ is equal for $\pm\theta_0$. (b) In longitudinal geometry the angles between $\boldsymbol{k}$ and $\boldsymbol{M}$ are supplementary angles for the light coming from the right- or left-hand side and $\boldsymbol{k}\cdot\boldsymbol{M}$ changes sign when the direction of incidence is reversed.

[1] In the classical model, Kerr effect can be understood as the change of the electric field vector by the Lorentz force $\boldsymbol{f} = \boldsymbol{E}\times\boldsymbol{M}$ due to the magnetization of material. The contribution to the Kerr signal is proportional to $\cos(\boldsymbol{k}\cdot\boldsymbol{M})$.

Table 1
The Fresnel coefficients for s-polarized light for a single nonmagnetic/magnetic interface. The complex index of refraction for both materials are n_0 and n_1. θ_0 and θ_1 are the angles of incidence and reflection of the light with respect to the interface normal

	r_{ss}	r_{ps}
Polar	$\frac{n_0 \cos\theta_0 - n_1 \cos\theta_1}{n_0 \cos\theta_0 + n_1 \cos\theta_1}$	$\frac{\mathrm{i}n_0 n_1 \cos\theta_0 \, Q}{(n_1 \cos\theta_0 + n_0 \cos\theta_1)(n_0 \cos\theta_0 + n_1 \cos\theta_1)}$
Longitudinal	$\frac{n_0 \cos\theta_0 - n_1 \cos\theta_1}{n_0 \cos\theta_0 + n_1 \cos\theta_1}$	$\frac{-\mathrm{i}n_0 n_1 \cos\theta_0 \tan\theta_1 \, Q}{(n_1 \cos\theta_0 + n_0 \cos\theta_1)(n_0 \cos\theta_0 + n_1 \cos\theta_1)}$
Transverse	$\frac{n_0 \cos\theta_0 - n_1 \cos\theta_1}{n_0 \cos\theta_0 + n_1 \cos\theta_1}$	0

3. Experiment

Co on Au(1 1 1) has been chosen to demonstrate the feasibility of the above-sketched method. Due to the spin-reorientation transition a mixing of different magnetization states can appear [9]. The Co films were grown at room temperature under UHV conditions by means of e-beam evaporation onto an Au(1 1 1) single crystal. The rate of deposition was 0.4 ML/min. The Au(1 1 1) crystal was cleaned by Ar ion etching and annealing at 900 K for half an hour. The reconstruction of Au was clearly seen in the low-energy electron diffraction (LEED) pattern. After growth, the film has been annealed at 510 K for 10 min in order to stabilize the magnetic properties, stop the Au diffusion and smooth the sample surface [10]. The thicknesses were tuned to fit the region close to the spin-reorientation transition.

S-polarized light was used to minimize signals caused by the transverse Kerr effect (see Table 1). Transverse signals can be caused by some small remnants of p-polarization. The amount of p-polarization can be estimated from optical calibration measurements. The extinction ratios have been determined in crossed polarizer geometry to investigate the effects of the windows. Values of 10^{-5} and 10^{-6} are found for the extinction ratio with and without windows, respectively.[2] The values are quite low for the reflection at a metal surface which indicates that the state of polarization must be very close to s-polarization.[3] If we assume that the extinction of 10^{-6} is solely determined by a slight misalignment of the polarization of the incoming light (worst case) we will obtain 1.5 mrad as the tilting angle. Due to birefringence of the windows the light is elliptically polarized and the extinction ratio is worse when windows are implemented. If we assign, in the same way as above, the increase in intensity due to birefringence to misalignment of the incident light we will get 3.5 mrad as the angle of deviation. For the magnetic measurements a quarter-wavelength plate is implemented to eliminate the window effects and to increase the sensitivity [12]. With the quarter wavelength plate again an extinction value of 10^{-6} is obtained. In spite of that high extinction ratio a total misalignment of 5 mrad, the sum of both uncertainties, is assumed as a conservative estimate. We have calculated the amount of ellipticity that is created due to the transverse Kerr effect caused by the estimated misalignment. Utilizing the formulae given by Zak and co-workers [13], the Voigt constant from Ref. [14] and tabulated values for the index of refraction [15] we find for our experimental settings 2.2% of longitudinal signal in saturation as an

[2] Glan-Thompson polarizer are used with an extinction ratio of 10^{-7}.

[3] In textbooks it is shown that only for s- or p-polarization a high extinction ratio will be found when the light is reflected at a metal surface and the angle of incidence is not too close to 0° or 90° (see Ref. [11]).

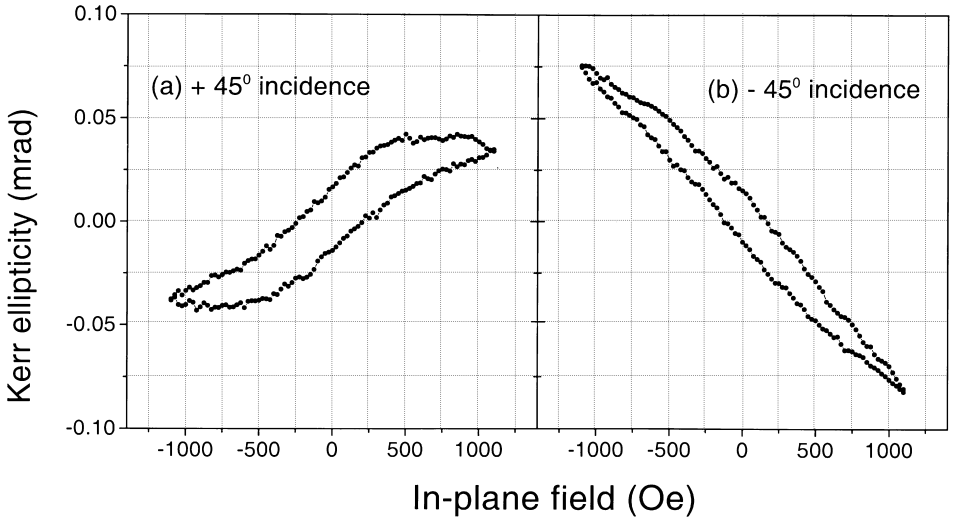

Fig. 2. Kerr ellipticities for a Co film on Au(1 1 1) at a thickness close to the spin-reorientation transition. The field is applied within the film and the light scattering plane. S-polarized light is impinging along $+45^\circ$ (a) and -45° (b), respectively.

upper limit for the uncertainty.[4] It should be pointed out that after exchanging the two optical parts the same value of extinction within a factor of 1.5 is achieved.

In order to keep the light spot at the same place on the sample, an additional laser has been used to mark the position while the light source and detector are interchanged. The positions where the light goes through the windows have also been marked. The optics, i.e. laser and polarizer as well as the analyzer components, are fixed to separate rigid supports which are tightly attached to the windows of the UHV chamber. The combination of marking the positions and the geometry of the experiment reduces the uncertainty of the incident angle on reversing the geometry to less than 1°. As the sensitivity of the polar and longitudinal Kerr effect is constant around 45° such small changes in the angle of incidence can be neglected [13].

4. Experimental results

The hysteresis loops obtained for an angle of incidence of $\pm 45^\circ$ are plotted in Figs. 2a and b. The magnetic field was applied parallel to the film plane and the scattering plane of the light. A slight misorientation of $1–2^\circ$ with respect to the surface plane could not be eliminated. The signals in the two measurements are quite different, depending on the relative orientation of the light and the external field. The two loops are inverted and the shape and magnitude are strongly different. If the magnetization was solely in the plane a pure longitudinal Kerr signal with two identical but reversed loops would be found.

Following the procedure sketched above we have calculated the point-by-point difference and sum of the two curves. The results, divided by two, are

[4] Following Zak, the Fresnel coefficients r_{pp}, r_{ss} and r_{ps}, in longitudinal geometry, and the change of reflectivity Δr_{pp} in transverse geometry at 2 eV were calculated for an angle of incidence of 45°. The sample is 5 ML Co/Au which is very close to the film thickness in the measurement. We obtained 139 μrad ellipticity for s-polarized light in longitudinal geometry. Assuming $\alpha = 5$ mrad as the angle of deviation from pure s-polarization and $\delta = 8.7$ mrad as the orientation of the analyzer we can calculate the ellipticity that is caused by the small amount of p-polarization. From the imaginary part of $\Delta r_{pp}(\delta + \alpha) \sin\alpha \cos\delta / (r_{ss} \cos\alpha \sin\delta + r_{pp} \sin\alpha \cos\delta)$ we obtain 3 μrad.

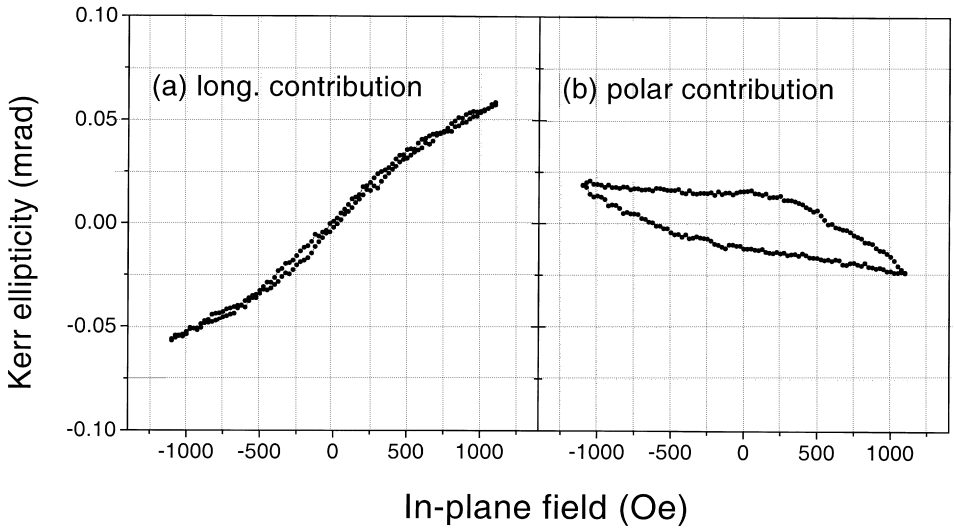

Fig. 3. Longitudinal and polar Kerr signals calculated from the data given in Fig. 2. (a) is $\frac{1}{2}$ of the difference and (b) is $\frac{1}{2}$ of the sum of the curves in Fig. 2. (For more details see text.)

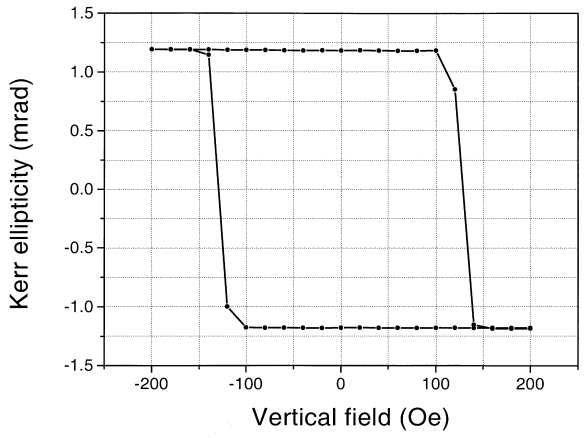

Fig. 4. Hysteresis loop obtained in a vertical field with the same film used for taking the data shown in Fig. 3. The angle of incidence is 15°.

shown in Figs. 3a (difference) and b (sum) which are the hystereses of the in-plane and polar Kerr signals, respectively. We have investigated the thickness dependence of the longitudinal signal in saturation for in-plane magnetization. From that dependence we extrapolate to the film thickness under investigation (roughly 5 ML). A Kerr ellipticity of 140 $\pm$ 5 μrad for the longitudinal signal in saturation is determined from this extrapolation, which is close the calculated value of 139 μrad (see foot note 4). Taking the above uncertainty analysis we obtain a maximal transverse signal of 3 μrad. Hence, Fig. 3a gives the longitudinal Kerr signal, i.e. the in-plane magnetization component along the field direction, exhibiting a hard axis loop. The vertical component (Fig. 3b), however shows a hysteresis. Apparently the field that is effective along the surface normal cannot saturate the film. Comparing Figs. 2 and 3 it is obvious that a polar signal that is caused by a slight misalignment of the field can change the hysteresis obtained in a longitudinal Kerr set-up. This demonstrates that it is necessary to separate the two Kerr contributions, particularly when performing experiments with systems close to a spin-reorientation transition. The polar loop shown in Fig. 4 was achieved when a field in the vertical direction was applied. The magnetization curve exhibits a square-like easy axis loop with a small coercivity (about 125 Oe) which proves that the easy axis is perpendicular to the film plane. The full signal is about 50 times larger than in Fig. 3b which demonstrates that the plot Fig. 3b is a minor loop.

In the longitudinal geometry the Kerr signal is expected to reverse sign when the experiment is

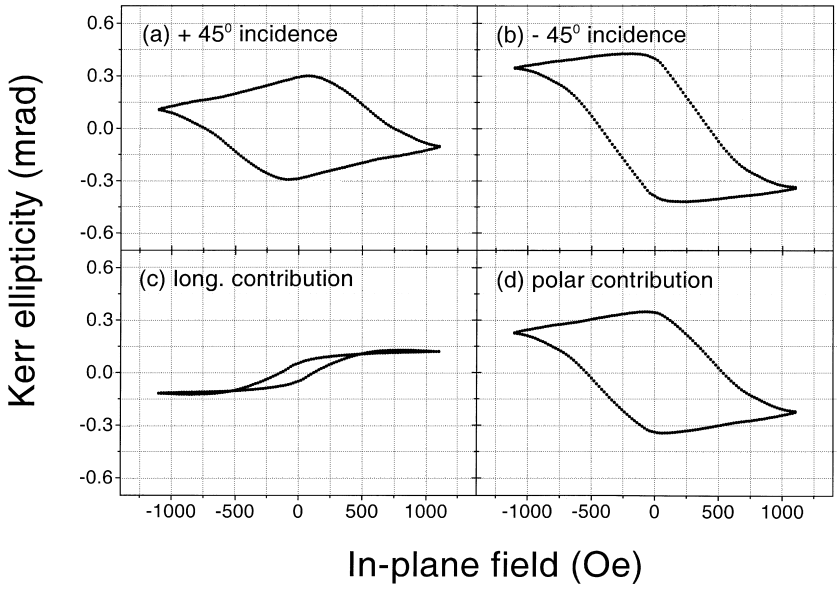

Fig. 5. Kerr ellipticities for a Co film on Au(1 1 1) at a thickness closer to the spin-reorientation transition than in the case of Fig. 3. The field is applied within the light scattering plane and the film plane. S-polarized light is impinging along $+45^{\circ}$ (a) and -45° (b). The calculated Kerr signals are the longitudinal contribution (c) and the polar contribution (d).

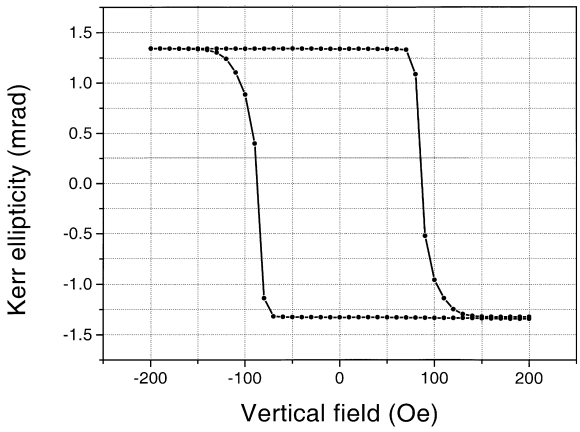

Fig. 6. Hysteresis loop obtained in a vertical field. The same film was used as for Fig. 5. The angle of incidence is 15°.

performed in the inverted geometry. In Fig. 5 the hysteresis for a Co thickness closer to the spin-reorientation transition is plotted. Both the signals with positive and negative angles of incidence show the same sign. This can be attributed to the large influence of the polar contribution. The magnetic perpendicular anisotropy is smaller in this case than before because the thickness is closer to the spin-reorientation value. Therefore, the misorientation of the external field causes a stronger signal in the polar Kerr effect, which in this case even dominates the total signal in a and b. The deconvoluted loops (c and d) show remanence in both in-plane and vertical directions while the longitudinal hysteresis again shows the correct sign. In pure vertical field a clearly easy axis appears in polar geometry (Fig. 6). More details will be given in a forthcoming paper [16].

Acknowledgements

The authors acknowledge discussions with Dr. R. Vollmer.

References

[1] E.R. Moog, S.D. Bader, Superlattices Microstruct. 1 (1985) 543.

[2] S.D. Bader, J.L. Erskine, in: J.A.C. Bland, B. Heinrich, (Eds.), Ultrathin Magnetic Structures, Vol. II, Springer, Berlin, 1994, ch. 4, and references therein.
[3] S.D. Bader, J. Magn. Magn. Mater. 100 (1991) 440, and references therein.
[4] Z.Q. Qiu, J. Pearson, S.D. Bader, Phys. Rev. Lett. 70 (1993) 1006.
[5] Z.J. Yang, M.R. Scheinfein, J. Appl. Phys. 74 (1993) 6810.
[6] M.J. Freiser, IEEE Trans. Magn. Mag-4 (1968) 152.
[7] J. Zak, E.R. Moog, C. Liu, S.D. Bader, J. Appl. Phys. 68 (1990) 4203.
[8] C. You, S. Shin, Appl. Phys. Lett. 69 (1996) 1315.
[9] H.P. Oepen, M. Speckmann, Y.T. Millev, J. Kirschner Phys. Rev. B. 55 (1997) 2752. H.P. Oepen, Y.T. Millev, J. Kirschner, J. Appl. Phys. 81 (1997) 5044.
[10] M. Speckmann, H.P. Oepen, H. Ibach, Phys. Rev. Lett. 75 (1995) 2035.
[11] See for example: M. Born, E. Wolf, Principles of Optics, Pergamon Press, Oxford, 1993, p. 615.
[12] E.R. Moog, C. Liu, S.D. Bader, J. Zak, Phys. Rev. B. 39 (1989) 6949.
[13] J. Zak, E.R. Moog, C. Liu, S.D. Bader, Phys. Rev. B. 43 (1991) 6423.
[14] R.M. Osgood III, K.T. Riggs, A.E. Johnson, J.E. Mattson, C.H. Sowers, S.D. Bader, Phys. Rev. B. 56 (1997) 2627.
[15] CRC Handbook of Chemistry and Physics, 74th ed., CRC Press, Boca Raton, 1993–1994.
[16] H.F. Ding, S. Pütter, H.P. Oepen, J. Kirschner, to be submitted.

Spin-reorientation transition in thin films studied by the component-resolved Kerr effect

H. F. Ding, S. Pütter,* H. P. Oepen,*,† and J. Kirschner
Max-Planck Institut für Mikrostrukturphysik, Weinberg 2, 06120 Halle, Germany
(Received 24 July 2000; published 14 March 2001)

We present a method to separate the longitudinal, polar, and equatorial magnetization components that may contribute to a mixed magneto-optical Kerr-effect signal and demonstrate how the spin-reorientation transition (SRT) can be investigated by means of simple Kerr magnetometry. In a Co/Au(111) film with thickness within the SRT region we find hysteresis loops with nonvanishing remanence in all three components when a field is applied within the film plane. A vertical field, however, drives the same film into a single domain state exhibiting full remanence. The fact that remanence is found in all magnetization components, and full remanence is obtained in a vertical field, rules out that the transition proceeds via a state of canting of magnetization and indicates that it proceeds via a state of coexisting phases.

DOI: 10.1103/PhysRevB.63.134425 PACS number(s): 75.70.Ak, 78.20.Ls, 33.55.Fi, 78.20.Jq

I. INTRODUCTION

Conventional methods for obtaining magnetic hysteresis loops, e.g., vibrating sample magnetometry and superconducting quantum interference device susceptometry are commonly used to detect a single component of magnetization parallel to the direction of the external field. A single hysteresis curve obtained with these methods, however, provides only a limited amount of information. Additional information can be produced by rotating the sample in an applied field.[1] A more fundamental method for investigating the magnetization process entails measuring the three components of the magnetization. Some work along this line demonstrated its power 40 years ago. The instruments, however, were rather complex to construct.[2,3]

The magneto-optical Kerr effect (MOKE) has become an important technique for the investigation of surface and ultrathin-film magnetism.[4–6] It has been successfully applied to measure the two orthogonal in-plane components of the magnetization by means of an in-plane vectorial MOKE technique.[7–11] This technique was also used to identify the orientation of in-plane domains in Kerr microscopy.[9,10] Yang and Scheinfein suggested measuring the pure polar signal in a normal-incidence geometry.[12] It appears possible to obtain the individual magnetization components by applying these methods. The very existence of a polar signal, however, prevents the correct measurement of the in-plane components due to the fact that these signals are suppressed by the much stronger polar signal. The mixing of polar and longitudinal signals has been qualitatively discussed in the literature.[13] Berger and Pufall presented a promising technique, i.e., generalized magneto-optical ellipsometry,[14] which allows to determine the orientation of the in-plane magnetization. The authors pointed out that the method is also useful to separate the mixed Kerr signal of out-of-plane and in-plane magnetization. This method, however, is quite involved.

A new method of separating the longitudinal and polar Kerr signal was presented recently.[15] In the present paper this technique is expanded to obtain the information of all three orthogonal magnetization components [three dimensional (3D) MOKE]. We use this method to study the spin-reorientation transition in Co films on Au(111).

In Co/Au(111) a thickness-dependent spin reorientation has been found.[16,17] The competition between surface anisotropy and magnetostatic energy forces the magnetization to flip from perpendicular to in-plane orientation with increasing thickness. The magnetization follows the sweep of an external field applied along the easy axis when the thickness is below or beyond the spin-reorientation transition. Within the spin-reorientation transition the magnetization orientation in a field is still unclear and the subject of ongoing debate. By means of the 3D-MOKE technique we can identify nonvanishing signals in all three components within the thickness span of the SRT when the field is in plane. Applying a field in the vertical direction drives the film into a single domain state with full remanence. This finding indicates that the spin-reorientation transition of Co/Au(111) proceeds via a state of coexisting phases, not via a state of continuous magnetization canting.

In the next section we will summarize the principle of the method and give a detailed description of the experimental verification in the third section. Hysteresis loops obtained with films at three representative thicknesses, i.e., below, beyond, and within the SRT will be discussed in the fourth section.

II. PRINCIPLE

In the framework of the linear Kerr effect, MOKE is classified with respect to the orientation of the magnetization and the light-scattering plane. In the polar Kerr effect the magnetization is normal to the reflecting surface. In the longitudinal/transverse Kerr effect the magnetization is parallel to the sample surface and within/perpendicular to the light-scattering plane, respectively. If the magnetization is oriented in an arbitrary direction the Kerr signal can, in principle, be split into these three basic configurations.

It should be pointed out that the different MOKE geometries are not related to the direction of the applied magnetic field. Particularly in the magnetization reversal process the magnetization will not be strictly fixed to the field direction or along the easy axis. In such a situation, the Kerr signal is a mixture of different Kerr effects. Usually, the mixed Kerr signal gives very complicated hysteresis loops due to the

 ©2001 The American Physical Society

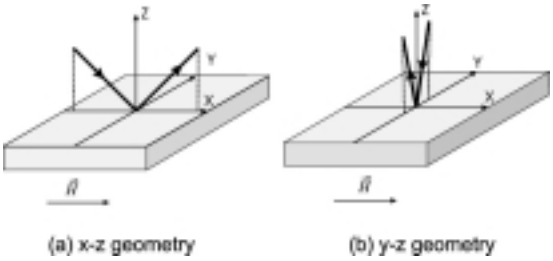

FIG. 1. Experimental setup. (a) The angle of incidence is 45°. The scattering plane is spanned by the direction of the magnetic field (x axis) and the surface normal (z axis). (b) The plane of incidence is perpendicular to the field direction (angle of incidence 9°).

different strength of the individual contributions.[13,15,18–21] The best way to obtain the pure components along different directions is to select a geometry where one component does not contribute and separate the remaining components. The third component can be achieved through a second similar measurement.

In a simplified classical model the linear Kerr effect can be understood as the change of the electric-field vector of the light due to Lorentz force caused by the magnetization of the material.[19] Hence, no Kerr signal is found when the magnetization is parallel to the electric field of the light. This situation appears for the transverse Kerr effect with *s*-polarized light. Vice versa, it means that by using *s*-polarized light the transverse Kerr effect can be eliminated and only polar and longitudinal components remain, which can be separated in the following way.

Recently, a procedure that can be used to separate the longitudinal and polar Kerr signals has been presented.[15] As the polar Kerr signal is an even function and the longitudinal signal is an odd function of the incident angle, the two contributions can be separated. When *s*-polarized light is impinging under a positive angle,[22] the sum of polar and longitudinal contributions is measured; while reversing the optical geometry with respect to the surface normal the difference of both is obtained, i.e.,

$$\varepsilon^{\pm\theta} = \varepsilon^{P} \pm \varepsilon^{L}, \tag{1}$$

with $\varepsilon^{\pm\theta}$ the Kerr ellipticities for the respective angles of incidence, and ε^{P} and ε^{L} the ellipticities for the polar and longitudinal Kerr effects. Hence, by two measurements in reversed geometries one can separate the longitudinal and polar Kerr signals. We will explain in the following how the third component of the magnetization can be determined.

For the sake of simplicity we introduce a frame of reference. As shown in Fig. 1, we define the surface normal as the z direction. The x and y directions are lying within the film plane. The field is acting along the x axis. When the xz plane is the light-scattering plane (''x-z geometry'') the magnetization component along the y direction (M_y) will not contribute to the Kerr signal when using *s*-polarized light. Hence, this MOKE setup is only sensitive to M_x and M_z, which causes a longitudinal and polar signal, respectively. The signals can be separated by two measurements in reversed geometries as explained above.

Rotating the MOKE optics by 90° about the surface normal (alternatively one may rotate the sample and the applied field by 90°) the yz plane becomes the scattering plane while the field is still oriented along the x direction [''y-z geometry'' in Fig. 1(b)]. In this geometry the MOKE setup is sensitive to M_y and M_z giving a longitudinal and polar signal, respectively. Applying the same technique the component M_y is obtained while the component M_z is measured redundantly. Thus, by using four different geometries, related to each other by mirror symmetry and a 90° rotation, all three components are obtained. The redundant measurement of M_z serves as an important consistency check.

III. EXPERIMENTS

The Co films were grown on a Au(111) single crystal under UHV conditions by means of *e*-beam evaporation at room temperature. Utilizing medium-energy electron-diffraction intensity oscillations the evaporation rate was calibrated with an error margin of 5%. The typical rate of deposition was 0.4 ML/min. The gold crystal was cleaned by 1-kV-Ar ion etching at a 30° angle of incidence and annealing at 900 K for half an hour. The $23\times\sqrt{3}$ reconstruction of Au (Refs. 23,24) was clearly seen in the low-energy electron-diffraction pattern. After growth the films have been annealed at 510 K for 10 min in order to stabilize the magnetic properties, stop the Au diffusion, and smooth the sample surface.[25] Co films with different thicknesses were grown to cover the full range of the spin-reorientation transition. We will discuss in the following the magnetic properties of three representative thicknesses, i.e., below, within, and beyond the spin-reorientation transition.

For the measurement of the magnetic properties, we use two optical setups with perpendicular scattering planes as shown in Fig. 1. The external field was applied along the x direction.[26] The ''x-z geometry'' is sensitive to M_x and M_z while the other one, i.e., ''y-z geometry'' is sensitive to M_y and M_z. Due to experimental restrictions the angle of incidence for the ''x-z geometry'' is 45° and for ''y-z geometry'' it is 9°. In a third MOKE geometry the polar Kerr effect is obtained under 15° in a vertical field along z.

S-polarized light was used in all MOKE setups to minimize the signals caused by the transverse Kerr effect. Quarter-wavelength plates have been incorporated in the optics to minimize the window effects and thus increase the sensitivity.[27] Due to the 90° phase shift induced by the quarter-wavelength plate the Kerr ellipticity instead of the Kerr rotation is obtained.[28]

The laser spots of both MOKE setups were kept on the same position (uncertainty was less than 20% of the laser-spot diameter) on the sample to reduce the uncertainty of the alignment when reversing geometry, i.e., interchanging the light source and the detector. The positions where the light passes through the windows have been marked. The optics, i.e., laser and polarizer as well as the analyzer components, were fixed to two rigid supports that were tightly clamped to the windows of the UHV chamber. The combination of

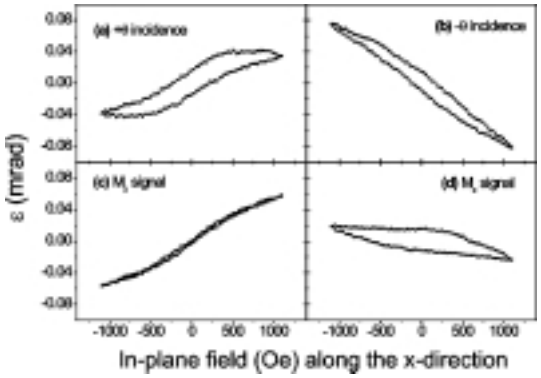

FIG. 2. Hysteresis loops at a thickness just before the spin-reorientation transition (5.0 ± 0.3 ML) obtained in the ''x-z geometry.'' (a) and (b) are hysteresis loops obtained at a $\pm45°$ angle of incidence. (c) and (d) are the pure components along the x and z directions. They are deconvoluted from (a) and (b).

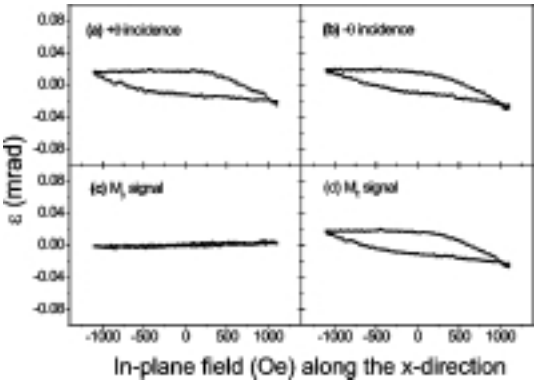

FIG. 3. Hysteresis loops obtained in the ''y-z geometry'' with the same film as in Fig. 2. The hysteresis loops in (a) and (b) are obtained at a $\pm9°$ angle of incidence. (c) and (d) are the pure components along the y and z directions. They are deconvoluted from (a) and (b).

marking the positions on the windows and the rigid support for the optics reduces the uncertainty in the angle of incidence to less than 1° on reversing the geometry. As the sensitivity of the polar and longitudinal Kerr effect is only weakly dependent on the angle around 45° small changes in the angle of incidence can be neglected in the ''x-z geometry.''[20]

In the ''y-z geometry,'' a larger uncertainty of the longitudinal signal is expected due to the uncertainty of the angle on reversing the geometry, as at 9° a stronger angle dependence of the Kerr signal is effective. Utilizing the formulas given by Zak and co-workers,[20] the Voigt constant from Ref. 29, and tabulated values for the index of refraction[30] we can estimate an uncertainty of about 10% for the longitudinal signal for a 1° deviation of the angle of incidence. Small changes in the angle of incidence must not be considered for the polar signal since the sensitivity is constant around 9°.

Due to the different angles of incidence we cannot directly compare the magnitude of the longitudinal signals. We have calculated the angle-dependent Kerr ellipticity of the longitudinal signal using the method mentioned above. We find that the sensitivity of the longitudinal signal at 45° is four times larger than that at 9°. As the Kerr signal is linear with the film thickness in the ultrathin-film approximation,[20] we use this ratio to compare the longitudinal signals obtained in both MOKE setups.[31]

IV. EXPERIMENTAL RESULTS

Figs. 2(a) and (b) show the hysteresis loops obtained in the ''x-z geometry'' for opposite angles of incidence. The thickness of 5.0 ± 0.3 ML is chosen just below the SRT. The magnetic field was applied along the x axis. Using the procedure mentioned at the beginning, the longitudinal (M_x) and polar (M_z) signal can be extracted [see Figs. 2(c) and (d)]. M_x shows a hard axis loop with almost no remanence and M_z reveals a hysteresis that is apparently not saturated.

Hysteresis loops taken with the MOKE setup in the yz plane in the same field are plotted in Figs. 3(a) and (b). The deconvoluted longitudinal signal (M_y) and polar signal (M_z) are shown in Figs. 3(c) and (d). It is important to note that the polar signals in both MOKE setups are the same although the angles of incidence are different [see Figs. 2(d) and 3(d)]. It means that the sensitivity of the polar Kerr effect is almost constant within that range of angles. This also gives a check of the accuracy of our experimental method. The signal in the y direction is very small (below 4 μrad). At the thickness under investigation the magnetic easy axis is perpendicular to the film plane. When the external field is applied along the x direction the magnetization is slightly tilted into the field direction. No torque is acting on the magnetization along the y direction and no signal appears.

The polar loop shown in Fig. 4(d) was obtained by applying the field in the vertical direction. It exhibits a squarelike

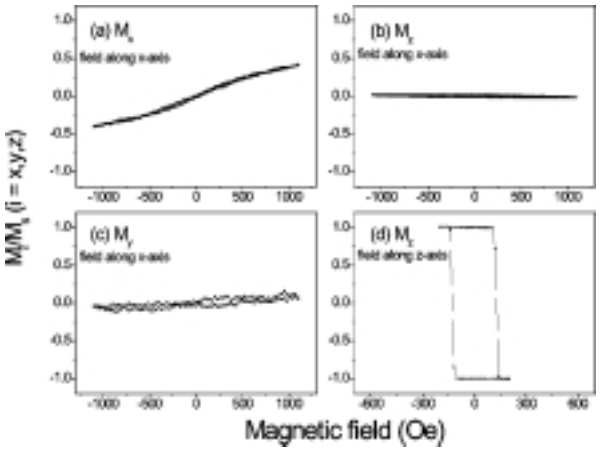

FIG. 4. (a)–(c) are the normalized magnetization components calculated with the data of Figs. 2 and 3. We have used a scaling factor of 8.4 ± 0.5 for the polar-versus-longitudinal Kerr sensitivity at an angle of incidence of 45°, and a factor of 4 ± 0.4 for the longitudinal Kerr sensitivity at the two angles of $\pm45°$ and $\pm9°$. (d) is the hysteresis loop obtained in a vertical field with the same film. The angle of incidence is 15°.

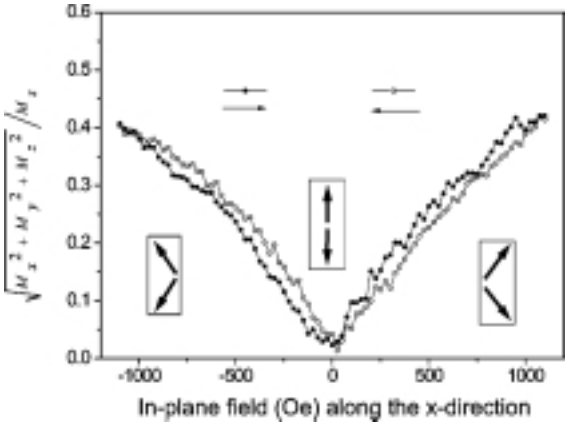

FIG. 5. The value of the magnetization calculated from the individual components in Fig. 4. The thinner arrows in the figures indicate the field scanning direction. The insets give a sketch of the proposed magnetic domain configuration.

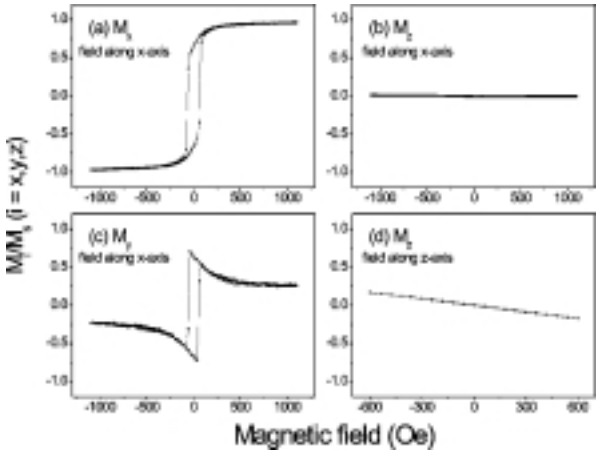

FIG. 6. (a)–(c) are the normalized magnetization components along the different directions deconvoluted from the data obtained at a thickness beyond the spin-reorientation transition (6.1 ± 0.3 ML). The scaling factors are the same as in Fig. 4. Fig. 6(d) is the hysteresis loop obtained with the same film in a vertical field.

easy axis loop with a small coercivity (about 125 Oe), which shows the easy axis to be perpendicular to the film plane. The signal in saturation is 50 times larger than the polar signal obtained in the in-plane field [Fig. 2(d)].

We have investigated the thickness dependence of the longitudinal signal in saturation for in-plane magnetization. From these data we can extrapolate to the film thickness under investigation. A Kerr ellipticity of 140 ± 5 μrad should be expected for the longitudinal signal in saturation. This value is in close agreement with the calculated value of 139 μrad in the 45° geometry.[15] Taking 140 ± 5 μrad and the polar saturation value 1180 ± 25 μrad we can calculate the relative sensitivities of the longitudinal to the polar signal. The polar signal is a factor of 8.4 ± 0.5 stronger than the longitudinal signal for 5 ML Co/Au and for an angle of incidence of 45°. Combining the theoretical and experimental values for the longitudinal Kerr-effect sensitivities we can estimate the relative sensitivities of the Kerr signals along the different components, i.e., 4:1:34 for $M_x : M_y : M_z$.

In Figs. 4(a)–(c), we have scaled the magnetization curves appropriately. Around 42% of the magnetization is found along the *x* direction in high fields. The signal in the *y* direction slightly increases with the field, which can be caused by a small misorientation of the field that causes the magnetization to tilt slightly towards the *y* direction. A small misalignment of the plane of incidence may also contribute to this signal, as a projection of the *x* component can appear. We have plotted (Fig. 5) the square root of the vectorial sum of the individual components (normalized to 100%) as a function of the field along the *x* direction. In this plot the curves show almost no remanence. The 42% of the M_x signal in high field can be interpreted as the magnetization to be tilted by about 25° away from the normal direction. Conversely that means that 9% of the magnetization signal along the *z* direction should be observed in case of a coherent rotation. In our measurement, however, only a 2% signal is found in the *z* component. Hence, we have to assume that the film is split into domains oppositely magnetized along the vertical direction. Applying a field along the *x* direction causes a tilt of the magnetization, i.e., the magnetizations in both spin-up and spin-down domains tilt towards the *x* direction. So a signal appears in the *x* direction while in the *z* direction the signal is almost balanced by domains with opposite vertical components (*z* components). The 2% signal appearing along the *z* direction can be caused by the misalignment of the magnetic field, which causes slightly unbalanced domain configurations or a small difference in the tilting for spin-up and spin-down domains. The magnetization process can be explained as follows: The film is in a multidomain state with a perpendicular direction of magnetization at zero field. The in-plane field forces the magnetization to tilt into the x axis. In the highest field the magnetization is tilted by 25° with respect to the surface normal.

For a thickness beyond the SRT the hard axis is perpendicular to the film plane [see Fig. 6(d) for a 6.1 ± 0.3-ML film]. When the external field is applied within the film plane, the magnetization reversal should proceed within the film plane [Figs. 6(a)–(c)]. In Fig. 6 the individual components of magnetization in an in-plane field are shown and have been scaled with the sensitivities given above and normalized to 100%. We clearly see that the magnetization along the *x* direction has almost reached saturation, i.e., 98% of the full signal is obtained in high fields. In the *z* direction the signal is less than 1%. The remaining signal is due to the misalignment of the magnetic field. Assuming that the Kerr signal that appears along the *z* direction in the in-plane field is caused by the misalignment of the field, we can estimate the angle of misalignment to be roughly 1°, since only 1% of the magnetization signal in high field is found in the *z* direction. Fig. 7 exhibits the field dependence of the magnetization obtained from the loops in Fig. 6. The value is nearly constant except for two dips around ± 60 Oe. First we would like to discuss the reliability of the observed structures. We have taken two possible mechanisms into consideration that could artificially cause sharp structures, i.e., a shift of data points and the uncertainty of the calibration

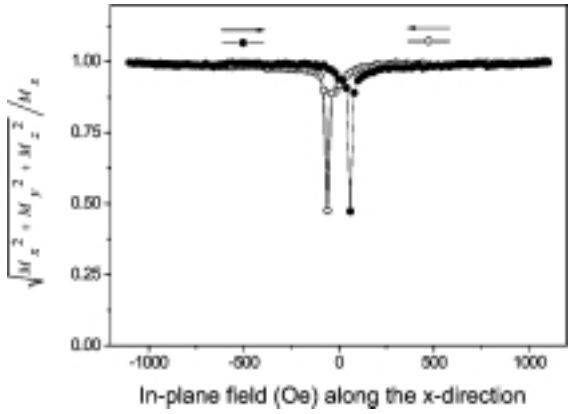

FIG. 7. The normalized value of the magnetization calculated from the individual components in Fig. 6.

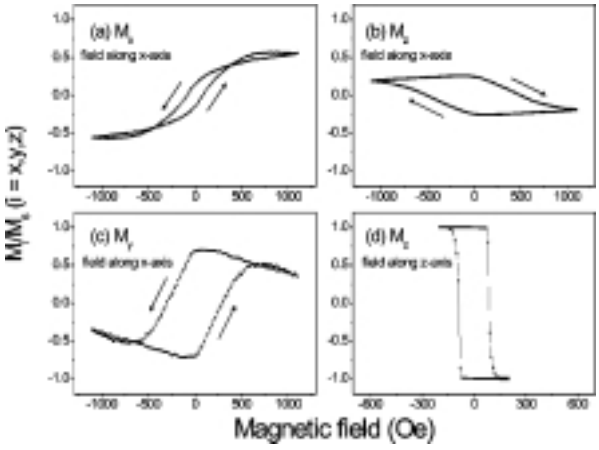

FIG. 8. (a)–(c) are the normalized magnetization components versus the in-plane field. The same scaling factors as in Fig. 4 are used for the normalization. The film thickness (5.3 ± 0.3 ML) was chosen to be within the spin-reorientation transition. The arrows indicate the switching directions. (d) is the hysteresis loop obtained in a vertical field.

factors. Any shift of the data points in the individual components can be ruled out as the Kerr signals in both MOKE setups are obtained at the same time in the same field and the calculation is made point by point. Furthermore, we performed a cross-check by shifting the data points one point upward or downward. The result is the same, i.e., the two dips still remain in the plot. To exclude also an effect due to the uncertainty of the calibration factors, we made a worst-case estimation. With 10% error margin we obtain in the plot a 20% effect, which cannot explain the strong decrease of around 60%. Hence, we have to assign the finding to the magnetic behavior of the sample. The strong decrease is most likely due to the creation of domains and the movement of domain walls. In case of coherent rotation of a single domain state the signal should stay constant everywhere. The single domain configuration splits up into a multidomain state in a field range where the reversal takes place. As the switching of the magnetization via domain nucleation and domain-wall movement can happen within a small field range our data are not dense enough to resolve the whole process in more detail. Consequently, we find only the trace of such a process, i.e., a loss of magnetization signal.

There are three generic cases of SRT for a uniaxial anisotropy system in second-order anisotropy approximation according to the sign of the second-order anisotropy constant K_2 within the transition.[32] The transition from the out-of-plane magnetization to the in-plane magnetization may happen via continuous canting of magnetization when $K_2>0$, or it directly changes from the vertical to the in-plane direction when $K_2=0$. The third situation appears when $K_2<0$, where the transition proceeds via a state of coexisting phases.

For the Co-on-Au(111) system two opposing results are reported. Allenspach *et al.*[17] claimed to find a canting of magnetization in the SRT while Oepen *et al.*[33,34] found evidence for a SRT via a state of coexisting phases. The essential difference between these two states is that the free energy in zero field has only one minimum at a certain canting angle in the first case while in the latter case two local minima for the vertical and the in-plane directions exist. Hence, only in case of coexisting phases the magnetization in zero field can be stabilized in one of these two special directions, i.e., the vertical or the in-plane direction.

To further identify the spin-reorientation transition of Co film on Au(111), we have also taken hysteresis loops at a thickness just within the spin-reorientation transition, i.e. at 5.3 ± 0.3 ML. In Figs. 8(a)–(c) the normalized individual components of magnetization in an in-plane field are shown using the sensitivities determined above. In all three components we find remanence and nonvanishing signals even at 1100 Oe. For M_x the remanence is lower than the signal in high field while the other two components reveal an opposite behavior. The remanence is found in both vertical and in-plane directions, which indicates that the thickness is indeed within the spin-reorientation transition. Taking an in-plane anisotropy into account, it is not surprising to find the maximum remanence in the *y* direction, which is around 80% of the full magnetization. Obviously, the in-plane easy axis is closer to the *y* direction.

The absolute value of the magnetization vector versus the applied field is shown in Fig. 9. We find minima around ±250 Oe that indicate that the dominant switching behavior is via domain-wall movement. It is somewhat strange that the magnetization signal decreases with increasing field above 500 Oe since an external field should drive the magnetization into a single domain state. To exclude the experimental error, we took the above-mentioned error margins of the scaling factors and recalculated the absolute magnetization value. We find that the magnetization signal still decreases with increasing field above 500 Oe within our experimental uncertainties. Hence, we have to consider it as a true magnetic behavior. The effect could be understood as follows. Although the magnetization has been switched by the external field, the field strength is still not large enough to erase all domains, which becomes evident from the fact that $\sqrt{(M/M_S)^2}<1$. The remaining domains are not strictly parallel/antiparallel to the field direction as magnetization signals are found in the other two directions as well. Besides

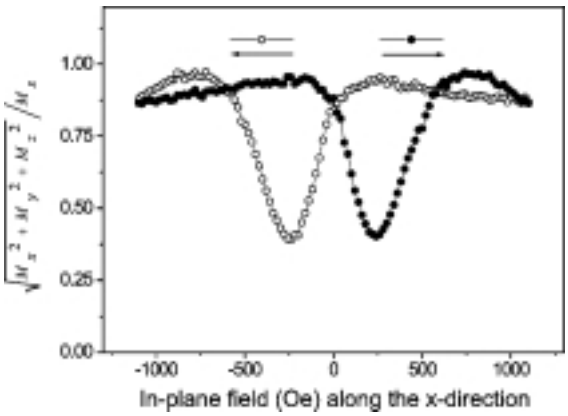

FIG. 9. The value of the magnetization calculated from the individual components in Fig. 8.

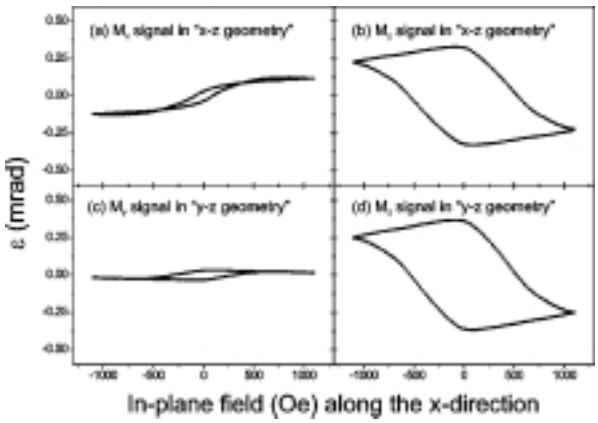

FIG. 10. The original data used for calculating the data shown in Figs. 8 and 9.

this canting of the magnetization of such domains, nucleation of domains and propagation of domain walls has to be expected. The decrease of magnetization value (in Fig. 9) could be due to the changes in the population of the different domains. The value obtained at $|H| \geqslant 1000$ Oe is nearly constant when reducing the field. This indicates that magnetization rotation is the dominant process until the flipping starts. Increasing the field in the opposite direction results in a flipping mainly in the *y* direction continued by an irreversible change in domain population. In order to demonstrate that no uncertainties of the experiments are responsible for the effects seen in Fig. 9 we plotted the original data in Fig. 10. In Figs. 10(a) and (b) are Kerr ellipticities along the *x* and *z* directions obtained in the ''*x*-*z* geometry.'' The Kerr ellipticities along the *y* and *z* direction obtained in the ''*y*-*z* geometry'' are plotted in Figs. 10(c) and (d). We find that the Kerr ellipticities along the *z* direction obtained by two measurements in different geometries are the same, within an error margin of less than 10%.

For a state of magnetization in canting or coexisting phases one would expect remanence in the vertical as well as the in-plane direction. Applying a field in different directions should help to distinguish between these two scenarios of spin-reorientation transition. In a case of canting magnetization the vertical component of magnetization should show a value in remanence that is independent of the field direction as there is only one free-energy minimum. On the other hand, for coexisting phases the value obtained in remanence depends on the direction along which the field has been applied.

In a vertical field we obtained a polar loop with full remanence, i.e., $M_r/M_s = 1$ [see Fig. 8(d)]. The saturation value of the signal 1340 ± 25 μrad is in complete agreement with the value obtained from the thickness dependence of the polar signal in saturation.[35] Apparently, the magnetization stays in perpendicular direction with a single domain state at zero field after saturating the film in a vertical field. This is strong proof for the transition to proceed via a state of coexisting phases instead of a canting state, since full remanence in the vertical direction can only be found in case of a state of coexisting phases within the spin-reorientation transition. Evidence for coexisting phases within the spin-reorientation transition was recently found for Fe/Cu(001) as well.[36]

V. CONCLUSIONS

In summary, we have developed a method to obtain the individual components of magnetization by means of a three-dimensional-MOKE technique. We applied this method to study the spin-reorientation transition of Co films on Au(111). Below the spin-reorientation transition, we observed a square loop in a vertical field, while in an in-plane field the magnetization has components not only along the field direction but also in perpendicular direction, which is attributed to a small misalignment of the field. Beyond the spin-reorientation transition, i.e., with an in-plane easy axis, we observe a hard axis loop in vertical field. The film is almost saturated in the film plane with a maximum in-plane field of 1100 Oe. The hysteresis indicates that there is domain nucleation during the reversal process. Within the transition region, the magnetization has remanence and nonvanishing components in all three directions in an in-plane field. After saturating the film in a vertical field, the magnetization remains in perpendicular direction with full remanence. From that behavior we conclude that the spin-reorientation transition of Co on Au(111) proceeds via a state of coexisting phases and not via continuous magnetization canting.

*Present address: Institut für Angewandte Physik, Universität Hamburg, Jungiusstrasse 11, 20335, Hamburg, Germany.
†Email address: oepen@physnet.uni-hamburg.de

[1] U. Admon, M.P. Dariel, E. Grunbaum, and J.C. Lodder, J. Appl. Phys. **66**, 316 (1989).
[2] E.M. Bradley and M. Prutton, J. Electron. Control **6**, 81 (1959).
[3] C.D. Olson and A.V. Pohm, J. Appl. Phys. **29**, 274 (1958).
[4] S.D. Bader, J. Magn. Magn. Mater. **100**, 440 (1991), and references therein.
[5] S.D. Bader and J.L. Erskine, in *Ultrathin Magnetic Structures*, edited by J.A.C. Bland and B. Heinrich (Springer-Verlag, Berlin, 1994), Vol. II, Chap. 4, and references therein.

[6] A. Hubert and R. Schäfer, *Magnetic Domains* (Springer-Verlag, Berlin, 1998), Chap. 2 and 3, and references therein.
[7] J.M. Florczak and E. Dan Dahlberg, J. Appl. Phys. **67**, 7520 (1990); Phys. Rev. B **44**, 9338 (1991).
[8] C. Daboo, J.A.C. Bland, R.J. Hicken, A.J.R. Ivews, and M.J. Baird, Phys. Rev. B **47**, 11 852 (1993).
[9] W. Rave, R. Schäfer, and A. Hubert, J. Magn. Magn. Mater. **65**, 7 (1987).
[10] P. Büscher and L. Reimer, Scanning **15**, 123 (1993).
[11] S.M. Jordan and J.S.S. Whiting, Rev. Sci. Instrum. **6**, 4286 (1996); J. Magn. Magn. Mater. **172**, 69 (1997).
[12] Z.J. Yang and M.R. Scheinfein, J. Appl. Phys. **74**, 6810 (1993).
[13] Z.Q. Qiu, J. Pearson, and S.D. Bader, Phys. Rev. Lett. **70**, 1006 (1993).
[14] A. Berger and M.R. Pufall, J. Appl. Phys. **85**, 4583 (1999).
[15] H.F. Ding, S. Pütter, H.P. Oepen, and J. Kirschner, J. Magn. Magn. Mater. **212**, L5 (2000).
[16] C. Chappert, D. Renard, P. Beauvillain, J.P. Renard, and J. Seiden, J. Magn. Magn. Mater. **54-57**, 795 (1986).
[17] R. Allenspach, M. Stampanoni, and A. Bischof, Phys. Rev. Lett. **65**, 3344 (1990).
[18] R.P. Hunt, J. Appl. Phys. **38**, 1652 (1967).
[19] M.J. Freiser, IEEE Trans. Magn. **4**, 152 (1968).
[20] J. Zak, E.R. Moog, C. Liu, and S.D. Bader, J. Magn. Magn. Mater. **89**, 107 (1990); J. Appl. Phys. **68**, 4203 (1990); Phys. Rev. B **43**, 6423 (1991).
[21] C.-Y. You and S.-C. Shin, Appl. Phys. Lett. **69**, 1315 (1996).
[22] In this paper, we define the angle of incidence as positive when the incident beam is closer to the positive component of magnetization effective in the longitudinal Kerr effect.
[23] D.M. Zehner and J.F. Wendelken, in *Proceedings of the Seventh International Vacuum Congr. and Third International Conference on Solid Surfaces, Vienna, 1977*, edited by R. Dobrozemsky *et al.* (Berger, Vienna, 1977), p. 517.
[24] W.J. Kaiser and R.C. Jaklevic, Surf. Sci. Lett. **182**, L227 (1987).
[25] M. Speckmann, H.P. Oepen, and H. Ibach, Phys. Rev. Lett. **75**, 2035 (1995).
[26] A misalignment of a few degrees has to be expected.
[27] E.R. Moog, C. Liu, S.D. Bader, and J. Zak, Phys. Rev. B **39**, 6949 (1989).
[28] Z.Q. Qiu, J. Pearson, and S.D. Bader, Phys. Rev. B **46**, 8195 (1992).
[29] R.M. Osgood III, K.T. Riggs, A.E. Johnson, J.E. Mattson, C.H. Sowers, and S.D. Bader, Phys. Rev. B **56**, 2627 (1997).
[30] *CRC Handbook of Chemistry and Physics*, 74th ed. (CRC Press, Boca Raton, FL, 1993).
[31] Generally speaking, it is not necessary to calculate the longitudinal Kerr-effect sensitivities if the angles of incidence in both geometries are the same.
[32] Y.T. Millev and J. Kirschner, Phys. Rev. B **54**, 4137 (1996).
[33] H.P. Oepen, M. Speckmann, Y.T. Millev, and J. Kirschner, Phys. Rev. B **55**, 2752 (1997).
[34] H.P. Oepen, Y.T. Millev, and J. Kirschner, J. Appl. Phys. **81**, 5044 (1997).
[35] S. Pütter, Ph.D. thesis, Martin-Luther University, 2000.
[36] E. Mentz, A. Bauer, T. Günther, and G. Kaindl, Phys. Rev. B **60**, 7379 (1999).

Appendix B

Curriculum vitae

Personal data:

Name:	Haifeng Ding
Date of birth:	July 05, 1973
Place of birth:	Fujian, P.R. China
Marital status:	Single

Education:

Sept. 1979 – Feb. 1984,	The Xingdi primary school of Lianchen city, Fujian Province, China.
Feb. 1984 – July 1985,	The Shiyan primary school of Lianchen city, Fujian Province, China.
Sept. 1985 – July 1987,	The first middle school of Lianchen city, Fujian Province, China.
Sept. 1987 – July 1991,	The first middle school of Longyan city, Fujian Province, China.
Sept. 1991 – July 1995,	B.Sc. at Tianjin University, Tianjin, China Major: Applied Physics.
Sept. 1995 – July 1998,	M.Sc. at Fudan University, Shanghai, China Supervisor: Prof. Xiaofeng Jin Thesis: Magnetic properties of ultrathin films in wedge shapes.

July 1998 – June 2001, Ph.D. candidate at Max-Planck-Institut für Mikrostrukturphysik, Halle, Germany
Supervisor: Prof. Dr. Jürgen Kirschner
Thesis: Spin-polarized scanning tunneling microscopy.

Honor:

Excellent student of Tianjin University, 1993

Excellent student of Tianjin City, 1994

Halle, 18. June 2001. Haifeng Ding

Appendix C

Publication lists

Publication list during Ph.D.

1. Tunneling magneto resistance in the limit of small gap distances
   H.F. Ding, W. Wulfhekel and J. Kirschner
   To be submitted.

2. How sharp can magnetic domain wall be?
   H.F. Ding, W. Wulfhekel and J. Kirschner
   Submitted to Europhys. Lett. (May 2001).

3. Amorphous, low magnetostriction tips for spin-polarized scanning tunneling microscopy
   W. Wulfhekel, R. Hertel, H.F. Ding, G. Steierl and J. Kirschner
   Submitted to J. Magn. Magn. Matter. (April 2001).

4. Magnetic susceptibility: An easy approach to the spin-reorientation transition
   S. Pütter, H.F. Ding, Y.T. Millev, H.P. Oepen and J. Kirschner
   Submitted to Phy. Rev. B (Feb. 2001).

5. A combined magnetic force and spin-polarized scanning tunneling microscopy study of the closure domain pattern of Co(0001)
   H.F. Ding, W. Wulfhekel, C. Chen, J. Barthel, and J. Kirschner
   Materials Science and Engineering B **84**, (2001) 96.

6. High resolution magnetic imaging by local tunneling magneto-resistance
   W. Wulfhekel, H.F. Ding, W. Lutzke, G. Steierl, M. Vázquez, P. Marín, A. Hernando, and J. Kirschner
   Appl. Phys. A **72**, (2001) 463.

7. Spin-reorientation transition in thin films studied by the component-resolved Kerr effect
   H.F. Ding, S. Pütter, H.P. Oepen, and J. Kirschner
   Phys. Rev. B **63**, (2001) 134425.

8. High-resolution study of magnetization and susceptibility by spin-polarized tunneling microscopy
   W. Wulfhekel, H.F. Ding and J. Kirschner
   J. Appl. Phys. **87**, (2000) 6475.

9. Field-driven reorientation in ultrathin ferromagnetic films with uniaxial anisotropy
   H.P. Oepen, Y.T. Millev, H.F. Ding, S. Pütter and J. Kirschner
   Phys. Rev. B **61**, (2000) 9506.

10. Experimental method for separating longitudinal and polar Kerr signals
    H.F. Ding, S. Pütter, H.P. Oepen and J. Kirschner
    J. Magn. Magn. Mater. **212**, (2000) L5.

Publication list during M.Sc.

1. Epitaxy and magnetism of Co on GaAs(001)
   Y.Z. Wu, H.F. Ding, C. Jing, D. Wu, G.S. Dong, X.F. Jin, K. Sun and S. Zhu.
   J. Magn. Magn. Mater. **198-199**, (1999) 297.

2. In-plane magnetic anisotropy of bcc Co on GaAs(001)
   Y.Z. Wu, H.F. Ding, C. Jing, D. Wu, G.L. Liu, V. Gordon, G.S. Dong, X.F. Jin, K. Sun and S. Zhu.
   Phys. Rev. B **57**, (1998) 11935.

Appendix D

Erklärung

Ich versichere hiermit, die vorliegende Dissertation

Spin-polarized scanning tunneling microscopy

selbständig verfaßt und keine anderen als die von mir angegebenen Quellen und Hilfsmittel verwendet zu haben. Die den benutzten Werken wörtlich oder inhaltlich entnommennen Stellen sind als solche kenntlich gemacht.

Halle, 18. June 2001 Haifeng Ding

Appendix E

Acknowledgements

First of all I would like to express my great thanks to my supervisor Prof. Dr. Jürgen Kirschner for giving me the opportunity to work at Max-Planck-Institute in his department. I would like to thank for his constant deposition for discussions, for his keen interest in my work. His expert's knowledge, ideas and suggestions were very helpful for me. I benefited a lot from them. I wish to thank for his trust, support, guidance and encouragement. I also appreciate very much that he supported me to participate several international conferences which widened my view of research.

I am very grateful to Dr. Wulf Wulfhekel for teaching me the experimental technique of Spin-polarized STM. I thank him for the time he spent with me in the laboratories when explaining me all experimental details and tricks. I really appreciate many long discussions which were important and motivating for me. I should thank him for his patience as well.

I also very much appreciate the help of Prof. Dr. Hans-Peter Oepen. He not only guided me in the field of magneto-optics in the beginning of my Ph.D. studies but also opened me a fantastic world of research.

I should mention the help from my Master thesis supervisor, Prof. Xiaofeng Jin. It is him who recommended me to apply to study in Halle. I wish to thank him for his long time encouragement.

I would like to thank Prof. M. Vázquez for his kind supply of the special magnetic wires for making the tips used for the Sp-STM measurements. I very much appreciate Dr. Gerold Steierl for the SEM imaging of the tip and Dr. Jochen Barthel for help with the MFM measurements.

I wish to thank my colleagues and coworkers Dr. Jochen Barthel, Dr. Chen Chen, Dr. Riccardo Hertel, Dr. Dimitre Iorgov, Dr. Manfred Klaua, Mr. Guolei Liu, Dr. Wim Lutzke, Mr. Fabrizio Porrati, Dr. Sabine Pütter, Dr. Gerold Steierl, Mr. Florin Zavaliche for their helping hands, instructive discussions and friendly atmosphere. It was my great pleasure to work with all of them. Particularly, I would like to thank Dr. Sabine Pütter for teaching me the susceptibility technique.

Discussions with Prof. Dr. Ulrich Gradmann, Prof. Dr. Patrick Bruno, Dr. Jürgen Henk, Dr. Wolfgang Kuch, Dr. Miroslav Nývlt, Dr. Dirk Sander, Dr. Rüdiger Vollmer were very helpful for me. I wish to thank them for sharing with me their busy time.

An experimental Ph.D. is impossible without technical support. I thank especially to Mr. Herbert Engelhard, Mr. Detlef Hartung for the Sp-STM chamber construction and for frequent help with trouble-shooting. I also wish to thank Mrs. Heike Menge, she prepared many times the etching solution for STM tips, and Mr. Günter Kroder, he helped me in the Au evaporator preparation. My thanks are also addressed to the colleagues in the electronic and mechanical workshop.

I thank also all the other colleagues at Max-Planck-Insitut für Mikrostrukturphysik. They offered me a very nice environment which allowed me to work with high efficiency and great pleasure. I only know a few words of German. "Danke" is the most important one I have learned. I should say **Danke** to all the colleagues at this institute. I did enjoy the time I spent here.

Studying in a foreign country with the language you don't know from the beginning is not easy. It would be troublesome without the helps from friends. Particularly, I would like to thank Mr. Roger Pflanz, who helped me to settle down my first apartment in Germany, Mr. Fabrizio Porrati, who helped me in getting my bicycle on the second day after my arrival. I wish to thank all the friends in Halle, German friends, Chinese friends and all my friends from the other countries. I wish to thank Mrs. Xiaohong Chen, Dr. Qinyuan Jin, Dr. An-ping Li, Dr. Xucun Ma, Dr. Ge Men, Dr. Xianghong Qian, Dr. Dong Shen, Dr. Jian Shen, Mr. Yixin Zhang for the help in life and the pleasant time spent together.

I owe a lot to Dr. Yizheng Wu and Mr. Jian Yao for their friendship like brothers. I will never forget their care and encouragement. The long time discussions about life and future are, of course, very important for my Ph.D. work and future.

Special thanks to my parents and to Miss Siying Zhang for their love, support and encouragement through the years of my studies. I cannot imagine what my life would be without their love. If there is any success of mine, it belongs to them.